Technische Universität München
TUM School of Natural Sciences

TUM

Photoredox Catalysis with Metal-Mabiq Complexes

Oaikhena Zekeri Esezobor

Vollständiger Abdruck der von der TUM School of Natural Sciences der Technischen Universität München zur Erlangung des akademischen Grades eines

Doktors der Naturwissenschaften

genehmigten Dissertation.

Vorsitz: Prof. Dr. Klaus Köhler
Prüfer*innen der Dissertation: 1. Prof. Dr. Corinna. R. Hess
2. Prof. Dr. Lukas Hintermann

Die Dissertation wurde am 23.11.2023 bei der Technischen Universität München eingereicht und durch die TUM School of Natural Sciences am 08.12.2023 angenommen.

"Darkness cannot drive out darkness; only LIGHT can do that".

– Martin Luther King, Jr.

This dissertation describes the work carried out by Oaikhena Zekeri Esezobor at the Faculty of Chemistry, Technical University of Munich from November 1, 2019, to April 30, 2023, under the supervision of Prof. Corinna R. Hess.

Dedicated to:

Oshuwa Esezobor 💔 🕊️

23 January 1992 – 28 December 2021.

Continue to Rest in Peace.

Acknowledgements

List of Abbreviations

Å	Ångström
BCB	bicyclobutane
Boc	tert-butyloxycarbonyl
Bpy	bipyridine
CT	charge transfer
DBAD	Di-tert-butyl azodicarboxylate
DIPEA	diisopropyl ethylamine
Dtbbpy	4,4'-Di-tert-butyl-2,2'-dipyridyl
EA	energy acceptor
ee	enantiomeric excess
EnT	energy transfer
Equiv.	equivalents
ESI	electrospray ionization
ET	electron transfer
E_T	triplet energy
Et_3N	triethylamine
fs	femtosecond
GC	gas chromatography
HAT	hydrogen atom transfer
ISC	intersystem crossing
K	Kelvin
kcal	kilocalorie
kJ	kiloJoules
LMCT	ligand-to-metal charge transfer
max	maximum
MC	metal-centered
MeCN	acetonitrile
MHAT	metal-hydride hydrogen atom transfer
MLCT	metal-to-ligand charge transfer

MO	molecular orbital
mol	mole
MS	mass spectrometry
NMR	nuclear magnetic resonance
ns	nanosecond
^{o}C	degree Celsius
PC	photocatalyst
Ppy	phenylpyridine
S_0	singlet state
S_1	singlet excited state
SCE	standard calomel electrode
SET	single electron transfer
T_1	triplet excited state
THF	tetrahydrofuran
TM	transition metal
UV Vis	ultraviolet/visible region
V	Volts
VLIH	visible light-induced homolysis
XRD	X-ray diffraction
λ	wavelength
μs	microseconds

Publication List

- **Oaikhena Zekeri Esezobor,** Wenyi Zeng, Lukas Niederegger, Michael Grübel, and Corinna R. Hess. Co–Mabiq Flies Solo: Light-Driven Markovnikov-Selective C- and N-Alkylation of Indoles and Indazoles without a Cocatalyst. *J. Am. Chem. Soc.* **2022**, *144*, 2994–3004.

- Raphael Lauenstein, Sophie L. Mader, Henrieta Derondeau, **Oaikhena Z. Esezobor,** Matthias Block, Armin J. Römer, Christian Jandl, Eberhard Riedle, Ville R. I. Kaila, Jürgen Hauer, Erling Thyrhaug and Corinna R. Hess. The central role of the metal ion for photoactivity: Zn– vs. Ni–Mabiq. *Chem. Sci.,* **2021**, *12*, 7521 – 7532.

Conference Contributions

- Oaikhena Zekeri Esezobor and Corinna R. Hess. 17. Koordinationschemie-Treffen (KCT), Jena 2022, Germany. "Visible Light Induced and Co-Mabiq Catalyzed C3- and N-Alkylation of Indoles and Indazoles" (Oral Presentation).

- Oaikhena Zekeri Esezobor, Wenyi Zeng, Lukas Niederegger, Michael Grübel and Corinna R. Hess. Gordon Research Conferences – 2022 Electron Donor-Acceptor Seminar/Interactions, Salve Regina University in Rhode Island, United States. "Light-Driven Reactions with Co-Mabiq" (Poster Presentation).

- Oaikhena Zekeri Esezobor, Raphael Lauenstein, Michael Grübel and Corinna R. Hess. Exploratory Photochemistry: Light Creates Structure. Nationale Akademie der Wissenschaften Leopoldina, Jägerberg 1, 06108 Halle, Germany, 2021. "Photoredox Catalysis with Metal-Mabiq Complexes" (Poster Presentation).

- Oaikhena Zekeri Esezobor, Raphael Lauenstein, Michael Grübel and Corinna R. Hess. Anglo-German Inorganic Chemistry Conference (2021 AGICHEM) – Online. "Photoredox Catalysis with Metal-Mabiq Complexes" (Poster Presentation).

- Oaikhena Zekeri Esezobor, Michael Grübel, Irene Bosque, Thorsten Bach, Corinna R. Hess. 16. Koordinationschemie-Treffen (KCT), Freiburg 2020, Germany. "Redox and photocatalytic properties of cobalt and nickel complexes of macrocyclic biquinazoline (Mabiq) ligand" (Poster Presentation).

Table of Contents

Chapter 1

1.1 Introduction

The tremendous advances achieved in radical chemistry in the last 2 decades has been partly due to the resurgence of interests in photoredox catalyzed transformations in synthetic organic chemistry.[1] Although radicals were hitherto misconstrued as highly uncontrollable intermediates, advances in transition metal catalyzed cross coupling reactions and light-induced modes of substrate activation have demystified this misconception.[1c] Photoredox catalysis offers myriads of substrate activation and mechanistic pathways, and as a result provides access to challenging synthetic routes, complex structural motifs, and reduction in synthetic steps. The mild reaction conditions, functional group tolerance and compatibility with other catalytic methods (dual catalysis) have also underpinned the enormous interests in photoredox catalysis.[1b, 1e, 1i, 1k, 2]

Nature's inspiration with photosynthesis, the biological process that powers all life forms on earth, is the foundation for photoredox catalysis. The key components of photosynthesis are sunlight and the light-harvesting green pigment, chlorophyll **1** (Figure 1). Sunlight is a renewable resource on earth and Nature found a way to harness it by deploying the magnesium containing molecule, chlorophyll, for harvesting and transducing sunlight energy into chemical energy.[3] Chlorophyll is found in cyanobacteria and in the chloroplast of algae and plants.[4]
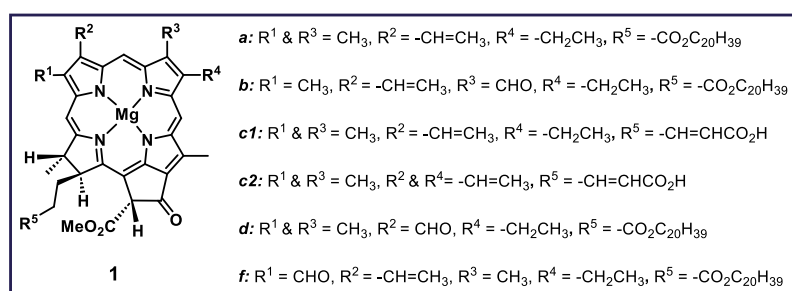
Figure 1. Chlorin backbone in chlorophyll and all types of chlorophyll found in Nature.[4a]

The first step in photosynthesis is the splitting of H_2O into molecular O_2, protons and electrons with sunlight energy (equations 1 – 3). This is followed by a dark phase (Calvin cycle) which involves the reduction of CO_2 to carbohydrates with electrons and protons generated in the light reaction (equation 2).[4b, 5]

Light reaction

$$2H_2O + light \rightarrow O_2 + 4H^+ + 4e^- \ (\Delta G^o = +317 \ kJ \cdot mol^{-1}) \qquad \text{equation 1}$$

Dark reaction

$$CO_2 + 4H^+ + 4e^- \rightarrow CH_2O + 4H_2O \ (\Delta G^o = +162 \ kJ \cdot mol^{-1}) \qquad \text{equation 2}$$

Overall reaction

$$H_2O + light + CO_2 \rightarrow CH_2O + O_2 \ (\Delta G^o = +479 \ kJ \cdot mol^{-1}) \qquad \text{equation 3}$$
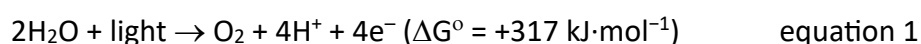
Equation 3 represents the beginning of many complex biological cycles which culminate in the synthesis of sugars, amino acids, lipids, etc, that are essential for the sustenance of plants and animals. Overall, photosynthesis plays the essential role of regulating the amounts of the greenhouse gas, CO_2, in the atmosphere, and in the production of oxygen, which is vital for sustenance of life on earth.[4b, 5]

1.2 Resurgence in Photocatalysis (Photoredox Catalysis)

Until late 2008 when the groups of D.W.C. MacMillan (2021 Nobel Prize winner),[6] T.P. Yoon[7] and C.R.J. Stepheson[8] independently reported photoinduced transformations employing the one-electron photoredox catalyst, $[Ru(bpy)_3]^{2+}$ **2**, photoredox catalyzed synthetic methodologies were sparingly reported in the literature.[1f] Before 2008, most light-induced reactions (referred to as photochemical reactions) involved the use of UV light.[9] The challenge in the use of UV light is the low abundance of UV wavelength required for photochemical reactions in the solar spectrum. As a result, to safely generate such UV radiation, specialized devices had to be designed.[10] Furthermore, even though the UV region is of high energy and can initiate bond-breaking and -making steps, extending light-initiated reactions to lower energy (i.e. visible region of the absorption spectrum) was desirable to expand the application of light in chemical synthesis.[11] However, the inability of many organic substrates to absorb visible light and engage in desired reactivity posed a challenge.[10] Hence, to drive chemical reactions with visible light, photoactive catalysts are generally required. Thus, photoactive transition metal complexes such as $[Ru(bpy)_3]^{2+}$ **2**, *fac*-(Ir(ppy)$_3$) **3**, and organic dyes, that can be excited upon absorption of visible light energy and engage in SET or EnT processes were developed.[1b, 1d, 1f, 1j-l, 2a, 10, 12]

With regards to $[Ru(bpy)_3]^{2+}$ **2** in particular, its photochemistry, photophysics and chemiluminescence and applications in water splitting, CO_2 activation and energy storage were already established as far back as 1959.[13] Despite this knowledge, its use in core synthetic organic chemistry was not explored. Nevertheless, since the "seminal" works by MacMillan,[6a] Yoon[7] and Stephenson,[8] the field of photoredox catalysis has experienced a resurgence and contributed tremendously to synthetic organic chemistry by utilizing photoactive complexes such $[Ru(bpy)_3]^{2+}$ **2**, *fac*-(Ir(ppy)$_3$) **3**, and organic dyes[1b-g, 1i, 1j, 1l, 6a, 12a] **(Figure 2)**, and more recently earth abundant transition metal complexes.[1h]
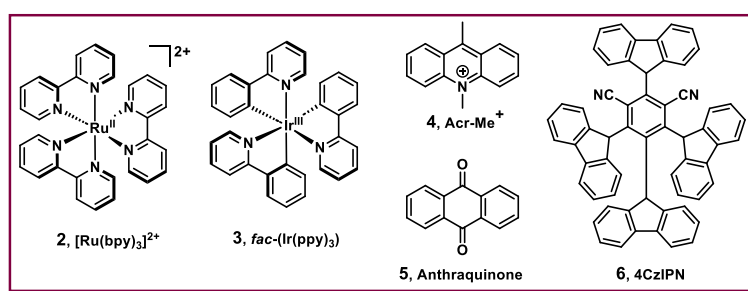
Figure 2. Examples of photoactive complexes and organic dyes.

An intriguing aspect of the seminal report by MacMillan and Nicewicz[6a] is that the transformation was enantioselective and merged organo- and photoredox catalysis, even though at that time, photoredox catalysis was still underdeveloped. They demonstrated the asymmetric alkylation of aldehydes with alkyl bromides via enamine and alkyl radical intermediates to furnish yields and *ee* as high as 93% and 99% respectively. Key aspects of the mechanism include the condensation of the imidazolidinone and aldehyde to form enamine. SET from the sacrificial electron donor (2,6-lutidine) or in situ generated enamine to excited state $*[Ru^{II}(bpy)_3]^{2+}$ generates $[Ru^{II}(bpy)_2(bpy^{\bullet-})]^+$. *(In many literature, the formal notation for $[Ru^{II}(bpy)_2(bpy^{\bullet-})]^+$ is $[Ru(bpy)_3]^+$ or Ru^I-species. For convenience, $[Ru(bpy)_3]^+$ is used in catalytic cycles while Ru^I-species is used in text describing catalytic cycles shown in this thesis). Ru^I-species* transfers an electron to the alkyl halide to generate the alkyl radical. Alkyl radical addition to the enamine and SET from the resultant α-amino radical intermediate to excited state $*[Ru(bpy)_3]^{2+}$ furnishes the iminium ion intermediate. Finally, hydrolysis of the iminium ion generates the enantioenriched product and regenerates the imidazolidinone catalyst (Scheme 1). The utility of the organophotoredox methodology was further demonstrated in the enantioselective α-trifluoromethylation and α-benzylation of aldehydes.[14]
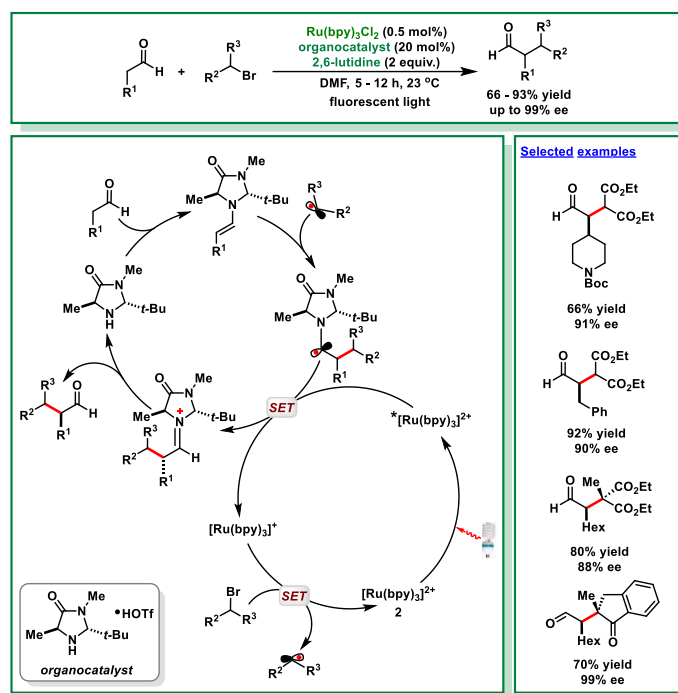
Scheme 1. Organo- and photoredox catalyzed asymmetric α-alkylation of aldehydes with alkyl bromides.[6a]

The report by Yoon and coworkers[7] underlined the possibility to merge photoredox catalysis with another mode of substrate activation, Lewis acid catalysis. The intramolecular diastereoselective [2+2] cycloaddition of bis(enone), which they reported, involved the Lewis acid activation of aryl enone and one electron reduction of the activated enone by Ru^I-species. A sacrificial electron donor (amine) was required to reduce the excited state Ru^{II}-photocatalyst (Scheme 2). They further developed an intermolecular [2+2] cycloaddition protocol in which enantioselectivity was achieved with the use of a chiral Lewis acid. The functionalised cyclobutanes reported in the work had enantiomeric excess of up to 97%.[15]
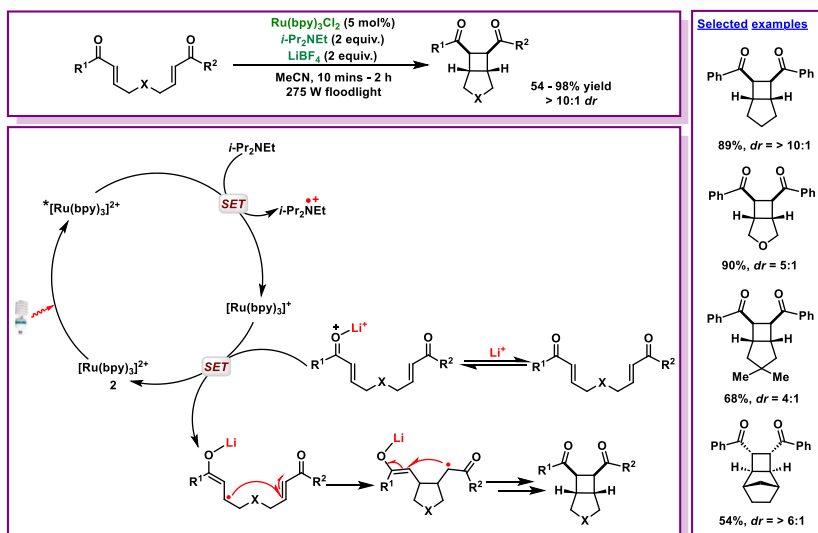
Scheme 2. Photoredox and Lewis acid catalyzed [2+2] cycloaddition.[7]

1.3 Mechanisms in Photocatalysis

1.3.1 Single Electron Transfer (SET)

The most common process encountered in photoinduced transformations is the single electron transfer (SET), which result from the interaction between an excited photocatalyst and a suitable organic substrate. The electron transfer to and from a substrate leads to the generation of radical anions or cations, or a neutral radical if the substrate contains a leaving group. Unlike the ground state of a photoactive compound, its electronically excited state is both a stronger reductant and oxidant. This photoinduced ET pathway is known as *photoredox catalysis* since both reductive and oxidative events occur and lead to intermediates which react to form new bonds (Scheme 3).[1b, 1f, 1g, 16]
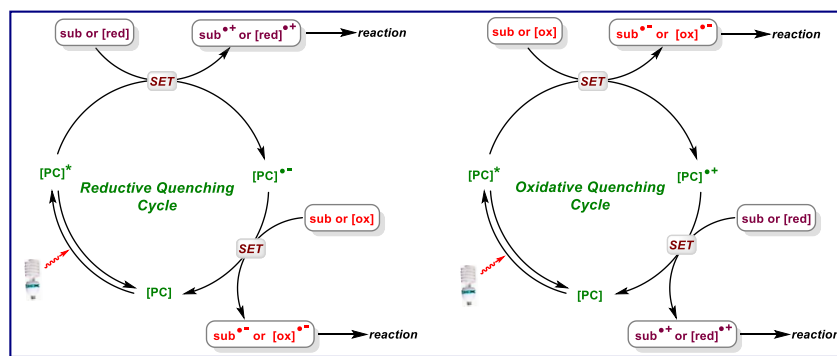
Scheme 3. Electron transfer pathway in photoredox catalysis.

Upon excitation, photoactive transition metal complexes undergo MLCT, LMCT, d→d, π→π*, etc, electronic transitions. The lifetimes and redox potentials of the excited state species which are formed during these transitions are crucial for the generation of reactive intermediates upon interaction with organic substrates. Hence, long-lived excited state lifetimes and high redox potentials are desirable for photoredox catalysts. For example, *fac*-(Ir(ppy)$_3$) **3** (τ = 1.9 µs), when excited can act as both an oxidant ($E_{1/2}^{*III/II}$ = +0.31 V vs SCE) and a reductant ($E_{1/2}^{*III/IV}$ = −1.73 V vs SCE. *Ir^{IV} is a formal notation; the actual species generated is [Ir^{III}(ppy)$_2$(ppy$^{\bullet+}$)]$^+$* (Scheme 4).[1b, 1f, 1g, 16]
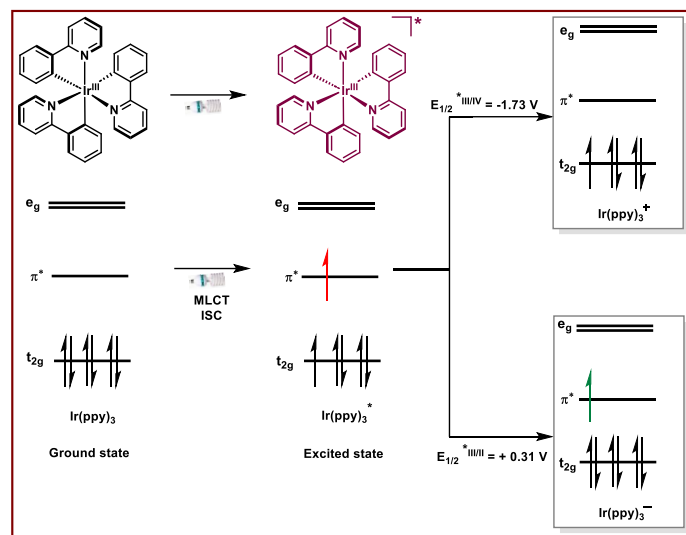
Scheme 4. Molecular orbital diagram of Ir(ppy)₃ showing ground and excited state transition.

A myriad of transformations initiated by SET from photoredox catalysts are reviewed in the literature.[17] The dominant catalysts employed in these transformations are polypyridyl complexes of Ru and Ir, and several organic dyes which have very long-lived excited state lifetimes and high redox potentials.[1i, 1j, 2c] The utility of photoredox catalyzed reactions involving SET have also been extended to three-component reactions in which two groups are introduced at vicinal positions of an alkene.[18] An example of this strategy is the recent report by Zhu and co-workers in which 1,3-dienes were difunctioalized by amide and azide groups. They employed *fac*-(Ir(ppy)₃) **3** as photoredox catalyst, N-amidopyridinium salt as amine source and TMSN₃ as azide source. The authors reported that with 1-aryl substituted 1,3-dienes, 1,2-amidoazidation were exclusively formed as products, while their 1-alkyl counterparts afforded moderate to high 1,2- vs 1,4-amidoazidation products. The mechanism proposed for the reaction involves the reduction of N-amidopyridinium salt via SET from excited state *fac*-(Ir(ppy)₃) **3** to generate an amidopyridinium radical. Radical fragmentation results in an NHBoc-radical which then adds onto the diene to furnish an alkyl radial intermediate. Oxidation of the alkyl radical by Ir^{IV}-species generates alkyl cationic species and concurrent regeneration of the ground state Ir^{III}. Finally, nucleophilic addition of the azide affords the desired product regioselectively (Scheme 5).[19]
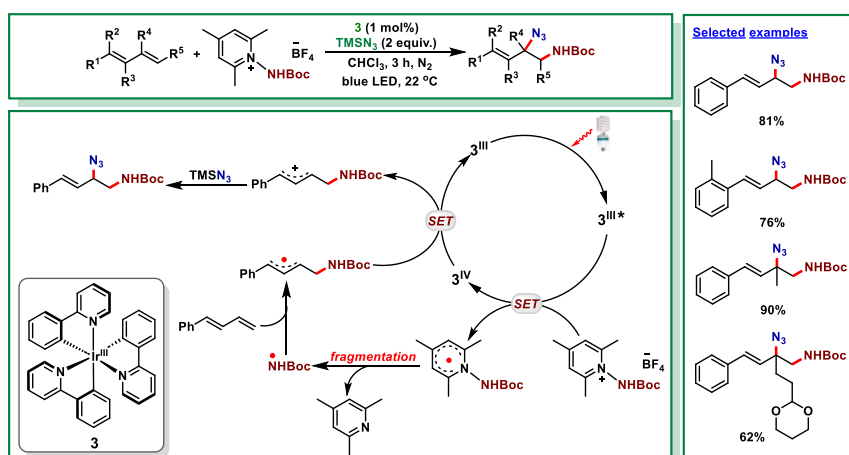
Scheme 5. Photoredox catalyzed three-component amidoazidation of 1,3-dienes.[19]

1.3.2   Energy Transfer (EnT)

Energy transfer from an excited photocatalyst (PC) to a suitable substrate is also an intriguing route for generating reactive intermediates and initiating photoinduced transformations. In EnT catalysis, the photocatalyst, referred to as a *photosensitizer*, upon excitation transfers its triplet energy to another molecule (energy acceptor, EA) rather than engage in SET. Unlike SET processes, EnT pathways do not rely on the redox potentials of the substrates. The crucial properties of the photosensitizer and EA relevant for efficient catalysis to occur via EnT is the triplet-state energies of the molecules.[12a, 12b] The triplet energy, E_T, of the photosensitizer should be greater than or equal to that of the EA. The key steps in EnT catalysis are the excitation of the PC from its ground singlet state (S_0) into the low-lying singlet excited state (S_1), followed by intersystem crossing (ISC) which generates the triplet excited state (T_1) of the PC.[2a] Upon collision of the PC in its T_1 state with an EA, intermolecular EnT occurs which promotes the EA from its S_0 to T_1 and returns the PC from T_1 to S_0 simultaneously (Scheme 3).[2a, 12a, 12b] At this point, the EA then engages in a reaction while the PC absorbs visible light, and the catalytic process continues (Scheme 6).
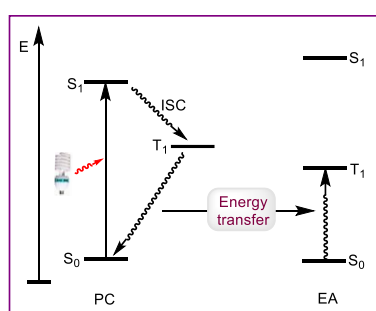
Scheme 6. Photoinduced EnT pathway.[2a, 12a]

Utilizing the mechanistic understanding of EnT catalysis, several challenging transformations have been demonstrated including enantioselective variants in which chiral photosensitizers or achiral photosensitizers combined with a chiral cocatalyst were employed.[2a, 12a, 12b] EnT catalysis is frequently employed in the construction of very complex bicyclic compounds such as bicyclobutanes (BCBs) via [2+2]–cycloaddition.[20] Photoinduced EnT reactions such as cycloadditions have been demonstrated to tolerate a wider range of functional groups and substrates when compared with SET-initiated alternatives. Furthermore, other photoinduced EnT reactions available in the literature include deracemization and dearomative cascade reactions.[2a, 12a, 12b, 21] Similar to photoinduced SET reactions, EnT-initiated transformations can also be merged with other types of substrate activation pathways. Such systems are referred to as *dual catalysis* and examples are shown in the dual catalysis section.

In 2022, Glorious and co-workers employed [Ir(dF(CF$_3$)ppy)$_2$(dtbbpy)]PF$_6$ **8** (E_T = 61.8 kcal/mol) as an EnT photocatalyst in the synthesis of polysubstituted 2-oxabicyclo[2.1.1]hexanes from benzoylformate esters and BCBs. The [2π + 2σ] photocycloaddition involved the sensitization of benzoylformate esters (E_T ~62 kcal/mol) via triplet EnT from **8** upon excitation with blue LEDs (λ_{max} = 450 nm). The EnT is followed by the reaction of the triplet excited state of the benzoylformate esters with BCBs, ISC and radical-radical coupling of the diradical intermediate. Intramolecular HAT, aryl group migration via an aryl-radical transition state, and finally a second intramolecular HAT step produces the desired polysubstituted

2-oxabicyclo[2.1.1]hexanes (Scheme 7).[22] Although the yields reported were not above 56%, the protocol provides a mild and atom-economical approach for the synthesis of 2-oxabicyclo[2.1.1]-hexanes (2-oxa-BCHs), which are potential phenyl bioisosteres.
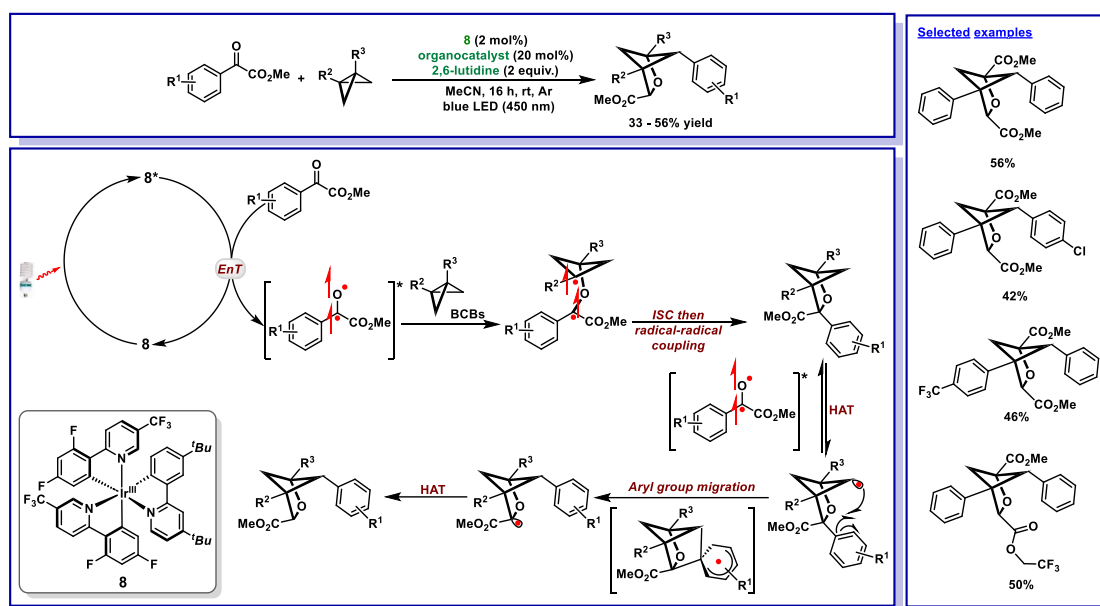
Scheme 7. Photoinduced EnT [2π + 2σ] photocycloaddition.[22]

Bach and co-workers have demonstrated the use of chiral xanthone and thioxanthone as efficient catalysts for enantioselective EnT intramolecular [2+2] photocycloaddition and deracemization reactions.[23] Recently in 2022, they reported the photoinduced chiral thioxanthone-catalyzed deracemization of alkenes via triplet EnT. Racemic mixtures of alkylidenecyclobutanes and alkylidenecyclopentanes were irradiated with blue LEDs (λ = 420 nm) in the presence of the chiral thioxanthone **9** (ET = 263 kJ mol^{-1}) to afford enantiopure products with yields and *ee* up to quantitative and 96% respectively. Sensitization of the substrate is proposed to occur intramolecularly after the formation of a catalyst-substrate complex. This is possible due to the presence of a cyclic amide substituent on the parent thioxanthone ligand backbone which can form hydrogen bonds with the substrate. The formation of a hydrogen bond thus provides a window for intramolecular rather than intermolecular EnT, which was previously proposed to promote efficient sensitization. Furthermore, two diastereometric catalyst-substrate complexes (**9a** and **9b**) were proposed as possible transition states with **9b** as the preferred transition state thus leading to efficient sensitization of the enantiomer in the catalyst-substrate complex (Scheme 8).[23b] Also utilizing the chiral thioxanthone **9** as an efficient EnT-catalyst, Bach and co-workers have reported the enantioselective Aza Paternò–Büchi reactions of quinaxolinones with styrenes,[24] and deracemization of primary allene amides.[25]
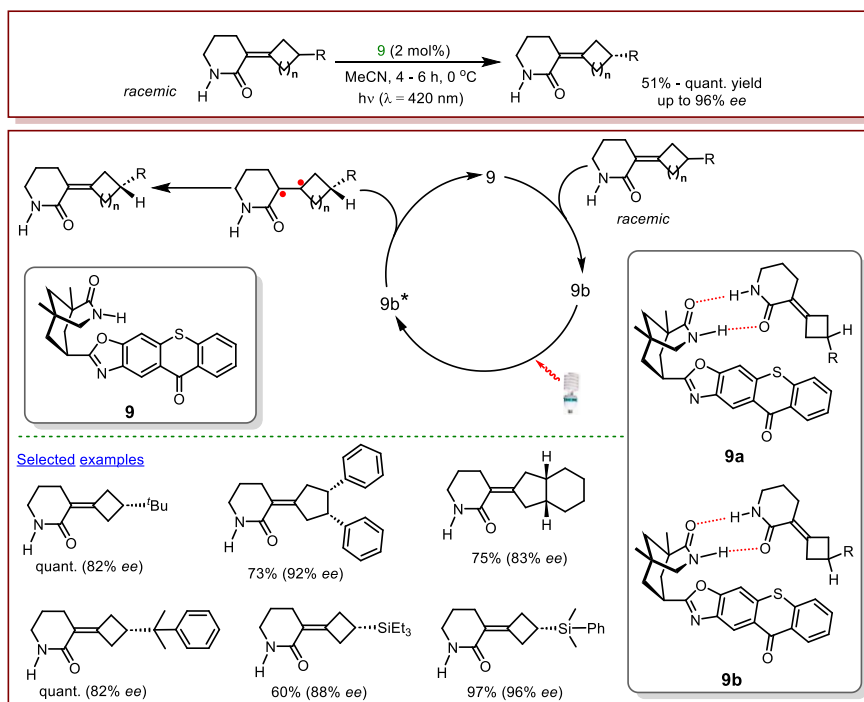
Scheme 8. Photochemical deracemization of alkenes via triplet EnT.[23b]

Bach and co-workers further expanded the toolbox for photochemical deracemization to hydantoins as substrates using the chiral benzophenone **10**.[26] The mechanism of the transformation, apart from the already established formation of catalyst-substrate complex which promotes EnT,[23b, 25] also includes a reversible HAT step which is crucial to the conversion of the racemate to the enantiomer observed as products. The authors have also recently reported a detailed theoretical and experimental study on the mechanistic steps involved in the deracemization reaction (Scheme 9).[26-27]
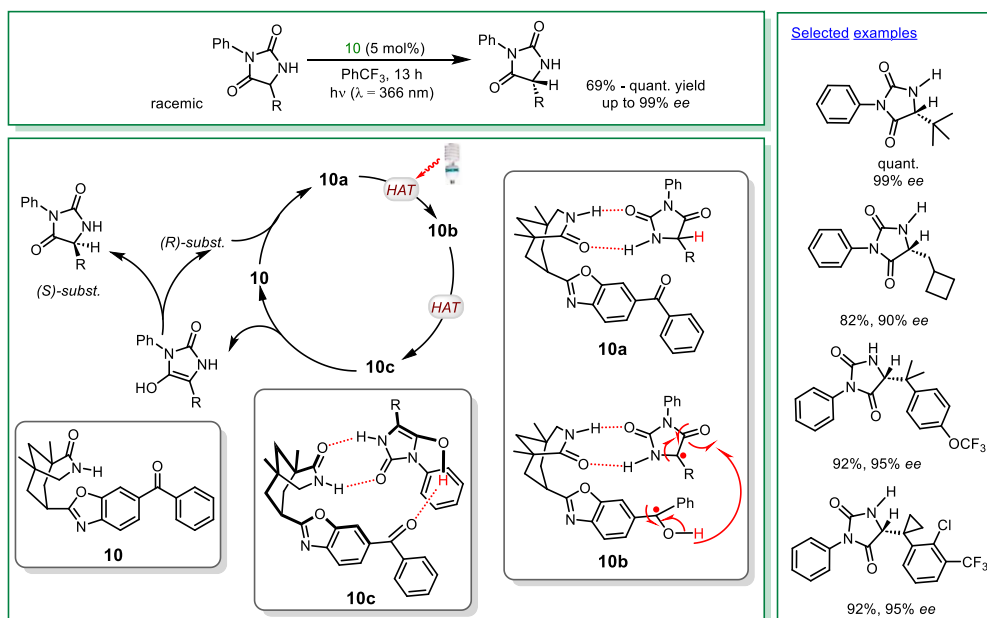
Scheme 9. Photochemical deracemization of hydantoins via triplet EnT. Mechanistic investigations were carried out with (−)-**10**.[26-27]

1.4 Dual Catalysis

For regio-, stereo- and enantio-selectivity, several catalytic platforms involving the combination of a photoredox catalyst, and TM complex, organic molecule or Lewis acid have been developed. In these catalyst systems, the photoredox catalyst or photoactive complex plays the role of generating radical intermediates via SET, EnT or VLIH. The co-catalyst on the other hand engages the radical intermediates and acts as the center for controlled bond formation.[1c, 1g, 2a, 6a, 16] This intriguing synergy has made formation of hitherto challenging bonds, control of reactive intermediates, access to enantio- and stereo-selective products, and multi-component reactions possible.

As earlier stated, the seminal report by Macmillan in 2008 described the possibility to merge photoredox and organo-catalysis (Scheme 1).[6a] Since 2008, MacMillan and co-workers have reported other transformations utilizing this dual mode of substrate activation.[14] Dual catalysis in photochemistry has been largely dominated by the merger of transition metal catalysts with photoredox catalysts. This area, termed *metallaphotoredox catalysis*, has become a toolbox for activation of difficult substrates and construction of challenging bonds.

1.4.1 Metallaphotoredox Catalysis

In 2007, Osawa and co-workers reported a photo assisted Sonogashira coupling by replacing the CuI co-catalyst in the conventional methodology with $Ru(bpy)_3^{2+}$ as EnT catalyst. The report which was the first to describe the merger of TM and photocatalysis led to improvements in the yields of the cross-coupling products as well as accelerated the rate of the reaction. Despite the observable improvements provided by light in the Sonogashira coupling compared to the conventional reaction, the utility of dual light- and TM catalyzed reactions was not explored further for several years.[28] In 2011, Sanford and co-workers revived interests in the merger of photoredox catalysis with TM catalysis when they reported the Pd- and photoredox catalyzed C–H arylation of 2-arylpyridine employing $Ru(bpy)_3^{2+}$ **2** as photocatalyst and aryldiazonium trifluoroborates as source of aryl-radical. In contrast to conventional methods which required high temperatures, the coupling reactions were performed at room temperature. The protocol was also amenable to a broad substrate scope and to different functional group. The authors thus provided the first mechanistic insights that photoredox catalysis could assist in activation of challenging substrates and improve electron transfer steps at metal centers when combined with TM catalysis.[29] Based on the foundation laid by Sanford and co-workers on the potentials of merging Pd-catalyst with photocatalysis, several methods were subsequently developed extending the applicability of the dual Pd-photoredox catalyzed reactions to aryl acylation, allylation, decarbonylation, carbonylation and carboxylation reactions as well as Heck-type reactions.[1c]

Despite the successes recorded with the dual Pd-photoredox catalyst platforms, attention quickly shifted to the use of first row transition metals which are more abundant in the earth crust. Amongst the first reports available in the literature is the merger of Cu and photoredox catalysis for the trifluoromethylation of boronic acids with CF_3I. The report by Sandford and co-workers exploited the ability of Cu^{II}-species to trap free radicals. The mechanism involves the excitation of $[Ru(bpy)_3]^{2+}$ and oxidation of the Cu^I-catalyst by the excited state *$[Ru(bpy)_3]^{2+}$ to generate Cu^{II}- and $[Ru(bpy)_3]^+$-species. SET from $[Ru(bpy)_3]^+$-species to CF_3I generates free CF_3 radicals and $[Ru(bpy)_3]^{2+}$-species. The CF_3-radical is then trapped by Cu^{II}

and the ensuing Cu^{III}-CF_3-species undergoes a base-promoted transmetalation with arylboronic acid, followed by reductive elimination to afford the desired product and Cu^I-species (Scheme 10).[30]
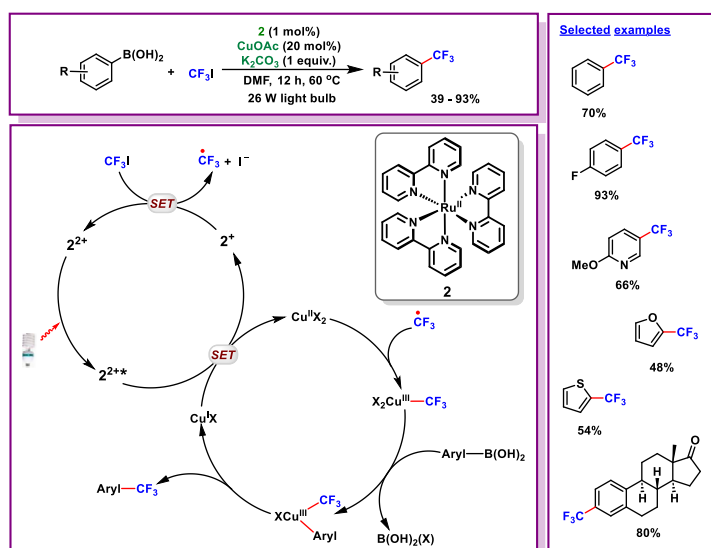
Scheme 10. Dual Cu- and photoredox catalyzed trifluoromethylation of aryl bronic acids.[30]

Ni-complexes have also found extensive use in dual photoredox and TM catalyzed reactions. The attraction to Ni is its tendency to undergo oxidative addition to C–halide (Br, Cl, I) bonds in its Ni^0 and Ni^I-states. Also, some Ni^{II} and Ni^{III}-complexes with suitable ligands are photoactive and can undergo VLIH; in the case of Ni^{II}-aryl species, excitation leads to long-lived ^3d-d excited state which ultimately results in the homolysis of the Ni^{II}-aryl bond. On the other hand, Ni^{III}-Cl species upon excitation can undergo MLCT transitions leading to the homolytic cleavage of the Ni^{III}-Cl/Br bond; in this case, the Cl/Br-radical generated can be used as an HAT catalyst. These properties of some Ni-complexes in various oxidative states and their behaviours when merged with photoredox catalysis have been exploited by the groups of Molander,[31] Doyle[32] and MacMillan[33] in the alkylation of aryl halides with ethers and decarboxylative alkylation of aryl halide.

Specifically, the generation of Cl-radical from Ni^{III}-Cl-species and its subsequently utility as an HAT-catalyst was described by Doyle and co-workers in the methylation of (hetero)aryl chlorides. The dual Ni- and photoredox catalytic tool which was used to generate methyl radicals from orthoformate provided a mild strategy for installation of methyl-groups on aromatic rings.[34] The methyl group is a moiety of significant importance in the pharmaceutical industry due to its role in improving bioavailability, metabolic stability and binding affinity of drugs.[35] The mechanism of the methylation reaction is detailed in Scheme 11.[34] Oxidative addition of Ni^0-species to aryl halide generates Ni^{II}-species which is oxidized by excited state Ir-photocatalyst to Ni^{III}-species. At this point, photoelimination of Cl-radical occurs from Ni^{III}-intermediate which abstracts a H-atom from trimethyl orthoformate to afford orthoformate radical. β-scission by the orthoformate radical liberates methyl radical which is then trapped by the Ni^{II}-aryl species. Finally, reductive elimination occurs at the Ni^{III}-methyl-aryl-intermediate to furnish the desired product, generate a Ni^I-species which is then reduced by Ir^{II}-intermediate to Ni^0-species.[34] This strategy has been extended to acetals as alcohol-derived radical source for methylation of aryl bromides and aziridines.[36]
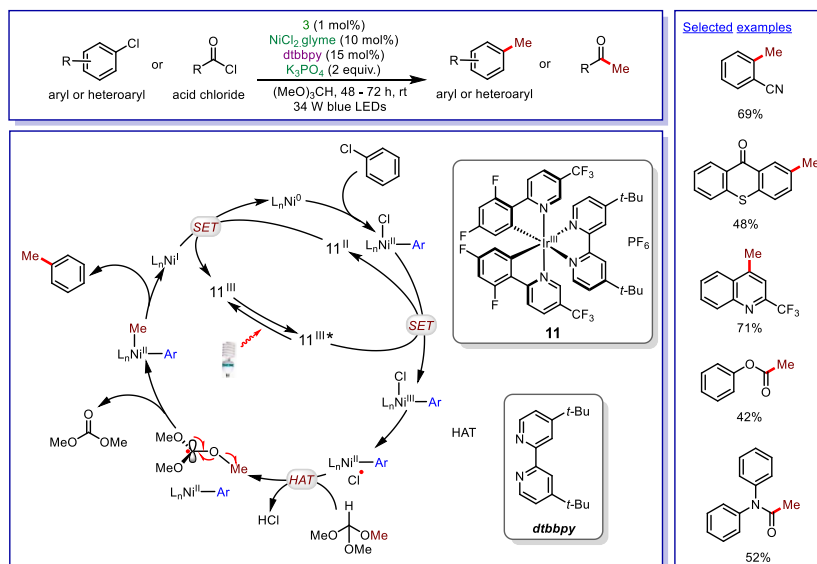
Scheme 11. Dual Ni and photoredox catalyzed methylation of aryl and acyl chlorides.[34]

Generally, metallaphotoredox catalysis involves the use of photocatalysts which engage in SET or EnT processes for radical generation and a TM cocatalyst as center for catalysis. This means a photocatalyst, usually of precious metals (Ir and Ru) or organic dyes is always required for substrate activation. However, the possibility to combine two earth-abundant transition metals, access other substrate activation pathways such as VLIH and regioselectively forge new bonds is not just mechanistically attractive but also of economic relevance. This was the case in the report by Gryko and co-workers who merged the photoactive vitamin B_{12} and $NiCl_2$ as catalysts in the photo-induced activation of epoxides and coupling with aryl halides. The authors reported that the supernucleophilic Co^I-species generated via reduction of vitamin B_{12} with Zn can engage in epoxide ring opening to produce Co^{III}-alkyl intermediate. Due to the weak Co^{III}–C bond,[37] the Co^{III}-alkyl intermediate undergoes VLIH upon excitation to furnish alkyl radical and Co^{II}-species. The alkyl radical then adds to Ni^{II}-aryl species generated upon oxidative addition of Ni^0 to aryl halide. Finally, reductive elimination at the Ni^{III}-intermediate yields the desired products. Due to the bulky nature of vitamin B_{12}, attack on the epoxide only occurs from the less sterically hindered side, hence the generation of radicals and products formation is regioselective (Scheme 12).[38] This strategy has also been extended to the activation of oxetanes and coupling with aryl halides.[39]
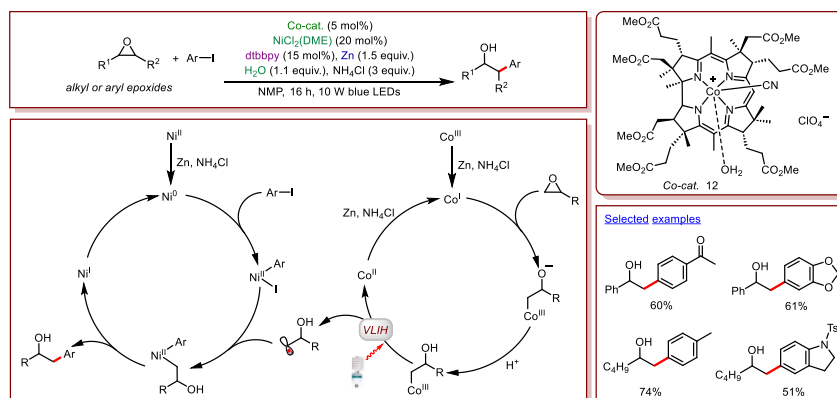
Scheme 12. Dual Co- and Ni-catalyzed regioselective ring opening of epoxides with aryl halides.[38]

1.5 Photoactive Complexes of Earth Abundant (3d) Transition Metals

Due to sustainability and economic concerns, there has been increased interest in the development of photocatalysts based on earth abundant transition metals. In this regard, complexes of Cr, Mn, Fe, Co, Ni and Cu, Zn have been investigated as potential alternatives to noble metal complexes of Ir and Ru. Photoactive complexes of 3d transition metals are advantageous since they are coordinatively unsaturated and can contain labile ligands, which allow for ligand exchange. The significance of this is that substrates and intermediates can directly interact with and bind the metal center. Mechanistically, these complexes are more elegant as they can engage in both outer- and inner-sphere electron transfer processes, thus offer different pathways for metal-ligand and/or substrate bond activation. The wide range of oxidation states accessible with 3d transition metals also makes the complexes attractive for catalysis as the different oxidation states could play divergent roles in catalytic cycles, thus obviating the need for dual catalyst systems (Scheme 13).
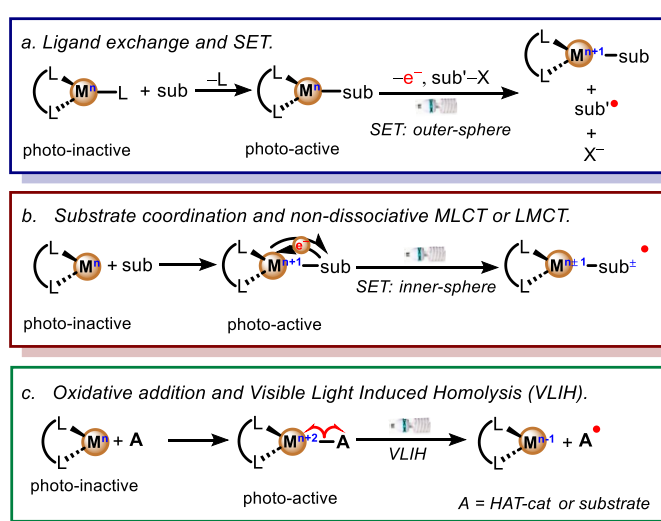
Scheme 13. Mechanistic paradigms accessible with photoactive 3d-metal complexes

Despite the above advantages and the possibility of unlocking new reactions with 3d metal complexes, the challenge of short-lived excited state lifetimes encountered with 3d metal analogues (e.g. [Fe(bpy)$_3$]$^{2+}$ **13**, Figure 3a)[40] of polypyridyl complexes of Ru and Ir slowed down progress in developing efficient photocatalysts based on these metals. If these complexes are intended for the traditional SET mechanistic pathways, then long-lived excited states species and high redox potentials are desirable. Except for Cu(I) with completely filled 3d subshell, other 3d transition metals with partially filled d-orbitals undergo undesirable fast MLCT excited state deactivation.[40b] This is due to the presence of energetically low-lying metal-centered (MC) states resulting from the partially filled d-orbitals, a situation which is not observed in heavier 4d and 5d transition metals (Figure 3 b and c).[40a] For example, the effect of the low-lying MC states is evident in the short-lived emission lifetime of [Fe(bpy)$_3$]$^{2+}$ with τ_{em} = 50 fs, compared to its noble metal analogue [Ru(bpy)$_3$]$^{2+}$ with τ_{em} = 5 μs and 850 ns at 77 K and room temperature respectively.[40b, 41]
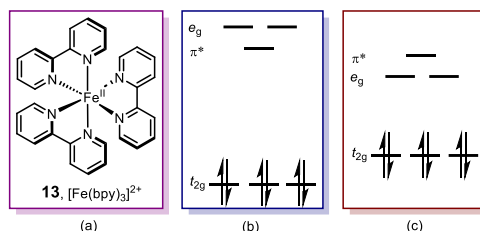
Figure 3. (a) $[Fe(bpy)_3]^{2+}$ **13** (b) Molecular orbital (MO) scheme for low spin d^6 metal complexes, e.g. Ru^{II} polypyridine, cyclometalated Ir^{III}, and related noble metal-based complexes (c) MO scheme for Fe^{II} polypyridines.[40a]

Another challenge encountered in the early development of photoactive complexes based on 3d transition metals was the excited state flattening distortion observed for example in bis-diimine Cu(I) complexes (e.g. $[Cu(phen)_2]^+$ **14**, Figure 4a). This phenomenon switches the geometry of bis-diimine Cu(I) complexes from tetrahedron-like D_{2d} structures in the ground (S_0) state to "flattened" square-planar-like structure in the excited state (Figure 4b). The import of this non-radiative decay pathway is the reduction in the excited state lifetime of the complex.[40b, 41a, 42]
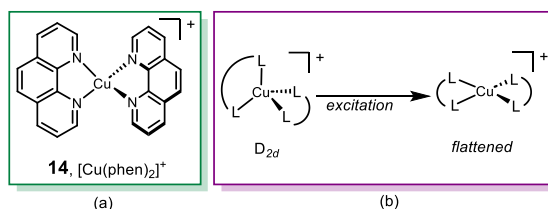
Figure 4. (a) $[Cu(phen)_2]^+$ **14**. (b) Flattening distortion observed upon excitation of **14**.

Even though there were initial setbacks encountered in developing photoactive 3d transition metal complexes, tremendous improvements have been made in increasing the excited state lifetimes and improving the redox potentials of photoactive 3d-TM complexes in recent years. The rationale to achieve long-lived excited states is to push the energy of the MC states higher. The strategies that have been adopted to realise this include increasing the steric bulk in the ligand backbone, strong σ-donor and/or π-acceptor ligands and incorporating electron-withdrawing and donating substituents on the ligand backbone to instigate push–pull effects.[40, 43] Examples of complexes that have been developed by implementing the aforementioned strategies are shown in Figure 5.
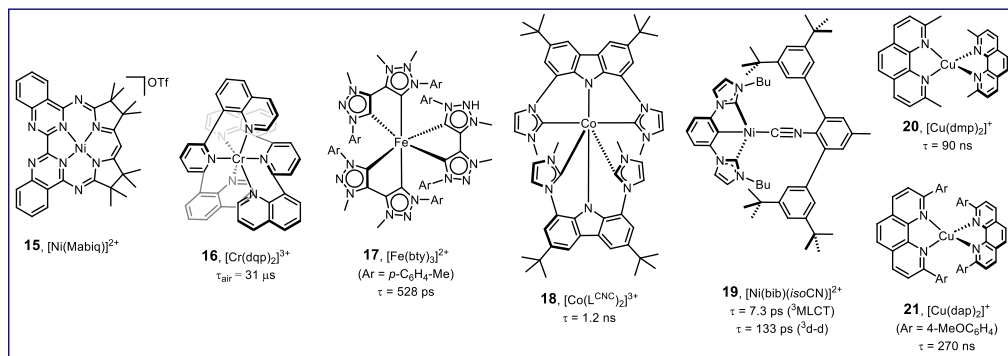
Figure 5. Examples of 3d transition metal complexes with appreciably long-lived excited state lifetimes.

1.5.1 Photoinduced SET Reactions Catalyzed by 3d TM Complexes

Having achieved significant improvements in developing photoactive complexes of 3d metals with long-lived excited states and high redox potentials, several bond forming reactions utilizing these complexes have been developed. In reactions reported in the literature, the complexes performed favourably as their 4d and 5d (Ru and Ir) counterparts earlier utilized for such reactions. The Hess and Bach group in 2018 collaborated and developed a Ni^{II}-complex based on the non-innocent macrocyclic biquinazoline (Mabiq) ligand and explored the redox and photocatalytic properties of the complex.[43b] The authors reported that the Ni^{II}-Mabiq **15** complex can be photoreduced in the presence of amines as sacrificial electron donors and estimated an excited state redox potential of ≥ 1.25 V vs SCE. The excited state oxidative properties of **15** were then explored in the cyclization of bromoalkyl-substituted indoles, a reaction already demonstrated by Stephenson and co-workers with $[Ru(bpy)_3]^{2+}$ **2**.[44] However, **15** outperformed **2**, with product yields as high as 97% depending on the sacrificial electron donor used. The mechanism of the reaction is similar to that reported for **2**, which includes excitation of **15** followed by reductive quenching of the excited state photocatalyst by Et_3N. The reduced **15**-species then undergoes SET to the bromoalkyl-substrate to generate the alkyl radical. Cyclization of the radical, oxidation of the ensuing benzylic radical and elimination of H^+ or HBr affords the desired product (Scheme 14).[43b, 44]
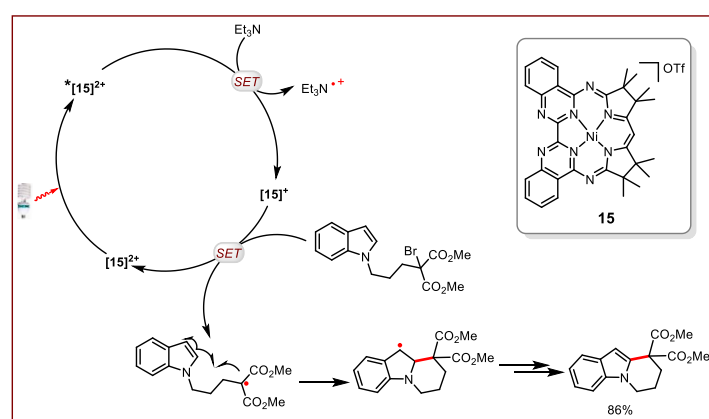
Scheme 14. Ni^{II}-Mabiq **15** photocatalyzed cyclization of bromoalkyl-substituted indole. *Ni^I-Mabiq (i.e. [15]$^+$ is a formal notation. The active species generated upon SET from Et$_3$N is $Ni^{II}(Mabiq^\bullet)$).*[43b]

In 2022, Wenger and co-workers reproduced the photocatalytic aerobic hydroxylation of arylboronic acids and pinacol esters to phenols with $[Cr(dqp)_2]^{2+}$ **16**.[43c] Although this reaction had already been achieved with $[Ru(bpy)_3]^{2+}$ **2**[45] and methylene blue[46], they reported $91 - 99\%$ yield of the phenols in $4 - 6$ hours of irradiation in the presence of DIPEA as a sacrificial electron donor and O_2 as oxidant. The mechanism reported, which is the same as what has been reported with **2**, involves the SET from DIPEA to the excited Cr^{III}-complex. The generated Cr^{II}-intermediate is then oxidized by O_2 to regenerate Cr^{III}-species and superoxide anion. The superoxide anion then reacts with boronic acid to furnish the peroxo-boronic intermediate which abstracts a proton from the oxidized DIPEA. Finally, rearrangement, hydroxyl elimination and hydrolysis furnished the desired phenol product (Scheme 15).[43c]
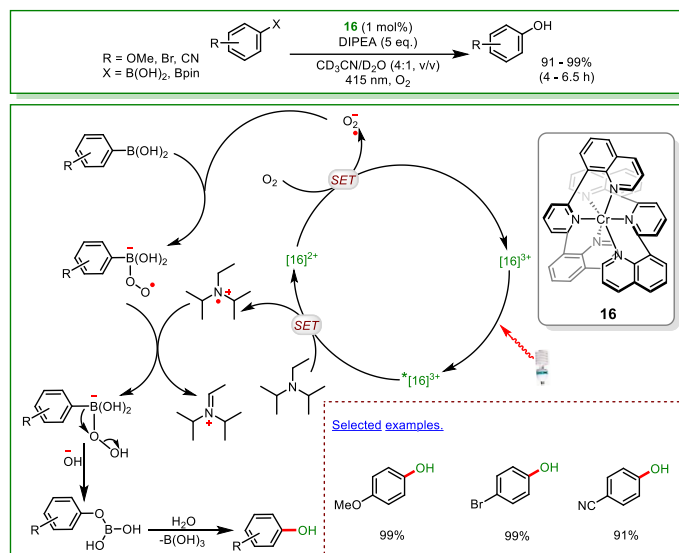
Scheme 15. Photocatalytic oxidation of arylboronic acids and pinacol esters to phenols.[43c]

Changing the ligand system from bpy to btz in Fe-complexes improved the excited state lifetime and redox potential of the complexes from τ = 50 fs ([Fe(bpy)$_3$]$^{2+}$ **13**) to τ = 528 ps (E(Fe$^{III*/II}$) = +1.94 V; E(Fe$^{III/II}$) = –0.13 V; Fe(btz)$_3$ **17**). This opened a window for utilizing Fe-complexes for photoinduced SET reactions. Accordingly, Kang and co-workers demonstrated the efficiency of **17** in the photoinitiated radical [4+2] cycloaddition reaction of styrenes with dienes.[47] The cycloaddition reaction reported by Kang and co-workers had earlier been demonstrated by Yoon and co-workers with [Ru(bpz)$_3$]$^{2+}$,[48] hence similar catalytic cycle was proposed as shown in Scheme 16. The mechanistic aspects of the reaction involve the excitation of the catalyst which results in LMCT followed by SET from the styrene (E_{ox} = +1.27 V) to the excited Fe-complex (E(Fe$^{III*/II}$) = +1.94 V). The SET generates a styrene radical cation and a reduced Fe^{II}-species. Addition and cyclization reaction then occurs between the styrene radical cation and diene furnishing a cylcohexene radical cation. Reduction of the cylcohexene radical cation by Fe^{II}-species turns over the Fe^{III}-catalyst and furnishes the desired product. According to Kang and co-workers, high yields were obtained under aerated condition. They claimed this could be due to ET from the excited Fe^{III}-catalyst to singlet oxygen to produce O$_2$$^{•–}$ and the O$_2$$^{•–}$ subsequently transferred an electron to the cyclohexene radical cation to furnish the desired product (Scheme 16).[47]
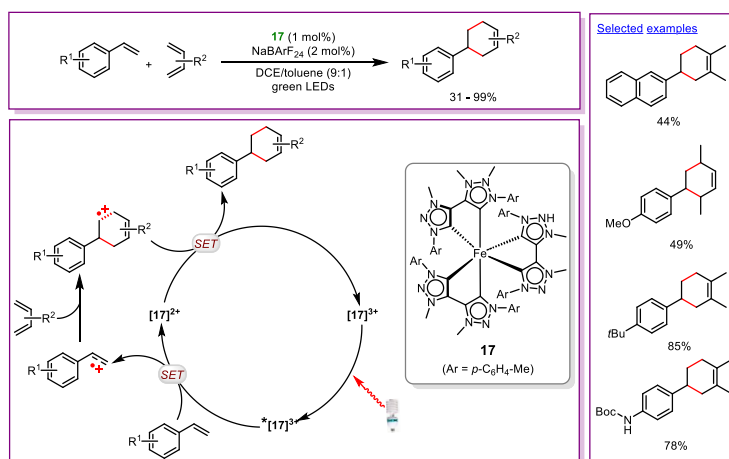
Scheme 16. [Fe(btz)$_3$]$^{2+}$ photocatalyzed [4+2] cycloaddition.[47]

1.5.2 Beyond SET and EnT: VLIH in 3d TM Complexes

As stated earlier, the attraction to 3d transition metal photoactive complexes goes beyond just economic and sustainability reasons. The unique mechanistic pathways accessible with these complexes as shown in Scheme 13 provides opportunities to form new bonds which are challenging with SET and EnT pathways. Also worth noting is the possibility to generate in situ photoactive complexes with 3d metals by ligand dissociation and substrate coordination steps.[1h] Exploiting the uniqueness of 3d metal complexes, several intriguing catalytic methodologies have been developed including the use of very common 3d metal salts as sources of radicals (e.g. Cl•) which can act as HAT catalysts. As far back as 1962, Kochi already observed the photolysis of Cu–Cl bond in $CuCl_2$ upon irradiation with a Hg lamp. He exploited this observation in the oxidation of alcohols to ketones and the chlorination of alkenes.[49] More recently, Rovis and co-workers demonstrated that with the same catalytic platform shown by Kochi, the alkylation of alkanes with electron deficient alkenes which served as radical acceptors was possible. Their mechanistic proposal includes the generation of Cl• via LMCT and VLIH of a Cu–Cl bond upon irradiation of a mixture of $CuCl_2$ and LiCl in MeCN. The Cl• abstracts an H-atom from an alkane, followed by addition of the ensuing alkyl radical to an electron-deficient alkene. Subsequent steps in the catalytic cycle include metallation, tautomerization and protodemetallation to afford the desired product (Scheme 17).[50]
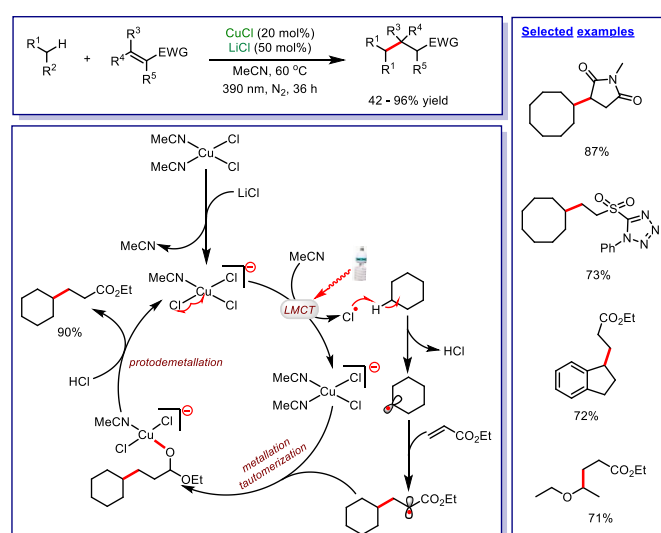
Scheme 17. Photoinduced $CuCl_2$-catalyzed alkylation of alkanes with electron-deficient alkenes.[50]

Also exploiting the LMCT properties of photoactive Cu-species, MacMillan and co-workers reported the decarboxylative halogenation and borylation of hetero(aryl) acids. The in situ generated photoactive Cu^II-carboxylate species is formed via coordination of deprotonated carboxylic acid to the Cu^I-salt followed by oxidation to Cu^II-carboxylate. Upon excitation, the Cu^II-carboxylate engages in an LMCT, which results in the formation of an aryloxyl radical and Cu^I-species. The aryloxyl radical then extrudes CO_2 and the aryl radical formed is proposed to (a) engage in an atom transfer with the halide (I and Br) source or (b) via a Cu-mediated coupling is trapped by an already generated Cu-halide (Cl and F) intermediate followed by reductive elimination of the desired product. In the case of the borylation, in situ generated activated metal boronates deliver the –Bpin-moiety unto the aryl radical (Scheme 18).[51]
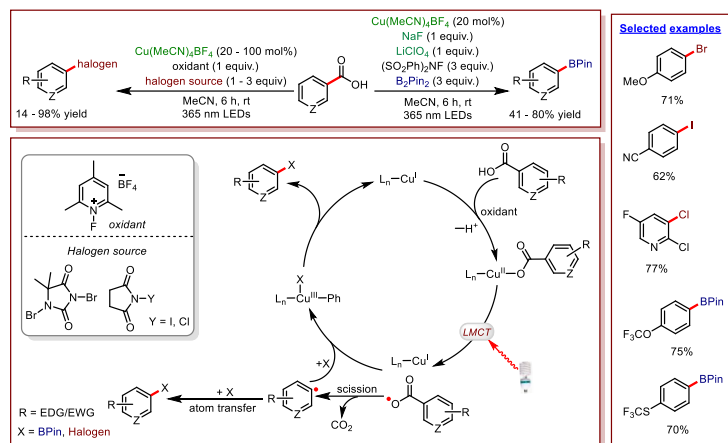
Scheme 18. Photoinduced decarboxylative halogenation and borylation of hetero(aryl) acids.[51]

Similarly, in situ generated photoactive Fe-species which undergo LMCT excited state transitions have also been employed in the generation of radical intermediates and for forging new bonds.[52] These species which are accessible via coordination of substrates such as alcohols and carboxylic acids to simple Fe-salts (with or without added ligands) upon irradiation undergo inner-sphere CT which results in VLIH.[53] Specifically, Zeng and co-workers reported the remote amination of alcohols via Fe-alkoxide photoinduced 1,5-HAT. The mechanism of the transformation involves coordination of alcohol to Fe(III) and the ensuing Fe-alkoxide intermediate undergoes a VLIH to generate alkoxide radical intermediate. Intramolecular 1,5-HAT by the alkoxide radical furnishes a C-centered radical which then adds on to DBAD to afford an N-centered radical species. Finally, SET from Fe(II)-intermediate to the N-centered radical species affords the desired product and regenerates the Fe(III)-catalyst. With the methodology, a range of alcohols were efficiently aminated in 26 − 92% yield (Scheme 19).[53a]
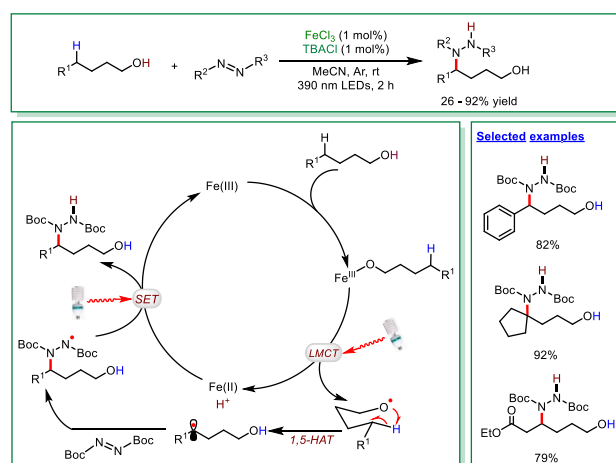
Scheme 19. Photoinduced Fe-catalyzed amination of alcohols.[53a]

Photoactive Co[III]-complexes are also efficient sources of C–centered radicals due to the weak Co–C bond (14 − 45 kcal mol^{-1}) in such molecules. Although organocobalt complexes have been predominantly employed in light induced radical polymerization,[37a] the complexes have recently come to limelight in photoinduced organic reactions due to the unique catalytic roles of the three oxidation states of four-coordinated cobalt complexes.[1h] The "supernucleophilic"

Co[I], metalloradical Co[II], organo-, and hydro-Co[III]–species are all accessible in situ. The supernucleophilic Co[I]–species can undergo oxidative addition to alkyl or acyl halides, acyl thiols and bicyclic compounds to generate the corresponding photoactive organocobalt(III)–species.[54] When irradiated or subjected to significant amount of heat, the Co[III]–species undergo VLIH of Co–C bond to generate C–centered radicals and metalloradical Co[II]–species. The metalloradical Co[II]–species is capable of trapping in situ generated radicals, hence plays the key role of reducing the amounts of free radicals as well as facilitate regiocontrol in situations where rebound of radical species formed from radical addition or HAT to alkenes is feasible.[55]

In this regard, a handful of photoactive Co-complexes have been developed and utilized in photoinduced C-centered radical generation and bond formation. Organocobalt complexes such as Co-salen,[55a, 55b] Co-salophen[56] and the naturally occurring vitamin B_{12}[37b] are most often reported in the literature as efficient sources of C-centered radical. The generation of C-centered radicals using Vitamin B_{12} in particular has been demonstrated extensively by Gryko and co-workers.[37b] In 2020, they reported the alkylation of strained bicycloalkanes (BCBs) with electron deficient alkenes in a catalytic process through which the BCB is activated by in situ generated supernucleophilic Co[I]. The Co[III]-BCB anion intermediate is first protonated and upon excitation undergoes VLIH to afford a BCB-radical and Co[II]. BCB Radical addition to electron deficient alkenes and protonation by NH_4Cl affords the desired product. To generate the Co[I]-species, stoichiometric amounts of Zn, which acts as a reductant is required.[54a] The yields of the products ranged from 44 – 98% (Scheme 20).
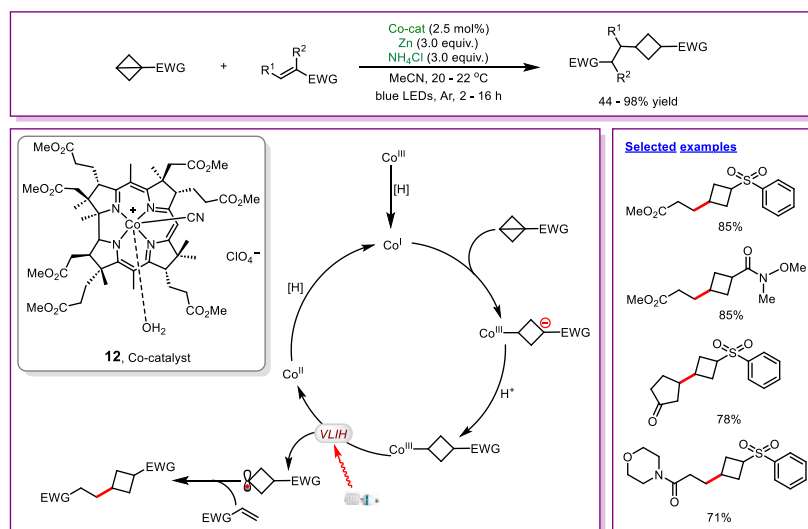
Scheme 20. Photoinduced Co-catalyzed alkylation of bicyclobutanes with electron-deficient alkenes.[54a]

1.6 Aim and Scope of Research

The development of photoinduced earth-abundant transition metal catalyzed reactions has become very popular in recent years as the use of expensive Ir- and Ru-photocatalysts become less appealing due to economic and sustainability concerns. Additionally, the possibility to open new mechanistic paradigms with photoactive 3d complexes which are predominantly unsaturated, contain labile ligands and hence can engage in inner- and outer-sphere reactions also makes them very appealing for photoinduced reactions. Beyond the conventional photoinduced SET and ET pathways for generating reactive radical intermediates, the VLIH pathway, which is characteristic to 3d transition metals provides opportunities for activation of strong bonds and forging of hitherto challenging bonds. These advantages of photoactive 3d TM complexes have thus led to the development of several intriguing photoinduced reactions by employing 3d TM complexes that could serve as alternatives to Ir- and Ru-photocatalysts both for small molecule activation and cross-coupling reactions.

In this regard, the Hess Group has been exploring the photocatalytic properties of 3d TM complexes based on the macrocyclic Mabiq ligand (Mabiq = 2−4:6−8-bis(3,3,4,4-tetramethyldihydropyrrolo)-10−15-(2,2'-biquinazolino)-[15]-1,3,5,8,10,14-hexaene-1,3,7,9, 11,14-N$_6$). Following the successful synthesis and characterization of M^n-Mabiq complexes (n = 0 → +3) of Fe, Co, Ni, Cu and Zn,[57] the group went further to investigate the redox and photocatalytic properties of Ni(Mabiq). The findings of the report, which is among the first examples of a photoredox catalyst based on Ni, have already been summarized in section 1.5.1 (Scheme 14).[43b] In this context, we focused on expanding the utility of M-Mabiq complexes, shown in Figure 6, for photoinduced reactions.

15, Ni(Mabiq)OTf   **22**, X = H, Co(Mabiq)Cl$_2$ **24**, Co(Mabiq)Cl   **25**, Co(Mabiq)   **26**, Zn(Mabiq)OTf
23, X = Br, Co(MabiqBr)Cl$_2$
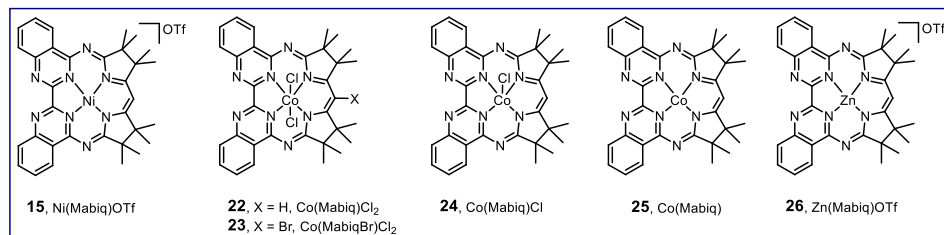
Figure 6. M–Mabiq complexes used in this work.

Thus, the primary aim of this work was to further explore the potentials of M–Mabiq complexes as efficient photocatalysts and the mechanistic pathways which can be accessible with the complexes since the ligand is redox active. As earlier stated, the attraction to earth-abundant complexes as photoredox catalysts, apart from the economic and sustainability concerns, also includes the myriads of substrate activation modes and mechanistic pathways which can be accessible with such complexes, that are not feasible with Ir- and Ru-photocatalysts. Photoredox catalysis with Ir- and Ru-complexes solely involve excited state SET or EnT, which are highly dependent on the lifetimes, redox potentials, and excited state energy of the photocatalyst. Thus, the excited state species are required to be long lived and highly oxidizing or reducing to engage in outer sphere substrate activation.[1] However, with 3d-TM complexes, other possibilities that aid SET are feasible. Such possibilities, which include π-π-stacking and substrate pre-association improves SET by bringing the substrate closer to the catalyst, thus resulting in somewhat inner sphere SET rather than outer sphere SET. Hence, even when the first row TM photocatalyst has short-lived excited state lifetime and low redox

potential, such catalyst might still facilitate SET or EnT processes.[40b, 41a] Another disadvantage of the potent Ir- and Ru-photocatalysts is the lack of control of the ensuing reactive radical intermediates upon SET. As a result, for regio-, diastereo- and/or enantio-control of products, additional catalysts, e.g. 3d-metal complexes, are required. For example, the intermolecular oxidative hydrofunctionalization reported by Zhu and co-workers[55a] required the combination of a [Ru(bpy)$_3$]$^{2+}$ as photocatalyst, Co-salen for regiocontrol and alkene activation, and stoichiometric amount of silanes as H-atom donor to effect Markovnikov-selective functionalization of indazoles, imidazoles, and pyrazoles with styrenes. Although the protocol provided a mild dual Co- and photoredox catalyzed method for the functionalization of medicinally relevant indazoles and imidazoles, the catalyst system still fell short of being referred to as an overall atom economical and sustainable approach. Thus, the development of an even more robust method that would employ a single catalyst that can play the roles of a photocatalyst and metal centre for catalysis was desirable. To achieve this, a redox active ligand capable of supporting a first-row TM in its variable oxidation states is required. Intriguingly, we developed a catalytic method in which the Co-Mabiq complex **23** could act as both the photoredox catalyst and the metal center for regiocontrol of product. Our study revealed that the Co-Mabiq complex **23** can catalyze the Markovnikov-selective alkylation of indoles and indazoles without the requirement for a co-catalyst, an oxidant, or a H-atom donor. The catalyst **23** thus adopted several roles in the catalytic cycle, i.e. induced SET upon excitation, and intercepted radical intermediates, thereby ensuring regioselective product formation in the presence of nucleophiles (Scheme 21).
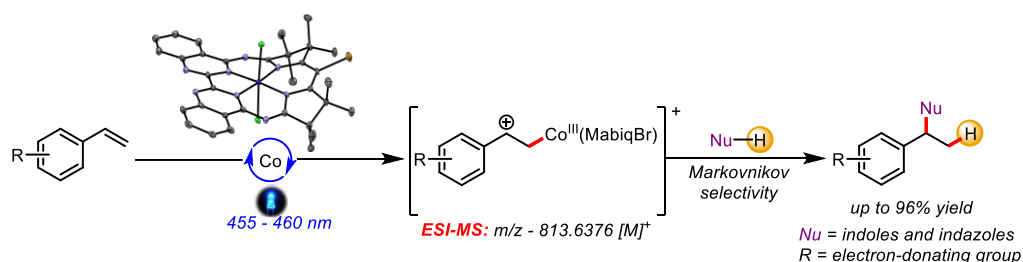
Scheme 21. Molecular structure of Co-Mabiq-Br and photoinduced reactions catalyzed by the complex.

Furthermore, substrate activation via coordination or oxidative addition, which do not involve excited state SET or EnT are hardly observed with Ru- and Ir-photocatalysts. However, these mechanistic steps which precede VLIH, a mechanistic event that furnish radical species is feasible with some photoactive Ni- and Co-complexes. These substrate activation pathways eliminate the challenge of mismatch of redox potentials and triplet energy encountered with conventional photoredox catalysts. For example, the photocatalytic generation of acyl radicals from acid chlorides, carboxylic acids, aldehydes, or α-keto acids require the use of a combination of highly oxidizing Ru- or Ir-photocatalysts and radical initiator. Also, the ensuing acyl radical, which is nucleophilic, only undergoes radical addition to electron-deficient alkenes as there is no further interaction of the radical with the photocatalyst. To solve this challenge, pre-functionalization of the alkene is required. Additionally, for Heck-type coupling of acyl radicals to alkenes, additional co-catalyst such as oxidants, a base, or a 3d-TM-catalyst is required for double-bond retention. In general, these types of transformations require careful selection of photocatalyst, co-catalysts and a wide range of other additives.[12c]

The above challenges encountered with the generation of acyl radical and controlled addition to alkenes can be solved with careful development of a photoactive 3d-TM metal complex with suitable ligand architecture that predisposes the catalyst to different oxidation states in which the catalyst can adopt several roles. Indeed, the Co-Mabiq can catalyze the activation and controlled addition of acyl radicals to styrenes, furnishing Heck-type products with both electron-rich and electron-deficient styrenes. The reactivity of the Co-Mabiq complexes involves the different oxidative states supported by the redox active Mabiq ligand, i.e. Co^I – Co^{III}, with each playing different roles in the catalytic cycle (Figure 9). Hence, leveraging on the ability to photo-reduce the Co^{II}-Mabiq to $Co^{II}(Mabiq^•)$ *(formally denoted as Co^I-Mabiq)* and the subsequent oxidative addition of the Co^I-Mabiq to acyl chloride, photoactive acyl Co^{III}-Mabiq intermediate was formed. Although the subsequent steps, which include VLIH of the Co^{III}-acyl bond and addition to styrenes appeared straightforward, the products formed (unsaturated ketones) suggested a secondary involvement of the Co-Mabiq catalyst. This direct approach to activation of acyl halides via elementary oxidative addition step and subsequent controlled generation and addition of the acyl radicals to alkenes typifies the uniqueness of the Co-Mabiq complex (Scheme 22).
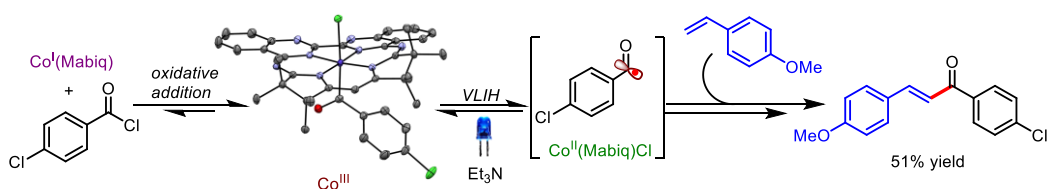
Scheme 22. Co-Mabiq catalyzed acylation of styrenes.

1.7 References

1. (a) Yan, M.; Lo, J. C.; Edwards, J. T.; Baran, P. S., Radicals: Reactive Intermediates with Translational Potential. *J. Am. Chem. Soc.* **2016**, *138* (39), 12692-12714; (b) Marzo, L.; Pagire, S. K.; Reiser, O.; König, B., Visible-Light Photocatalysis: Does It Make a Difference in Organic Synthesis? *Angew. Chem. Int. Ed.* **2018**, *57* (32), 10034-10072; (c) Chan, A. Y.; Perry, I. B.; Bissonnette, N. B.; Buksh, B. F.; Edwards, G. A.; Frye, L. I.; Garry, O. L.; Lavagnino, M. N.; Li, B. X.; Liang, Y.; Mao, E.; Millet, A.; Oakley, J. V.; Reed, N. L.; Sakai, H. A.; Seath, C. P.; MacMillan, D. W. C., Metallaphotoredox: The merger of photoredox and transition metal catalysis. *Chem. Rev.* **2022,** *122* (2), 1485-1542; (d) Prier, C. K.; Rankic, D. A.; MacMillan, D. W., Visible light photoredox catalysis with transition metal complexes: applications in organic synthesis. *Chem. Rev.* **2013,** *113* (7), 5322-5363; (e) Rivas, M.; Palchykov, V.; Jia, X.; Gevorgyan, V., Recent advances in visible light-induced C(sp^3)-N bond formation. *Nat. Rev. Chem.* **2022,** *6* (8), 544-561; (f) Shaw, M. H.; Twilton, J.; MacMillan, D. W., Photoredox Catalysis in Organic Chemistry. *J. Org. Chem.* **2016,** *81* (16), 6898-6926; (g) Twilton, J.; Le, C.; Zhang, P.; Shaw, M. H.; Evans, R. W.; MacMillan, D. W. C., The merger of transition metal and photocatalysis. *Nat. Rev. Chem.* **2017,** *1* (7), 1-18; (h) Abderrazak, Y.; Bhattacharyya, A.; Reiser, O., Visible-Light-Induced Homolysis of Earth-Abundant Metal-Substrate Complexes: A Complementary Activation Strategy in Photoredox Catalysis. *Angew. Chem. Int.* **2021,** *60* (39), 21100-21115; (i) Holmberg-Douglas, N.; Nicewicz, D. A., Photoredox-Catalyzed C-H Functionalization Reactions. *Chem. Rev.* **2022,** *122* (2), 1925-2016; (j) Romero, N. A.; Nicewicz, D. A., Organic photoredox catalysis. *Chem. Rev.* **2016,** *116* (17), 10075-10166; (k) McAtee, R. C.; McClain, E. J.; Stephenson, C. R. J., Illuminating Photoredox Catalysis. *Trends Chem.* **2019,** *1* (1), 111-125; lNarayanam, J. M.; Stephenson, C. R., Visible light photoredox catalysis: applications in organic synthesis. *Chem. Soc. Rev.* **2011,** *40* (1), 102-113.

2. (a) Grosskopf, J.; Kratz, T.; Rigotti, T.; Bach, T., Enantioselective Photochemical Reactions Enabled by Triplet Energy Transfer. *Chem. Rev.* **2022,** *122* (2), 1626-1653; (b) Capaldo, L.; Ravelli, D.; Fagnoni, M., Direct Photocatalyzed Hydrogen Atom Transfer (HAT) for Aliphatic C-H Bonds Elaboration. *Chem. Rev.* **2022,** *122* (2), 1875-1924; (c) Bell, J. D.; Murphy, J. A., Recent advances in visible light-activated radical coupling reactions triggered by (i) ruthenium, (ii) iridium and (iii) organic photoredox agents. *Chem. Soc. Rev.* **2021,** *50* (17), 9540-9685.

3. Hohmann-Marriott, M. F.; Blankenship, R. E., Evolution of photosynthesis. *Annu. Rev. Plant Biol.* **2011,** *62*, 515-548.

4. (a) Chen, M.; Schliep, M.; Willows, R. D.; Cai, Z. L.; Neilan, B. A.; Scheer, H., A red-shifted chlorophyll. *Science* **2010,** *329* (5997), 1318-9; (b) Chew, A. G.; Bryant, D. A., Chlorophyll biosynthesis in bacteria: the origins of structural and functional diversity. *Annu. Rev. Microbiol.* **2007,** *61*, 113-129.

5. Johnson, M. P., Photosynthesis. *Essays Biochem.* **2016,** *60* (3), 255-273.

6. (a) Nicewicz, D. A.; MacMillan, D. W., Merging Photoredox Catalysis with Organocatalysis: The Direct Asymmetric Alkylation of Aldehydes. *Science* **2008,** *322* (5898), 77-80; (b) The Royal Swedish Academy of Sciences. The Nobel Prize in Chemistry 2021. *www.nobelprize.org*.

7. Ischay, M. A.; Anzovino, M. E.; Du, J.; Yoon, T. P., Efficient Visible Light Photocatalysis of [2+2] Enone Cycloadditions. *J. Am. Chem. Soc.* **2008,** *130*, 12886–12887.

8. Narayanam, J. M. R.; Tucker, J. W.; Stephenson, C. R. J., Electron-Transfer Photoredox Catalysis: Development of a Tin-Free Reductive Dehalogenation Reaction. *J. Am. Chem. Soc.* **2009,** *131*, 8756–8757.

9. Bach, T.; Hehn, J. P., Photochemical Reactions as Key Steps in Natural Product Synthesis. *Angew. Chem. Int. Ed.* **2011,** *50* (5), 1000-1045.

10. Yoon, T. P.; Ischay, M. A.; Du, J., Visible Light Photocatalysis as a Greener Approach to Photochemical Synthesis. *Nat. Chem.* **2010,** *2* (7), 527-532.

11. Donaldson, D. J.; George, C.; Vaida, V., Red Sky at Night: Long-wavelength Photochemistry in the Atmosphere. *Environ. Sci. Technol.* **2010,** *44*, 5321-5326.

12. (a) Zhou, Q. Q.; Zou, Y. Q.; Lu, L. Q.; Xiao, W. J., Visible-Light-Induced Organic Photochemical Reactions through Energy-Transfer Pathways. *Angew. Chem. Int. Ed.* **2019,** *58* (6), 1586-1604; (b) Strieth-Kalthoff, F.; Glorius, F., Triplet Energy Transfer Photocatalysis: Unlocking the Next Level. *Chem.*

2020, *6* (8), 1888-1903; (c) Banerjee, A.; Lei, Z.; Ngai, M. Y., Acyl Radical Chemistry via Visible-Light Photoredox Catalysis. *Synthesis (Stuttg)* **2019,** *51* (2), 303-333.

13. (a) Kalyanasundaram, K., Photophysics, Photochemistry and Solar Energy Eonversion with Tris(bipyridyl)ruthenium(II) and its Analogues. *Coord. Chem. Rev.* **1982,** *46*, 159-244; (b) Juris, A.; Balzani, V.; Barigelletti, F.; Campagna, S.; Belser, P.; Zelewsky, A. v., Ru(II) Polypyridine Complexes: Photophysics, Photochemistry, Electrochemistry, and Chemiluminescence. *Coord. Chem. Rev.* **1988,** *84*, 85-277.

14. (a) Nagib, D. A.; Scott, M. E.; MacMillan, D. W. C., Enantioselective a-Trifluoromethylation of Aldehydes via Photoredox Organocatalysis. *J. Am. Chem. Soc.* **2009,** *131*, 10875–10877; (b) Shih, H.-W.; Wal, M. N. V.; Grange, R. L.; MacMillan, D. W. C., Enantioselective a-Benzylation of Aldehydes via Photoredox Organocatalysis. *J. Am. Chem. Soc.* **2010,** *132*, 13600–13603.

15. Du, J.; Skubi, K. L.; Schultz, D. M.; Yoon, T. P., A Dual-Catalysis Approach to Enantioselective [2 + 2] Photocycloadditions using Visible Light. *Science* **2014,** *344*, 392-396.

16. Skubi, K. L.; Blum, T. R.; Yoon, T. P., Dual Catalysis Strategies in Photochemical Synthesis. *Chem. Rev.* **2016,** *116* (17), 10035-10074.

17. (a) Wang, C. S.; Dixneuf, P. H.; Soulé, J. F., Photoredox Catalysis for Building C-C Bonds from C(sp(2))-H Bonds. *Chem. Rev.* **2018,** *118* (16), 7532-7585; (b) Yu, X. Y.; Chen, J. R.; Xiao, W. J., Visible light-driven radical-mediated C-C bond cleavage/functionalization in organic synthesis. *Chem. Rev.* **2021,** *121* (1), 506-561.

18. (a) Klauck, F. J. R.; Yoon, H.; James, M. J.; Lautens, M.; Glorius, F., Visible-Light-Mediated Deaminative Three-Component Dicarbofunctionalization of Styrenes with Benzylic Radicals. *ACS Catal.* **2018,** *9* (1), 236-241; (b) Yi, J.; Badir, S. O.; Alam, R.; Molander, G. A., Photoredox-Catalyzed Multicomponent Petasis Reaction with Alkyltrifluoroborates. *Org. Lett.* **2019,** *21* (12), 4853-4858; (c) Zhang, M.; Zhang, J.; Zhou, Y.; He, Y.; Wu, J.; Zheng, D., Photoredox-Catalyzed Three-Component Amidoheteroarylation of Unactivated Alkenes. *Org. Lett.* **2023,** *25* (22), 4113-4118.

19. Forster, D.; Guo, W.; Wang, Q.; Zhu, J., Photoredox Catalytic Three-Component Amidoazidation of 1,3-Dienes. *ACS Catal.* **2021,** *11* (17), 10871-10877.

20. Poplata, S.; Troster, A.; Zou, Y. Q.; Bach, T., Recent Advances in the Synthesis of Cyclobutanes by Olefin [2 + 2] Photocycloaddition Reactions. *Chem. Rev.* **2016,** *116* (17), 9748-815.

21. Kleinmans, R.; Dutta, S.; Ozols, K.; Shao, H.; Schafer, F.; Thielemann, R. E.; Chan, H. T.; Daniliuc, C. G.; Houk, K. N.; Glorius, F., ortho-Selective Dearomative [$2\pi + 2\sigma$] Photocycloadditions of Bicyclic Aza-Arenes. *J. Am. Chem. Soc.* **2023,** *145* (22), 12324-12332.

22. Liang, Y.; Kleinmans, R.; Daniliuc, C. G.; Glorius, F., Synthesis of Polysubstituted 2-Oxabicyclo[2.1.1]hexanes via Visible-Light-Induced Energy Transfer. *J. Am. Chem. Soc.* **2022,** *144* (44), 20207-20213.

23. (a) Müller, C.; Bauer, A.; Bach, T., Light-Driven Enantioselective Organocatalysis. *Angew. Chem. Int. Ed.* **2009,** *48* (36), 6640-6642; (b) Kratz, T.; Steinbach, P.; Breitenlechner, S.; Storch, G.; Bannwarth, C.; Bach, T., Photochemical Deracemization of Chiral Alkenes via Triplet Energy Transfer. *J. Am. Chem. Soc.* **2022,** *144* (23), 10133-10138.

24. Li, X.; Grosskopf, J.; Jandl, C.; Bach, T., Enantioselective, Visible Light Mediated Aza Paterno-Buchi Reactions of Quinoxalinones. *Angew. Chem. Int. Ed. Engl.* **2021,** *60* (5), 2684-2688.

25. Plaza, M.; Grosskopf, J.; Breitenlechner, S.; Bannwarth, C.; Bach, T., Photochemical Deracemization of Primary Allene Amides by Triplet Energy Transfer: A Combined Synthetic and Theoretical Study. *J. Am. Chem. Soc.* **2021,** *143* (29), 11209-11217.

26. Grosskopf, J.; Plaza, M.; Seitz, A.; Breitenlechner, S.; Storch, G.; Bach, T., Photochemical Deracemization at sp^3-Hybridized Carbon Centers via a Reversible Hydrogen Atom Transfer. *J. Am. Chem. Soc.* **2021,** *143* (50), 21241-21245.

27. Kutta, R. J.; Grosskopf, J.; van Staalduinen, N.; Seitz, A.; Pracht, P.; Breitenlechner, S.; Bannwarth, C.; Nuernberger, P.; Bach, T., Multifaceted View on the Mechanism of a Photochemical Deracemization Reaction. *J. Am. Chem. Soc.* **2023,** *145* (4), 2354-2363.

28. Osawa, M.; Nagai, H.; Akita, M., Photo-activation of Pd-catalyzed Sonogashira Coupling using a Ru/bipyridine Complex as Energy Transfer Agent. *Dalton Trans.* **2007,** (8), 827-829.

29. Kalyani, D.; McMurtrey, K. B.; Neufeldt, S. R.; Sanford, M. S., Room-temperature C-H Arylation: Merger of Pd-catalyzed C-H Functionalization and Visible-light Photocatalysis. *J. Am. Chem. Soc.* **2011,** *133* (46), 18566-18569.

30. Ye, Y.; Sanford, M. S., Merging Visible-light Photocatalysis and Transition-Metal Catalysis in the Copper-catalyzed Trifluoromethylation of Boronic Acids with CF_3I. *J. Am. Chem. Soc.* **2012,** *134* (22), 9034-9037.

31. (a)Heitz, D. R.; Tellis, J. C.; Molander, G. A., Photochemical Nickel-Catalyzed C-H Arylation: Synthetic Scope and Mechanistic Investigations. *J. Am. Chem. Soc.* **2016,** *138* (39), 12715-12718; (b) Karakaya, I.; Primer, D. N.; Molander, G. A., Photoredox Cross-Coupling: Ir/Ni Dual Catalysis for the Synthesis of Benzylic Ethers. *Org. Lett.* **2015,** *17* (13), 3294-3297; (c) Karimi-Nami, R.; Tellis, J. C.; Molander, G. A., Single-Electron Transmetalation: Protecting-Group-Independent Synthesis of Secondary Benzylic Alcohol Derivatives via Photoredox/Nickel Dual Catalysis. *Org. Lett.* **2016,** *18* (11), 2572-2575.

32. (a) Kariofillis, S. K.; Doyle, A. G., Synthetic and Mechanistic Implications of Chlorine Photoelimination in Nickel/Photoredox C(sp^3)-H Cross-Coupling. *Acc. Chem. Res.* **2021,** *54* (4), 988-1000; (b) Shields, B. J.; Doyle, A. G., Direct C(sp^3)-H Cross Coupling Enabled by Catalytic Generation of Chlorine Radicals. *J. Am. Chem. Soc.* **2016,** *138* (39), 12719-12722.

33. (a) Beil, S. B.; Chen, T. Q.; Intermaggio, N. E.; MacMillan, D. W. C., Carboxylic Acids as Adaptive Functional Groups in Metallaphotoredox Catalysis. *Acc. Chem. Res.* **2022,** *55* (23), 3481-3494; (b) Zuo, Z.; Ahneman, D.; Chu, L.; Terrett, J.; Doyle, A. G.; MacMillan, D. W. C., Merging Photoredox with Nickel Catalysis: Coupling of α-carboxyl sp^3-carbons with Aryl Halides. *Science* **2014,** *345* (6195), 437-440.

34. Kariofillis, S. K.; Shields, B. J.; Tekle-Smith, M. A.; Zacuto, M. J.; Doyle, A. G., Nickel/Photoredox-Catalyzed Methylation of (Hetero)aryl Chlorides Using Trimethyl Orthoformate as a Methyl Radical Source. *J. Am. Chem. Soc.* **2020,** *142* (16), 7683-7689.

35. (a) Huang, J.; Chen, Z.; Wu, J., Recent Progress in Methyl-Radical-Mediated Methylation or Demethylation Reactions. *ACS Catal.* **2021,** *11* (17), 10713-10732; (b) Aynetdinova, D.; Callens, M. C.; Hicks, H. B.; Poh, C. Y. X.; Shennan, B. D. A.; Boyd, A. M.; Lim, Z. H.; Leitch, J. A.; Dixon, D. J., Installing the "Magic Methyl"- C-H Methylation in Synthesis. *Chem. Soc. Rev.* **2021,** *50* (9), 5517-5563; (c) Schonherr, H.; Cernak, T., Profound Methyl Effects in Drug Discovery and a Call for New C-H Methylation Reactions. *Angew. Chem. Int. Ed. Engl.* **2013,** *52* (47), 12256-12267.

36. (a) Dongbang, S.; Doyle, A. G., Ni/Photoredox-Catalyzed C(sp^3)-C(sp^3) Coupling between Aziridines and Acetals as Alcohol-Derived Alkyl Radical Precursors. *J. Am. Chem. Soc.* **2022,** *144* (43), 20067-20077; (b) Kariofillis, S. K.; Jiang, S.; Zuranski, A. M.; Gandhi, S. S.; Martinez Alvarado, J. I.; Doyle, A. G., Using Data Science To Guide Aryl Bromide Substrate Scope Analysis in a Ni/Photoredox-Catalyzed Cross-Coupling with Acetals as Alcohol-Derived Radical Sources. *J. Am. Chem. Soc.* **2022,** *144* (2), 1045-1055.

37. (a) Demarteau, J.; Debuigne, A.; Detrembleur, C., Organocobalt Complexes as Sources of Carbon-Centered Radicals for Organic and Polymer Chemistries. *Chem. Rev.* **2019,** *119* (12), 6906-6955; (b) Wdowik, T.; Gryko, D., C–C Bond Forming Reactions Enabled by Vitamin B12–Opportunities and Challenges. *ACS Catal.* **2022,** *12* (11), 6517-6531.

38. Potrzasaj, A.; Musiejuk, M.; Chaladaj, W.; Giedyk, M.; Gryko, D., Cobalt Catalyst Determines Regioselectivity in Ring Opening of Epoxides with Aryl Halides. *J. Am. Chem. Soc.* **2021,** *143* (25), 9368-9376.

39. Potrzasaj, A.; Ociepa, M.; Chaladaj, W.; Gryko, D., Bioinspired Cobalt-Catalysis Enables Generation of Nucleophilic Radicals from Oxetanes. *Org. Lett.* **2022,** *24* (13), 2469-2473.

40. (a) Sinha, N.; Wenger, O. S., Photoactive Metal-to-Ligand Charge Transfer Excited States in 3d^6 Complexes with Cr^0, Mn^I, Fe^{II}, and Co^{III}. *J. Am. Chem. Soc.* **2023,** *145* (9), 4903-4920; (b) Forster, C.; Heinze, K., Photophysics and photochemistry with Earth-abundant metals - fundamentals and concepts. *Chem. Soc. Rev.* **2020,** *49* (4), 1057-1070.

41. (a) Wenger, O. S., Photoactive Complexes with Earth-Abundant Metals. *J. Am. Chem. Soc.* **2018,** *140* (42), 13522-13533; (b) Arias-Rotondo, D. M.; McCusker, J. K., The Photophysics of Photoredox Catalysis: A Roadmap for Catalyst Design. *Chem. Soc. Rev.* **2016,** *45* (21), 5803-5820.

42. Larsen, C. B.; Wenger, O. S., Photoredox Catalysis with Metal Complexes Made from Earth-Abundant Elements. *Chem. Eur. J.* **2018,** *24* (9), 2039-2058.

43. (a) Kitzmann, W. R.; Moll, J.; Heinze, K., Spin-flip luminescence. *Photochem. Photobiol. Sci.* **2022,** *21* (7), 1309-1331; (b) Grübel, M.; Bosque, I.; Altmann, P. J.; Bach, T.; Hess, C. R., Redox and Photocatalytic Properties of a Ni^{II} Complex with a Macrocyclic Biquinazoline (Mabiq) Ligand. *Chem. Sci.* **2018,** *9* (13), 3313-3317; (c) Bürgin, T. H.; Glaser, F.; Wenger, O. S., Shedding Light on the Oxidizing Properties of Spin-Flip Excited States in a Cr(III) Polypyridine Complex and Their Use in Photoredox Catalysis. *J. Am. Chem. Soc.* **2022,** *144* (31), 14181-14194; (d) Glaser, F.; Wenger, O. S., Recent progress in the development of transition-metal based photoredox catalysts. *Coord. Chem. Rev.* **2020,** *405*; (e) Ogawa, T.; Sinha, N.; Pfund, B.; Prescimone, A.; Wenger, O. S., Molecular Design Principles to Elongate the Metal-to-Ligand Charge Transfer Excited-State Lifetimes of Square-Planar Nickel(II) Complexes. *J. Am. Chem. Soc.* **2022,** *144* (48), 21948-21960; (f) Sinha, N.; Pfund, B.; Wegeberg, C.; Prescimone, A.; Wenger, O. S., Cobalt(III) Carbene Complex with an Electronic Excited-State Structure Similar to Cyclometalated Iridium(III) Compounds. *J. Am. Chem. Soc.* **2022,** *144* (22), 9859-9873.

44. Tucker, J. W.; Narayanam, J. M. R.; Krabbe, S. W.; Stephenson, C. R. J., Electron Transfer Photoredox Catalysis: Intramolecular Radical Addition to Indoles and Pyrroles. *Org. Lett.* **2009,** *12* (2), 368-371.

45. Pitre, S. P.; McTiernan, C. D.; Ismaili, H.; Scaiano, J. C., Mechanistic insights and kinetic analysis for the oxidative hydroxylation of arylboronic acids by visible light photoredox catalysis: a metal-free alternative. *J. Am. Chem. Soc.* **2013,** *135* (36), 13286-13289.

46. Zou, Y. Q.; Chen, J. R.; Liu, X. P.; Lu, L. Q.; Davis, R. L.; Jorgensen, K. A.; Xiao, W. J., Highly efficient aerobic oxidative hydroxylation of arylboronic acids: photoredox catalysis using visible light. *Angew. Chem. Int. Ed.* **2012,** *51* (3), 784-788.

47. Jang, Y. J.; An, H.; Choi, S.; Hong, J.; Lee, S. H.; Ahn, K. H.; You, Y.; Kang, E. J., Green-Light-Driven Fe(III)(btz)(3) Photocatalysis in the Radical Cationic [4+2] Cycloaddition Reaction. *Org. Lett.* **2022,** *24* (24), 4479-4484.

48. (a) Lin, S.; Ischay, M. A.; Fry, C. G.; Yoon, T. P., Radical cation Diels-Alder cycloadditions by visible light photocatalysis. *J. Am. Chem. Soc.* **2011,** *133* (48), 19350-19353; (b) Farney, E. P.; Chapman, S. J.; Swords, W. B.; Torelli, M. D.; Hamers, R. J.; Yoon, T. P., Discovery and Elucidation of Counteranion Dependence in Photoredox Catalysis. *J. Am. Chem. Soc.* **2019,** *141* (15), 6385-6391.

49. Kochi, J. K., Photolyses of Metal Compounds: Cupric Chloride in Organic Media. *J. Am. Chem. Soc.* **1962,** *84* (11), 2121–2127.

50. Treacy, S. M.; Rovis, T., Copper Catalyzed C(sp^3)-H Bond Alkylation via Photoinduced Ligand-to-Metal Charge Transfer. *J. Am. Chem. Soc.* **2021,** *143* (7), 2729-2735.

51. (a) Chen, T. Q.; Pedersen, P. S.; Dow, N. W.; Fayad, R.; Hauke, C. E.; Rosko, M. C.; Danilov, E. O.; Blakemore, D. C.; Dechert-Schmitt, A. M.; Knauber, T.; Castellano, F. N.; MacMillan, D. W. C., A Unified Approach to Decarboxylative Halogenation of (Hetero)aryl Carboxylic Acids. *J. Am. Chem. Soc.* **2022,** *144* (18), 8296-8305; (b) Dow, N. W.; Pedersen, P. S.; Chen, T. Q.; Blakemore, D. C.; Dechert-Schmitt, A. M.; Knauber, T.; MacMillan, D. W. C., Decarboxylative Borylation and Cross-Coupling of (Hetero)aryl Acids Enabled by Copper Charge Transfer Catalysis. *J. Am. Chem. Soc.* **2022,** *144* (14), 6163-6172.

52. de Groot, L. H. M.; Ilic, A.; Schwarz, J.; Warnmark, K., Iron Photoredox Catalysis-Past, Present, and Future. *J. Am. Chem. Soc.* **2023,** *145* (17), 9369-9388.

53. (a) Xiong, N.; Li, Y.; Zeng, R., Iron-Catalyzed Photoinduced Remote C(sp^3)-H Amination of Free Alcohols. *Org. Lett.* **2021,** *23* (22), 8968-8972; (b) Xue, T.; Zhang, Z.; Zeng, R., Photoinduced Ligand-to-Metal Charge Transfer (LMCT) of Fe Alkoxide Enabled C-C Bond Cleavage and Amination of Unstrained Cyclic Alcohols. *Org. Lett.* **2022,** *24* (3), 977-982; (c) Zhang, Z.; Zhang, G.; Xiong, N.; Xue, T.; Zhang, J.; Bai, L.; Guo, Q.; Zeng, R., Oxidative alpha-C-C Bond Cleavage of 2 degrees and 3 degrees Alcohols to Aromatic Acids with O$_2$ at Room Temperature via Iron Photocatalysis. *Org. Lett.* **2021,** *23* (8), 2915-2920; (d) Feng, G.; Wang, X.; Jin, J., Decarboxylative C-C and C-N Bond Formation by Ligand-Accelerated Iron Photocatalysis. *Eur. J. Org. Chem.* **2019,** *2019* (39), 6728-6732; (e) Li, Z.; Wang, X.; Xia, S.; Jin, J., Ligand-Accelerated Iron Photocatalysis Enabling Decarboxylative Alkylation of Heteroarenes. *Org. Lett.* **2019,** *21* (11), 4259-4265; (f) Xia, S.; Hu, K.; Lei, C.; Jin, J., Intramolecular Aromatic C-H Acyloxylation Enabled by Iron Photocatalysis. *Org. Lett.* **2020,** *22* (4), 1385-1389.

54. (a) Ociepa, M.;   Wierzba, A. J.;   Turkowska, J.; Gryko, D., Polarity-Reversal Strategy for the Functionalization of Electrophilic Strained Molecules via Light-Driven Cobalt Catalysis. *J. Am. Chem. Soc.* **2020,** *142* (11), 5355-5361; (b) Ociepa, M.;   Baka, O.;   Narodowiec, J.; Gryko, D., Light-driven vitamin B$_{12}$-catalyzed generation of acyl radicals from 2-S-pyridyl thioesters. *Adv. Synth. Catal.* **2017,** *359* (20), 3560-3565; (c) Bam, R.;   Pollatos, A. S.;   Moser, A. J.; West, J. G., Mild Olefin Formation via Bio-inspired Vitamin B$_{12}$ Photocatalysis. *Chem. Sci.* **2020,** *12* (5), 1736-1744.

55. (a) Sun, H.-L.; Yang, F.; Ye, W.-T.; Wang, J.-J.; Zhu, R., Dual Cobalt and Photoredox Catalysis Enabled Intermolecular Oxidative Hydrofunctionalization. *ACS Catal.* **2020,** *10* (9), 4983-4989; (b) Zhou, X. L.; Yang, F.; Sun, H. L.; Yin, Y. N.; Ye, W. T.; Zhu, R., Cobalt-Catalyzed Intermolecular Hydrofunctionalization of Alkenes: Evidence for a Bimetallic Pathway. *J. Am. Chem. Soc.* **2019,** *141* (18), 7250-7255; (c) Meng, Q. Y.;   Schirmer, T. E.;   Katou, K.; König, B., Controllable Isomerization of Alkenes by Dual Visible-Light-Cobalt Catalysis. *Angew. Chem. Int. Ed.* **2019,** *58* (17), 5723-5728.

56. (a) Donal J. Coveney;   Vinod F. Patel;   Pattenden, G.; Thompson, D. M., Acylcobalt Salophen Reagents. Precursors to Acyl Radical Intermediates for Use in Carbon-to-Carbon Bond-forming Reactions to Alkenes. *J. Chem. Soc. Perkin Trans.* **1990,** *1*, 2721-2728; (b) Pattenden, G., Cobalt-mediated Radical Reactions in Organic Synthesis. *Chem. Soc. Rev.* **1988,** *17*, 361-382; (c) Patel, V. F.; Pattenden, G.; Thompson, D. M., Cobalt-mediated Reactions in Synthesis. The Degradation of Carboxylic Acids to Functionalised Noralkanes via Acylcobalt Salophen Intermediates. *J. Chem. Soc. Perkin Trans.* **1990,** *1*, 2729-2734.

57. (a) Banerjee, P.;   Company, A.;   Weyhermüller, T.;   Bill, E.; Hess, C. R., Zn and Fe Complexes Containing a Redox Active Macrocyclic Biquinazoline Ligand. *Inorg. Chem.* **2009,** *48*, 2944-2955; (b) Puttock, E. V.; Banerjee, P.; Kaspar, M.; Drennen, L.; Yufit, D. S.; Bill, E.; Sproules, S.; Hess, C. R., A series of [Co(Mabiq)Cl$_{2-n}$] (n = 0, 1, 2) compounds and evidence for the elusive bimetallic form. *Inorg. Chem.* **2015,** *54* (12), 5864-5873; (c) Stark, H. S.;   Altmann, P. J.;   Sproules, S.; Hess, C. R., Structural characterization and photochemical properties of mono- and bimetallic Cu-mabiq complexes. *Inorg. Chem.* **2018,** *57* (11), 6401-6409.

Chapter 2

Co–Mabiq Flies Solo: Light-Driven Markovnikov-Selective C- and N-Alkylation of Indoles and Indazoles without a Cocatalyst

Authors: Oaikhena Zekeri Esezobor, Wenyi Zeng, Lukas Niederegger, Michael Grübel, and Corinna R. Hess

Summary: This work describes the synthesis and characterization of a Co-complex based on the Br-modified macrocyclic biquinazoline (Mabiq) ligand, and its utilization in the photoinduced regioselective alkylation of indoles and indazoles with electron rich styrenes.

Following a mechanism based approach, we explored the excited state interaction of Co(Mabiq)Cl$_2$ **1** with organic molecules such as allyl bromide. We had initially found that **1** is photoactive as it undergoes a visible light induced homolysis of the Co–Cl bond when a MeCN solution of the compound is irradiated. When a MeCN solution of **1** and allyl bromide was irradiated and monitored by UV-Vis, the final spectrum obtained was different from the spectrum observed during the photolysis studies on **1**. In the presence of 4-methoxystyrene, the interaction between **1** and allyl bromide led to the head-to-tail dimerization of the styrene. Furthermore, C3-alkylated indole was formed when a solution of **1**, allyl bromide, 4-methoxystyrene and indole was irradiated.
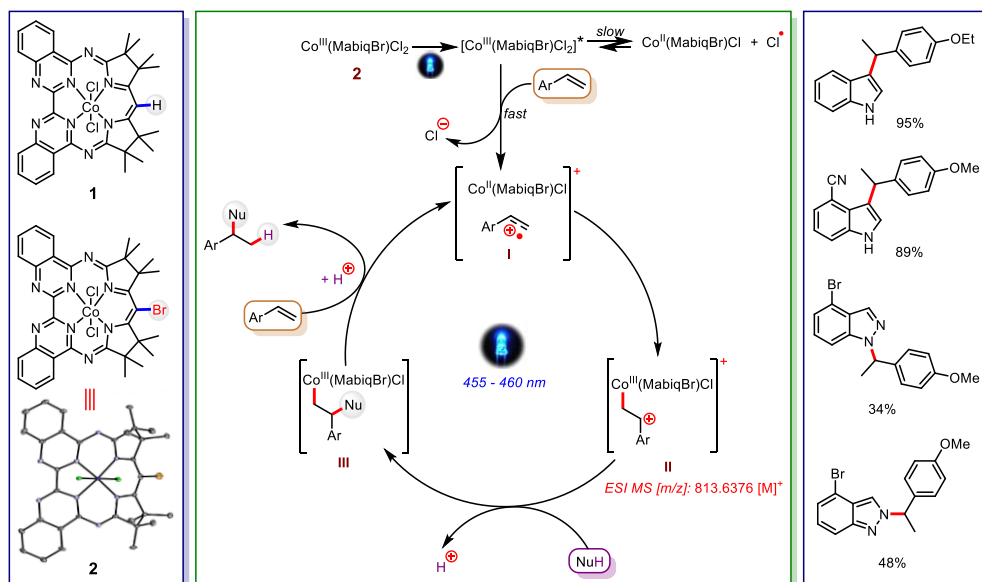
On further probing the contents of the irradiated solution of **1** and allyl bromide by ESI MS, we observed the transfer of Br from allyl bromide to the Mabiq ligand. We then successfully synthesized the Br-modified Mabiq ligand and complexation with CoCl$_2$ afforded Co(MabiqBr)Cl$_2$ **2**. Compound **2** effectively catalyzed the dimerization of 4-methoxystyrene and C3-alkylated indole in the absence of allyl bromide, thus confirming that this compound

is the active species detected in the irradiated solution of **1** and allyl bromide. With these results, the project then focused on C3-alkylation of indoles and N-alkylation of indazoles with electron-rich styrenes. Mechanistic investigations revealed that upon excitation, an SET ensues between **2** and styrene to generate metalloradical Co^{II}(Mabiq) and styryl radical cation. A radical rebound of the styryl radical onto the Co^{II}(Mabiq) then occurs. This step is critical to controlling the regiochemistry of the final product. Nucleophilic addition of indole or indazole to the coordinated styryl cation furnishes the alkylated indole product in a Markovnikov-selectivity fashion.

The generation of styryl radical cation and regioselectively coupling to indoles and indazoles demonstrated the ability of **2** to adopt a dual role in this reaction, acting as both the photocatalyst and metal center for regioselective bond formation. Although only electron-rich styrenes reacted favourably, a wide range of functional groups on the indole and indazole partners were tolerated. Indoles also reacted freely without the requirement for N-protection or directing group affording products with yields as high as 96%. Due to comparable N-nucleophilicity, mixtures of N1 and N2-alkylated indazoles were obtained with combined yields of up to 95% and selectivity slightly favouring N2 over N1. Compared to literature reports, this methodology did not require protection of the C3-position of the indazoles. The dual role adopted by **2** thus obviated the requirement for external oxidant/reductant, cocatalyst and added photosensitizer.

Contributions of Authors

Oaikhena Z. Esezobor planned, developed, and executed all the experiments, and wrote the manuscript. W. Zeng isolated some of the compounds, analysed NMR data and proofread the manuscript. L. Niederegger performed XRD measurements and proofread the manuscript. M. Grübel synthesized and obtained the molecular structure of the Br-modified Mabiq ligand. The development of the project and preparation of the manuscript was carried out under the supervision of Corinna R. Hess.

Article

Co−Mabiq Flies Solo: Light-Driven Markovnikov-Selective C- and N-Alkylation of Indoles and Indazoles without a Cocatalyst

Oaikhena Zekeri Esezobor, Wenyi Zeng, Lukas Niederegger, Michael Grübel, and Corinna R. Hess*

Read Online

ACCESS | Metrics & More | Article Recommendations | SI Supporting Information

ABSTRACT: Indoles and indazoles are common moieties in pharmaceuticals and naturally occurring bioactive compounds. The development of light-driven methods using earth-abundant transition-metal catalysts offers an attractive route for functionalization of such compounds. Herein, we report a visible-light-induced method for the C3- and N-alkylation of indoles and indazoles with styrenes, catalyzed by Co complexes based on the macrocyclic Mabiq ligand (Mabiq = 2−4:6−8-bis(3,3,4,4-tetramethyldihydropyrrolo)-10−15-(2,2′-biquinazolino)-[15]-1,3,5,8,10,14-hexaene-1,3,7,9,11,14-N_6). The photochemical behavior of two Co^{III} catalysts was examined: Co(Mabiq)-Cl_2 and the newly synthesized Co(MabiqBr)Cl_2, which contains the Br-modified ligand. Both complexes undergo visible-light-induced homolysis that is significant to their activity but exhibit differences in reactivity. The alkylation reactions are regioselective, furnishing the alkylated indole and indazole products in a Markovnikov fashion with excellent yields of up to 96% across a broad range of substrates. Notably, in contrast to dual-transition-metal and photoredox-catalyzed cross-coupling reactions, our studies reveal that the Co complex plays a dual role—as a photosensitizer and catalytically active metal center with the Mabiq ligand offering regiocontrol.

R—⟨benzene⟩=CH2 + Nu−H → (Co, 455 - 460 nm) → R—⟨benzene⟩(Nu)−CH3(H)

up to 96% yield
Markovnikov selectivity
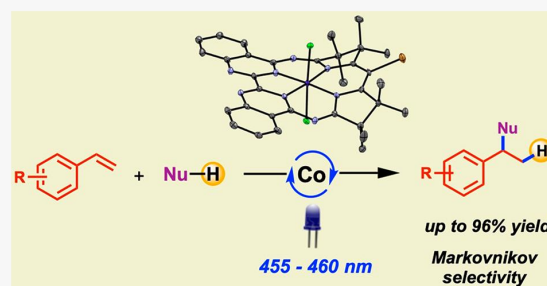
■ INTRODUCTION

The recent concentration of efforts to develop earth-abundant metal complexes for photoredox catalysis[1−5] is driven by both sustainability concerns and the prospects for engendering entirely new light-driven chemistry. Photoredox catalysis has largely been dominated by expensive Ru- and Ir-based complexes. However, these coordinatively saturated 4d and 5d compounds can engage solely in outer-sphere electron transfer processes. Hence, their combination with other transition metals—a strategy known as metallaphotoredox catalysis—has become a valuable tool for forming new C−C and C−X bonds, which were hitherto difficult to generate with single-photocatalyst systems.[6−8] The development of transition-metal catalysts capable of serving dual roles, i.e., as photosensitizers and catalytic centers, would be beneficial, wherefore many earth-abundant complexes have attracted extensive interest. First-row transition-metal complexes, for example, frequently have unsaturated coordination spheres and more readily undergo ligand exchange compared to their heavier congeners. These attributes can be exploited in excited state reactions and offer greater reactivity control via the inner coordination sphere.

Several 3d complexes, including cobalt compounds, can undergo visible-light-induced homolysis (VLIH).[1,5,9−13] Indeed, such photochemical behavior of cobalt-salens, alkyl-cobalamins, cobaloximes, and related macrocyclic cobalt compounds is well-established: photoinduced homolysis of

the Co^{III}−alkyl leads to the formation of radical pairs, i.e., Co^{II} species and alkyl radicals.[14−21] Co−alkyl complexes have consequently been investigated in several photocatalytic processes, in which the ensuing C-centered radical intermediates undergo dimerization, cyclization, dehalogenation, and ring-opening/expansion reactions.[14−16,22,23] Although the cobalt complexes serve as photocatalysts and substrate activation sites, all these processes nevertheless require an additional transition-metal cocatalyst and reductant.

Our group is interested in exploiting the photocatalytic potential of first-row transition-metal complexes based on the Mabiq ligand (Mabiq = 2−4:6−8-bis(3,3,4,4-tetramethyl-dihydropyrrolo)-10−15-(2,2′-biquinazolino)-[15]-1,3,5,8,10,14-hexaene-1,3,7,9,11,14-N_6; Figure 1). We previously established the ability of the Ni−Mabiq complex to act as a photoredox catalyst in several C−C bond forming reactions.[24,25] Both the cationic and neutral [Ni(Mabiq)]^n (n = 0, 1+) complexes involved in these reactions contain Ni(II) ions that favor a four-coordinate square planar geometry. In
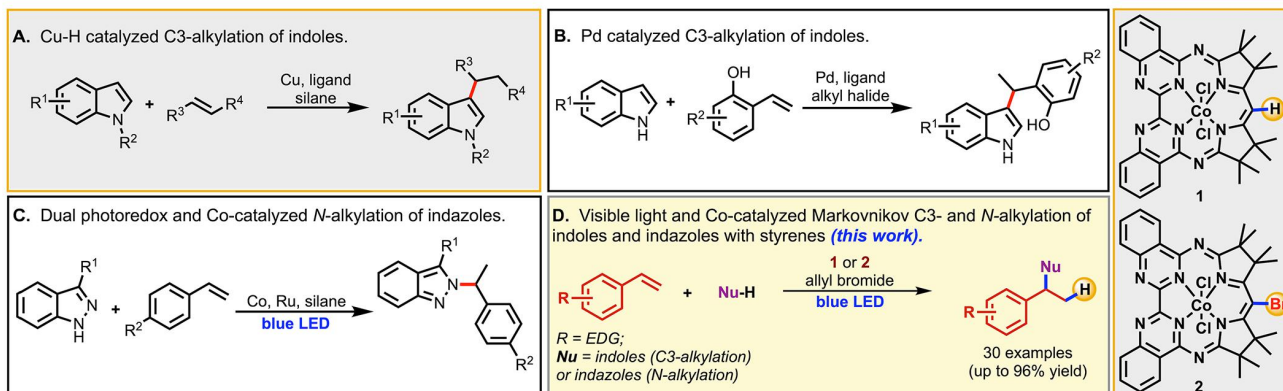
Figure 1. Previous reports of C3-alkylation of indoles (A,B),[41−43] N-alkylation of indazoles (C)[44] with styrenes, and reactions in this work (D). EDG: electron-donating group.

contrast, the series of Co−Mabiq compounds support a richer redox and coordination chemistry—anionic through dicationic $[Co(Mabiq)]^n$ ($n = 1- \rightarrow 2+$) with four-, five-, and six-coordinate geometries available—and thus, we envisioned these compounds would offer richer photochemistry.[26,27] We have now explored the photochemical behavior of the Co[III]−Mabiq complex, Co(Mabiq)Cl₂ (**1**, Figure 1). As part of these studies, we have also generated and characterized a brominated ligand variant, MabiqBr, and the Co compound thereof (Co(MabiqBr)Cl₂, **2**, Figure 1). We show that both Co[III]−Mabiq complexes undergo VLIH.

Notably, **1** and **2** act as catalysts for the visible-light-induced C- and N-alkylation of indoles and indazoles with styrenes (Figure 1D). Indoles and indazoles are among the biologically relevant N-heterocycles in natural and pharmaceutical compounds.[28−32] Consequently, the development of strategies for their functionalization is of interest to synthetic organic chemists. Despite the large number of synthetic methodologies available in the literature for the functionalization of indoles[33−38] and indazoles,[39] the use of styrenes as direct alkylating agents remains uncommon and requires a specific substrate and/or catalyst control.[40] These protocols usually need stoichiometric amounts of hydride donors (Figure 1A,B[41−43]), while a reported light-driven process for N-alkylation of indazoles also relied on a separate photosensitizer (Ru) and organometallic cocatalyst (Figure 1C).[44] In contrast, *in the cobalt−Mabiq(Br)-catalyzed reactions described herein, the Co center adopts both roles.* The C3-alkylation of indoles represents the first light-induced method for this functionalization process. Initial mechanistic studies indicate that, upon irradiation, the Co catalyst oxidizes the styrene substrate, and the ensuing radical cation is trapped in a regioselective fashion controlled by the coordination environment. Subsequent addition of the nucleophile results in C−C or C−N cross-coupled products.

RESULTS AND DISCUSSION

Reaction Development. Given the related structure of Mabiq to the aforementioned macrocyclic Co complexes, particularly cobalamins, and the established ability to photo-reduce the series of M[II]−Mabiq complexes (M = Fe[II] → Zn[II]),[24,25,45] we reasoned that the trivalent Co−Mabiq complex, Co(Mabiq)Cl₂ (**1**), might also be photoactive and undergo VLIH. Indeed, irradiation of **1** even in the absence of a sacrificial electron donor leads to photolysis of the Co−Cl

bond, with formation of the Co[II]-containing analogue as the sole product based on the final absorption spectrum (Figures 2A and S3).[26] In the absence of other substrates (*vide infra*) the conversion of Co[III] is very slow (ca. 6 h to completion, $\varphi = 9.5 \times 10^{-6}$) and displays complex kinetics, which may be due to the recombination of Co[II] and accumulated Cl• over time (see SI for details and Figure S4). The resultant Co[II] complex is photostable: no evidence of degradation is observed in the absorption spectrum, and the ESI mass spectrometry data shows only a mass consistent with the intact cobalt compound (Figure S5). Given the propensity of **1** for VLIH, we applied a mechanism-based approach[46,47] to investigate catalyst−substrate interactions upon irradiation of **1** and to explore its catalytic capacity for light-driven C−C bond formation. The simple haloalkene, allyl bromide, was initially tested as a substrate for photoinduced allylation.[48] The absorption spectral changes upon irradiation of a solution of **1** and allyl bromide signified rapid depletion of **1** (within ca. 35 min under the same conditions as for the photolysis) and clean evolution to new species (Figures 2B and S6). The product spectrum is different from that of Co[II](Mabiq)Cl but with similar absorption features in the region of 400−450 nm and above 550 nm (Figure S3). The additional band at $\lambda_{max} = 524$ nm is red-shifted by 11 nm compared to the dominant transition of **1** at 513 nm. These absorbance features suggest that the final product may contain a mixture of Co[II] and Co[III] species. ESI mass spectrometry (ESI-MS) analysis of the irradiated solution shows a peak of *m/z* 678.7432 with a characteristic bromine isotope pattern (Figures S7 and S8). The mass value fits to a Br-containing complex in which the ligand has been modified—i.e., *m/z* value corresponding to [Co-(MabiqBr)]⁺—rather than a complex containing a cobalt-bromide bond (see the SI for further details, Figures S7 and S8). A peak with *m/z* 642.0067 consistent with an allyl-bound Co−Mabiq complex is additionally observed.

We reasoned that if Br and/or allyl radicals were generated by the interaction of **1** and allyl bromide, regioselective allylation of styrenes influenced by the inner coordination sphere of the Co center could be achieved. Hence, to investigate the catalytic potential of the *in-situ*-generated photoproduct in the **1**/allyl bromide reaction, various styrenes (0.2 mmol) were added to MeCN solutions of **1** (2 mol %) and allyl bromide (0.5 equiv), and the mixture was irradiated for 24 h (3 W blue LED, 455−460 nm; Table S1). Surprisingly, with 4-methoxystyrene (**3a**), we observed the
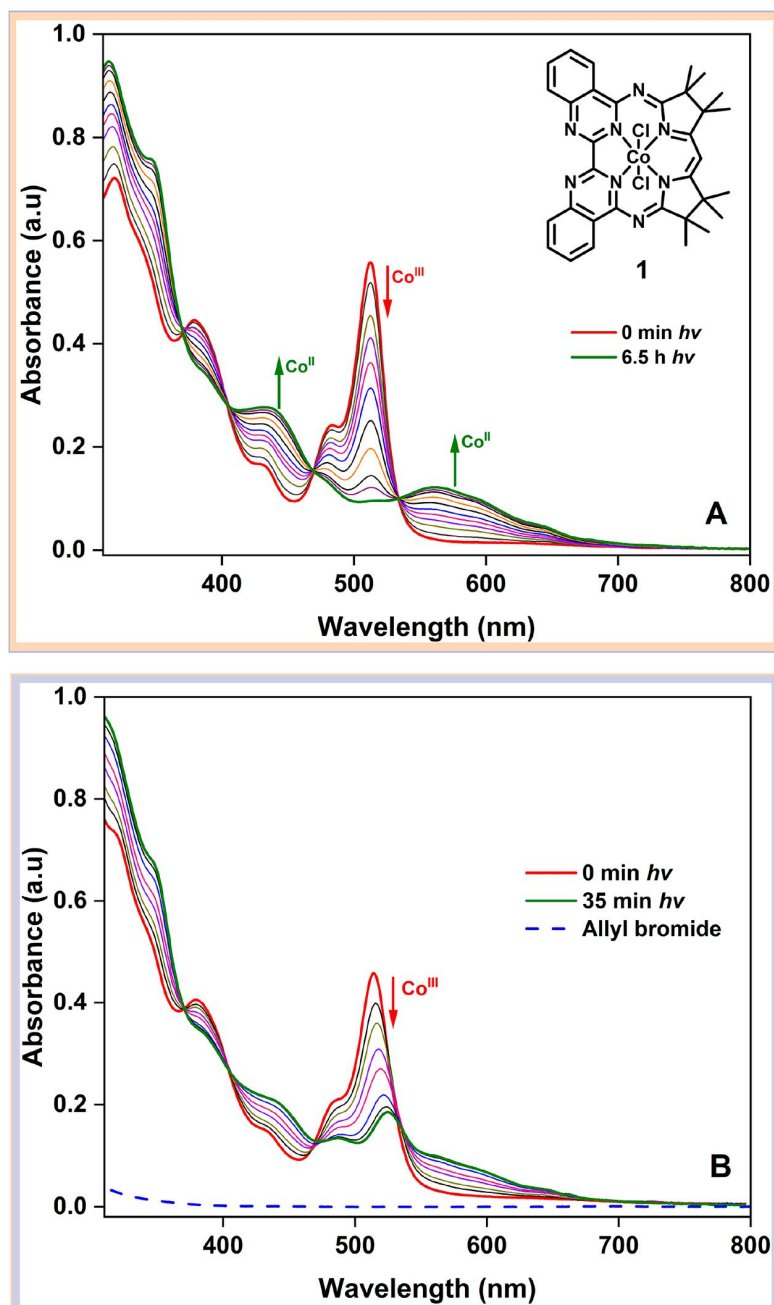
Figure 2. (A) Spectral evolution during the photolysis of **1**. Red trace: spectrum of **1** (0.035 mM in MeCN) prior to irradiation. Green trace: final spectrum obtained after irradiation of the solution with a blue LED (455 nm, P_{ref} = 540 mW, φ = 9.5 × 10^{-6}). (B) Dashed blue trace: spectrum of allyl bromide. Red trace: spectrum of **1** (0.03 mM) and allyl bromide (0.3 mM, 10 equiv) in MeCN prior to irradiation. Green trace: final spectrum obtained after irradiation of the solution with a blue LED (455 nm, P_{ref} = 540 mW).

head-to-tail dimer **4a** in 23% yield (Table S1, entry 4), rather than any cross-coupling products between allyl bromide and **3a**. No cross-coupling products were observed with the other styrenes tested (Table S1, entries 1−3). Control experiments (Table S2) revealed that **1**, allyl bromide, LED illumination, and inert atmosphere conditions are all necessary for the formation of **4a**. The product yield could be increased to 62% using a higher amount of allyl bromide (1.5 equiv; Scheme 1 and Table S3). Thus, although no allyl-functionalized products were obtained, the alkenyl halide plays an essential role in the dimerization reaction catalyzed by **1**.

While screening for a suitable solvent for the styrene dimerization reaction, we noticed that in methanol, **4a** was formed in very low yield (7%, Table S4, entry 4). Instead, a significant amount of 1-methoxy-4-(1-methoxyethyl)-benzene was produced (66% ^{1}H NMR yield, Table S4). With this observation, we wondered if more nucleophilic substrates, such as indoles, would react efficiently with styrenes to afford alkylated indole products. Indeed, 88% NMR yield of the C3-alkylated indole **6aa** was obtained upon irradiation of a reaction mixture containing **1** (2 mol %), 0.2 mmol each of **3a** and indole (**5a**), and allyl bromide (Scheme 1). At least 1.5

Scheme 1. Initial Optimized Reactions Catalyzed by 1
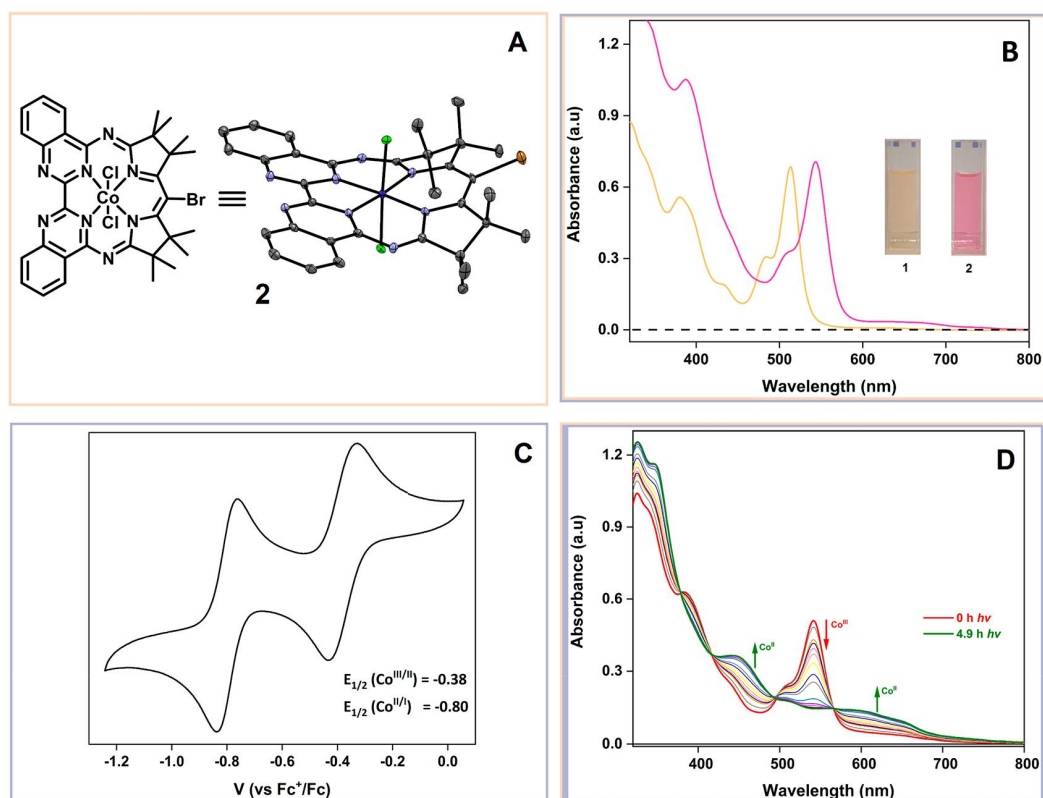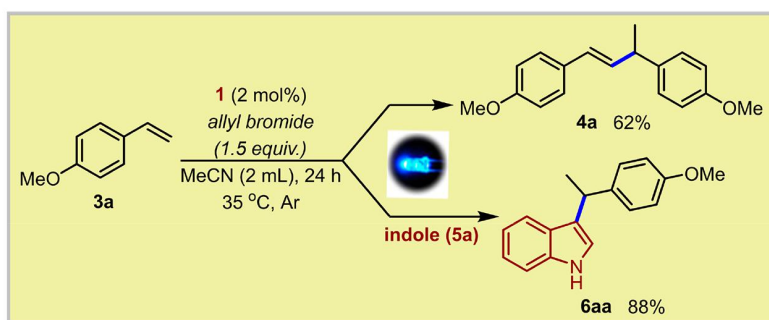
Figure 3. (A) Molecular structure of **2**, 50% ellipsoids, H atoms removed for clarity. (B) Comparison of absorption spectra of **1** and **2** in MeCN. (C) Cyclic voltammogram of **2** (1 mM in MeCN; 0.1 V s^{-1}, 100 mM [N(n-Bu)$_4$]PF$_6$), WE/CE (glassy carbon), RE (Ag/AgNO$_3$, 10 mM) under Ar atmosphere. The *formal* "Co$^{II/I}$" couple referred to in C corresponds to the ligand-centered reduction, MabiqBr/MabiqBr$^{\bullet}$. (D) Spectral evolution during the photolysis of **2**. Red trace: spectrum of **2** (0.034 mM in MeCN) prior to irradiation. Green trace: final spectrum obtained after irradiation of the solution with a blue LED (455 nm, P_{ref} = 540 mW; φ = 2.7 × 10^{-5}).

equiv of allyl bromide was again required to obtain high product yields (Table S5). The Co complex thus also offered a promising mild light-driven route for the functionalization of pharmaceutically relevant indoles.

The ability of **1** to photocatalyze the above reactions already supported our hypothesis that the complex can serve a dual role as a photosensitizer and catalytic Co center for regioselective-controlled catalysis. The light dependence of the product formation signifies an excited state electron transfer process. The regioselectivity of the head-to-tail dimerization reaction, retention of the double-bond, and lack of polymerization products in this reaction (Figures S9 and S10) also evidence that the Co center of **1** acts as the catalytic active site.[49−55]

Co(MabiqBr)Cl$_2$ as the Active Catalyst. Intrigued by these preliminary results, we sought to first understand the nature of the catalytically active species generated in the photodriven reaction of **1** with allyl bromide. As noted earlier, the ESI-MS analysis of the reaction product suggested formation of a modified Co−Mabiq species, [Co(MabiqBr)]$^+$. We deduced that the diketiminate moiety of the Mabiq ligand was a possible site of Br addition—the photoaccessible one-electron reduced [M(Mabiq$^{\bullet}$)] complexes and M^{II*} states have significant electron density distributed over the diketiminate site.[25,26] The bromine-functionalized Mabiq ligand was successfully synthesized, and substitution of the diketiminate C−H proton by a Br atom was confirmed by X-ray crystallography (Figure S11), ESI-MS (m/z 621.3230 [M +

32

Table 1. Optimization of Reaction Conditions for the C3-Alkylation of Indoles[a]

entry	deviation from the standard conditions	yield (%)[a]
1	none	89 (85[b])
2	**2** (2 mol %), allyl bromide (0.5 equiv), 24 h	90
3	**2** (1 mol %), without allyl bromide, 12 h	24
4	**2** (1 mol %), without allyl bromide, 24 h	40
5	**2** (2 mol %), without allyl bromide, 24 h	59
6	**2** (2 mol %), without allyl bromide, 48 h	83
7	without **2**	0
8	no LED	0
9	air	0

[a]Reaction conditions (unless otherwise specified): **3a** (0.2 mmol), **5a** (0.2 mmol), MeCN (2 mL, dry, deoxygenated), blue LED (3 W, 455−460 nm). Yields were determined by ^{1}H NMR using mesitylene as an internal standard. Yields are the average from at least two experiments. [b]Isolated yield.

H]$^+$; Figures S12 and S13), and ^{1}H NMR (Figure S14). Subsequent treatment of MabiqBr with CoCl$_2$ in aerated DCM, followed by recrystallization of the complex (DCM/hexane), provided Co(MabiqBr)Cl$_2$ (**2**, 82% yield) as reddish-brown needles suitable for X-ray diffraction. The molecular structure of **2** (Figures 3A and S15) reveals substantial buckling predominantly at the diketiminate unit of the ligand—an effect seemingly induced by the Br atom. A larger coplanarity difference of 38.57° between the quinazoline and diketiminate groups results, compared to the 20.65° observed in **1**. However, the average Co−N (1.904 Å), Co−Cl (2.258 Å), and ligand bond lengths (Table S8) in **2** are comparable to the analogous bond distances in **1**.[26] The ESI-MS data for **2** confirms that this compound is the product obtained in the light-driven reaction of **1**/allyl bromide (Figure S16).

The redox, spectroscopic, and photochemical properties of **2** were examined, as these properties correlate with its reactivity. The Br-containing **2** features a lower π−π* energy gap than **1**, with these transitions at λ_{max} = 544 nm (ε = 1.5 × 10^4 MeCN; Figure 3B) comparatively red-shifted (**1**, λ_{max} = 512 nm). A broad, weakly intense band at λ_{max} = 650 nm (ε = 3.5 × 10^2, MeCN) observed in the spectrum of **2** is tentatively assigned to d−d transitions. Both the Co$^{III/II}$ and formal Co$^{II/I}$ redox potentials of the brominated complex ($E_{1/2}$ = −0.38 and −0.80 V vs Fc$^{+/0}$, respectively, Figures 3C and S19) are similar to those of **1** ($E_{1/2}$ = −0.40 and −0.88 V vs Fc$^{+/0}$, respectively, Figure S20). The electron-withdrawing bromine atom appears to have a negligible effect on the reductions, suggesting also that the latter event involves a ligand-centered reduction. **2** also undergoes photolysis with a slightly higher quantum yield value for Co−Cl bond homolysis (φ = 2.7 × 10^{-5}, Figure 3D) compared to **1** (φ = 9.5 × 10^{-6}), and the conversion is straightforward (Figure S21). The spectral evolution accompanying photolysis of **2** likewise depicts formation of the one-electron reduced Co^{II}-containing complex, assigned as Co(MabiqBr)Cl based on the similarity of the final absorption spectrum in this process to that of Co(Mabiq)Cl and chemically generated Co(MabiqBr)Cl (Figures S22 and S27). The final Co^{II} product is also photostable (Figure S23).

The photolysis of **2** is again significantly faster (φ = 2.9 × 10^{-4}) in the presence of allyl bromide (Figures S24 and S25).

But in contrast to the behavior of **1**, the MS data indicates clean conversion to the Co^{II} form, without any evident degradation or modification of the complex (Figure S26). The reason for the faster Co^{III} → Co^{II} conversion in the presence of allyl bromide is currently not clear.

With **2** in hand, we focused on its photocatalytic activity in the C−C forming reactions initially observed with **1**. Compound **2** gave substantially higher yields in the light-driven head-to-tail dimerization of **3a** (80% **4a**, Table S10, entry 1), even using lower equivalents of allyl bromide (0.5 equiv). In fact, **4a** was also obtained in control experiments excluding allyl bromide (Table S10, entry 3), albeit with very low yields (12%). ESI-MS analysis of the latter reaction mixture revealed the presence of the debrominated Co complex (m/z 600.3831 = [CoMabiq]$^+$; Figure S29), which is only observed under these specific reaction conditions and not in the photolysis of **2** (Figure S23) or in the reaction with only allyl bromide (Figure S26). The debrominated Co species also is not observed in the MS data for the crude reaction mixtures with all components included (i.e., **3a**, **2**, and allyl bromide; Figure S31). Thus, the Mabiq diketiminate α-C appears to be susceptible to photoinduced functionalization under certain conditions. Overall, allyl bromide seems to play several roles. In photocatalytic styrene dimerization by **1**, allyl bromide serves as the Br source to generate the catalytically active **2**. In the reactions photocatalyzed by **2**, any potential, minor side-reactions leading to debromination of the Mabiq ligand can be suppressed with small amounts of added allyl bromide. The molecule may further facilitate Co^{III} → Co^{II} conversion.

Complex **2** also proved to be a more highly effective photocatalyst for C-3 functionalization of indoles, with 90% ^{1}H NMR yields of **6aa** obtained (Table 1, entry 2) in the reaction of 4-methoxystyrene (**3a**, 0.2 mmol) and indole (**5a**, 0.2 mmol). The amount of allyl bromide could even be reduced to 0.2 equiv (Table 1, entry 1) without compromising product yields. Other brominated compounds, including CBr$_4$, could be used instead of allyl bromide in the reaction (Table S13), but these alternate Br sources were not as effective (30−65% product yields, 12 h). When excluding allyl bromide entirely from the reaction, 24−83% yield of **6aa** was produced; the

higher yields corresponded to a longer irradiation time and higher catalyst loading (Table 1, entries 3−6). The behavior is in stark contrast to the reaction using **1** in the absence of allyl bromide, for which formation of **6aa** was not observed (Table S14). The dimerization product **4a** was not observed in any C-3 indole alkylation reactions. The moderate-to-excellent yields of **6aa** obtained with **2** indicate that the nucleophilicity of the coupling partner is crucial to obtaining high yields, irrespective of potential generation of the debrominated Co species when allyl bromide is excluded. We note that the Co−Mabiq-photocatalyzed route to the styrene-substituted indoles represents an improvement over literature reports, which usually require an excess of one of the coupling partners, hydrogen-atom donors, and substrate/catalyst control for regioselectivity.[41−43] This method is also the first light-driven single-catalyst route to indole functionalization with styrenes, and further studies with **2** focused on this reaction.

Mechanistic Investigations. We next turned our attention to the mechanistic pathways for the C3-indole alkylation. The formation of **6aa** in moderate-to-very good yields (59%, 24 h and 83%, 48 h, Table 1, entries 5 and 6) even in the absence of any additive is significant. Catalytic pathways proposed for most alkene functionalization methodologies involve metal hydride intermediates, usually generated with reagents such as silanes,[56−61] which are not involved here. Under photocatalytic conditions, the oxidation of olefins by organic photocatalysts and their subsequent coupling to nucleophiles to give anti-Markovnikov products have been reported.[62−65] The Markovnikov products obtained in this report imply that the Co complex thus adopts a dual role—as a photosensitizer and the catalytically active metal center.

To gain mechanistic insights into the processes occurring at the Co center, we spectroscopically monitored the individual interactions between **2** and each of the two substrates, methoxystyrene and indole, under irradiation. As with allyl bromide, irradiation of a solution of **2** and **3a** led to more rapid reduction of the Co^III complex (Figures S32 and S33). The Co^III consumption shows a clear dependence on styrene concentration, suggesting direct reduction of the cobalt complex by this substrate (Figure S34). The potential for oxidation of methoxystyrene is $E_{p,a} = 1.06$ V vs Fc^{+/0} (Figure S35), which should be sufficient to reduce Co^III* (Co^{III*/II} estimated at >1.27 V vs Fc^{+/0} considering the longest wavelength in the spectrum of **2**). We note that C3-indole functionalization by **2** is inhibited by added TBACl, whereas the dark reaction of **3a** and indole with HCl gives low product yields and substantial amounts of unidentified side-product (Table S12; Figure S28). Therefore, the low amount of chloride anion that would be released from the Co^II form generated upon reaction of **2*** with **3a** is inconsequential for the reaction. ESI-MS analysis of the **2**/**3a** product solution reveals the presence of new Co−styryl intermediates (m/z 735.7937 and 813.6376 [M]^+, Figure S29). Based on the Markovnikov regiochemistry of the C3-alkylated indole product **6aa**, we suggest that the styrene radical coordinates to the Co center via the terminal styryl C atom. Coordination of the Co ion to the benzylic position may be sterically disfavored, despite a thermodynamic preference for benzylic radical cation formation. Such catalyst-controlled regioselectivity has been proposed in related vitamin-B$_{12}$-catalyzed reactions.[18] In contrast to styrene, the indole **5a** has no effect on the photochemical behavior of **2**; the product and time

scale of Co^III conversion are the same in the presence and absence of indole (Figures S36 and S37).

Several studies were carried out to further probe the C3-alkylation reaction pathway. A radical trapping experiment with 2,2,6,6-tetramethylpiperidinyloxyl (TEMPO) as a radical trap, and **3a** and **5a** as substrates, was carried out under the standard reaction conditions with allyl bromide present (Scheme 2a).

Scheme 2. Control Experiments for C3-Alkylation of Indoles by Styrenes Using 2 as the Catalyst

(a) Reaction in the presence of **TEMPO**.
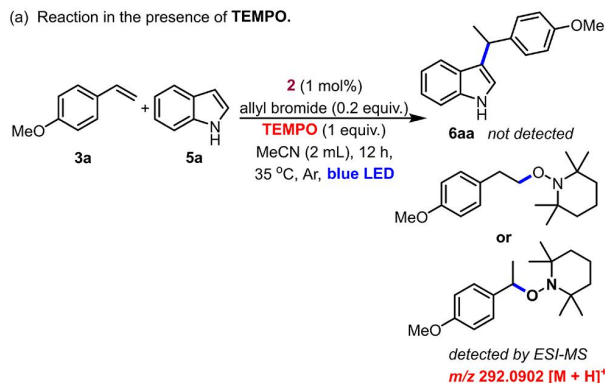
(b) Reaction in **CD$_3$CN**

(c) Deuterium labelling.
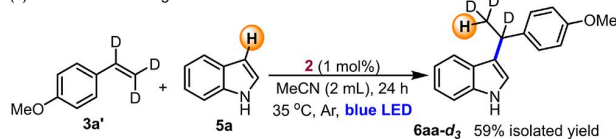
(d) Reaction in CD$_3$OD.
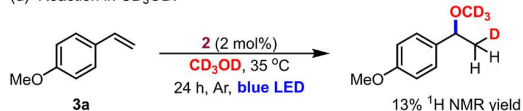
6aa was not observed as a product, but the ESI-MS showed evidence of radical adducts of TEMPO with both **3a** (m/z 292.0902 [M + H]^+) and allyl (m/z 197.9869 [M + H]^+) (Figures S38 and S39). The results of the experiments in the presence of TEMPO (Scheme 2a) and air (Table 1, entry 9) are indicative of radical intermediates in the reaction, particularly the formation of alkyl radicals. The products obtained from the reaction using CD$_3$CN excluded the solvent as a hydrogen-atom or proton source (Scheme 2b). However, using deuterated methoxystyrene (**3a′**, Scheme 2c), **6aa′** bearing a single H-atom on the terminal styrene carbon was obtained as the sole product in 59% isolated yield. The nucleophile served as the only proton source in this experiment, since no other additive was present. Similarly, upon irradiation of a solution of **3a** and **2** in CD$_3$OD, we obtained the alkoxylated product in Scheme 2d, in which both the OCD$_3$ group and D are transferred to the styrene in a Markovnikov fashion.

Guided by our combined experimental results, we propose the reaction cycle shown in Scheme 3. Upon excitation, the

Scheme 3. Proposed Mechanistic Pathway for Light-Driven C3/N-alkylation of Indoles 5 and Indazoles 7 with Styrenes 3 Catalyzed by 2
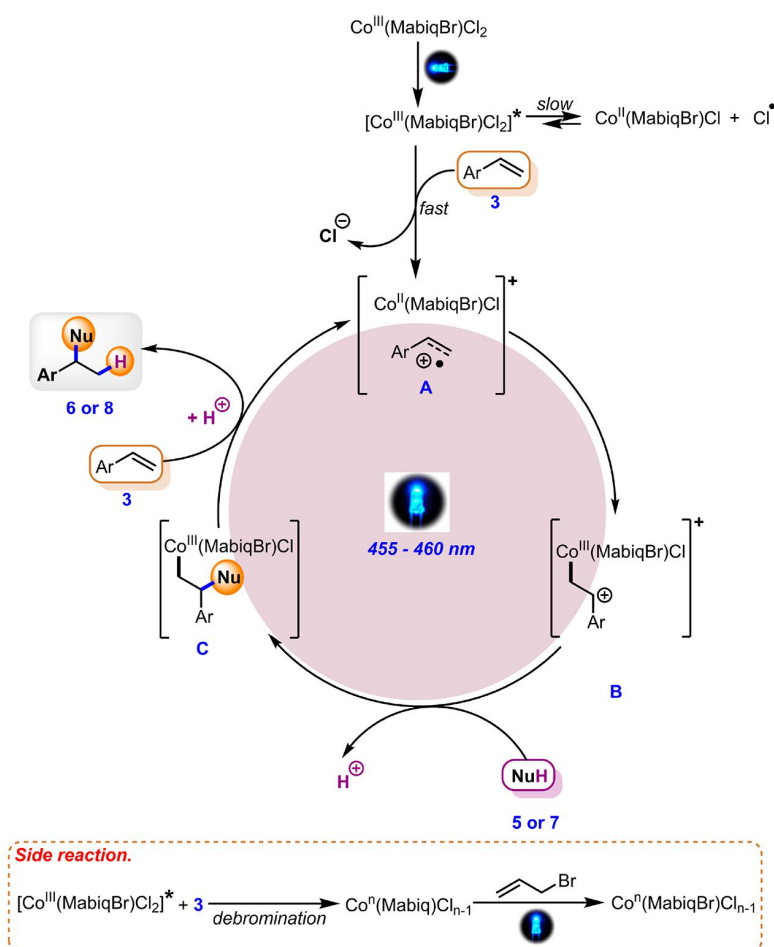
Co^{III} catalyst **2** oxidizes the styrene substrate,[62] forming Co^{II} and the substrate radical cation **A**. The Co^{II} form can also be generated by the light-driven homolysis of the Co−Cl bond in the absence of substrate, which also yields a chlorine radical. Substrate activation by halogen radicals, including chlorine radicals generated by VLIH of other M−chloride complexes, has previously been established.[12,66−69] However, the reported photoredox catalytic reactions all involve H-atom abstraction by chlorine radicals from an sp^3 carbon atom and frequently require an added chloride source. Furthermore, although both **1** and **2** can undergo Co−Cl bond homolysis, only **2** can catalyze the functionalization of indole with methoxystyrene in the absence of allyl bromide. Thus, we consider any alternate mechanisms involving chlorine radicals unlikely. At high styrene concentrations—as present under the catalytic conditions—the reaction between **2*** and **3a** predominates over Co−Cl bond homolysis. We have not seen any evidence of direct coordination of the substrate to the Co(III) complex in the absence of light. Nonetheless, we cannot rule out weak interactions between **2*** and **3a** that may facilitate electron transfer. The subsequent regioselective recombination of the radical pairs (Co^{II} and styrene radical cation) leads to the Markovnikov adduct **B** (detected by ESI-MS, m/z 813.6376 [M]$^+$), where the terminal carbon of the styrene is kinetically favored over the benzylic carbon. Structural features of the Co−Mabiq complex may regulate the observed regiochemis-

try.[18] Facile addition of the nucleophile affords **C**, followed by reduction of the ensuing Co^{III} intermediate by another styrene molecule and protonation of the alkyl adduct to give the desired product. We speculate that the addition of the nucleophile and subsequent reductive elimination of the desired product involves concerted rather than stepwise processes, as **C** was not detected by ESI-MS. Allyl bromide may sustain the active Co−MabiqBr form (Scheme 3, bottom), though the precise nature of the interaction between this molecule and the cobalt complex, and its further role in facilitating the reaction, remains to be ascertained.

We note that in related non-light-driven reactions by Co-salen systems[70−72] and dual Co-salen/photoredox-catalyzed hydrofunctionalization,[44] attack by a nucleophile was proposed to occur only at a highly electrophilic Co(IV) intermediate. However, the formation of Co(IV) species requires strong oxidants, which we did not employ.

Substrate Scope. We finally turned our attention to exploring the scope of the developed protocols, focusing on the indoles as well as extending the methodology to the related indazoles. Generally, the presence of an electron-donating group at the *para*-position of the styrene phenyl ring was relevant for reactivity in the reaction with indole **5a**. This reactivity was however unaffected by the moderately electron-withdrawing F-substituent *meta* to the vinyl group (Scheme 4). Monosubstituted styrenes **3a**−**3c** and **3i** afforded C3-alkylated

35

Scheme 4. Scope of Styrenes and Indoles for the C3-Alkylation of Indoles 5 with Styrenes 3 Photocatalyzed by 2[a]
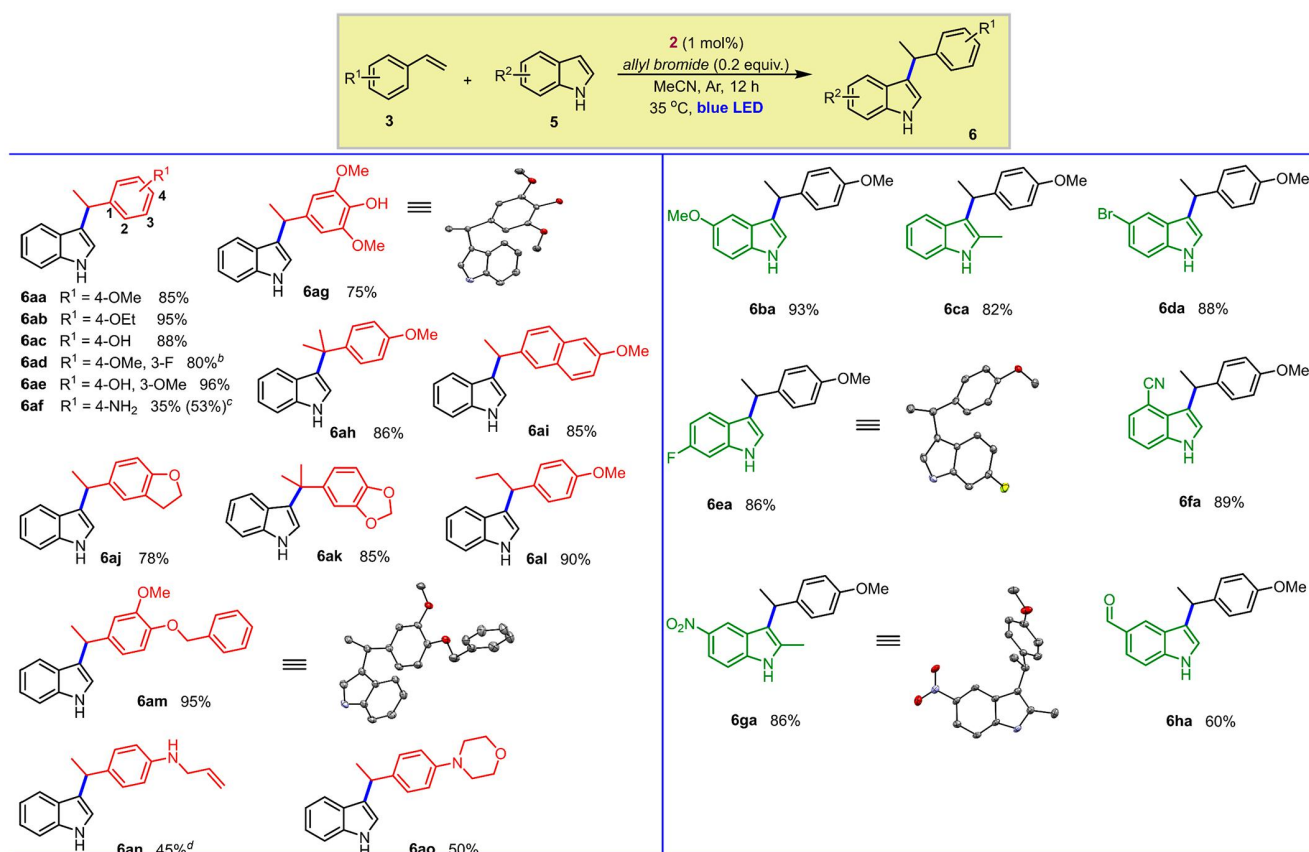
[a]Reaction conditions: **3** (0.2 mmol), **5** (0.2 mmol, 1 equiv), MeCN (dry, deoxygenated, 2 mL), blue LED (3 W, 455−460 nm). [b]Reaction time = 24 h. [c]The reaction was conducted without added allyl bromide. The yield given in parentheses represents the isolated yield after 24 h of irradiation. [d]The reaction was conducted with 0.5 equiv of allyl bromide.

indole products in very good-to-excellent yields, 85−95% (**6aa−6ac**, **6ai**). The 3-F-and-4-OMe-disubstituted styrene (**3d**) produced the alkylated indole product **6ad** in high yield (80%) after 24 h of irradiation. This demonstrates the utility of the reaction in the synthesis of F-containing indole pharmaceuticals.[73] Notably, styrenes containing a *meta*-OCH₃ group in addition to *para*-OH or -benzyloxy groups (**3e**, **3m**) performed excellently, affording almost quantitative yield of the desired products (**6ae**, **6am**). The trisubstituted and heterocyclic styrenes (**3g**, **3j**) also furnished the desired products in high yields (**6ag**, **6aj**). α- and β-substituted styrenes (**3h**, **3k**, **3l**) reacted favorably at the benzylic position to provide C3-alkylated products in very good-to-excellent yields (**6ah**, **6ak**, **6al**).

Interestingly, the reaction using 4-vinylaniline (**3f**) yielded a mixture of the expected product **6af** and **6an**, in which the amine group was additionally functionalized. By excluding allyl bromide from the reaction, **6af** was obtained as the only product in 35% (12 h) and 53% (24 h) isolated yields. By increasing the allyl bromide equivalent to 0.5 equiv, **6an** was obtained in 45% isolated yield (12 h), with **6af** in only 13% ¹H NMR yield. The formation of **6an** represents a mild one-pot synthetic route for the allylation of aminostyrenes and subsequent C3-alkylation of indole reaction. Finally, the morpholino-styrene **3o** afforded the alkylated indole product **6ao** in 50% yield.

The scope of indoles that underwent C3-alkylation with methoxystyrene **3a** was also assessed (Scheme 4). Generally, all indoles (**5b−5h**) examined furnished moderate-to-excellent yields of the desired products (**6ba−6ha**). The tolerance of this mild protocol to several functional groups on the indole moiety is noteworthy, thus allowing opportunities for further functionalization of these molecules.

The synthetic utility of this mild methodology was further examined with indazoles, which reacted favorably to afford N-alkylated indazoles (Scheme 5) in contrast to the C3-alkylation observed with indoles. The selectivity of the reaction is similar to that previously reported in the dual Co- and Ru-photocatalyzed alkylation,[44] with N2-selectivity slightly favored over N1-selectivity (combined yields of up to 95% and an N2:N1 ratio of up to 3:1). However, our protocol does not require protection of the indazole C3-position.[44] We also carried out preliminary studies with a few other nucleophiles. The reaction of **3a** with carbazole likewise yields the N-alkylated product **8ae** in moderate yields (63%, Scheme 5), whereas pyrrole is alkylated at the C3-position (42% yield, Table S15). Using either PhOH or sulfonamide, only the head-to-tail methoxystyrene dimer **4a** was observed (Table S15), which further highlights that, under the current conditions, high yields of C3- and N-alkylated products generally require a significantly nucleophilic coupling partner.

Scheme 5. Scope for the N-Alkylation of Indazoles 7 and of Carbazole with 4-Methoxystyrene 3a Photocatalyzed by 2
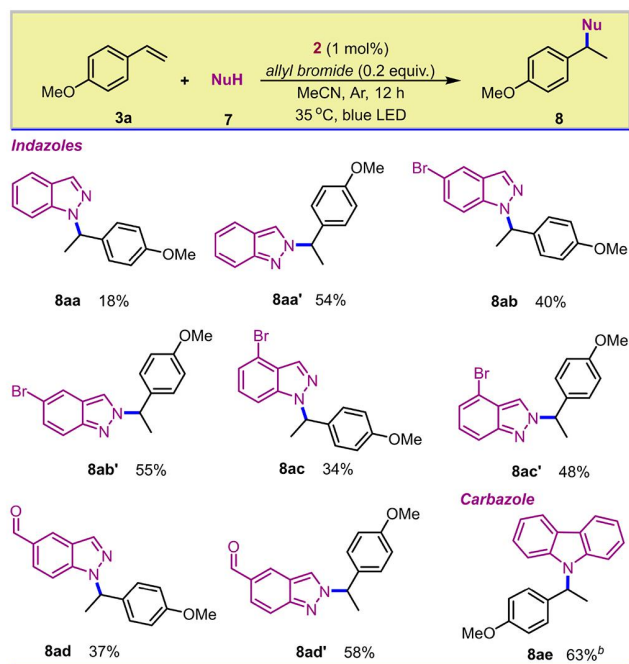
[a] Reaction conditions: **3a** (0.2 mmol), **7** (0.2 mmol, 1 equiv), MeCN (dry, deoxygenated, 2 mL), blue LED (3 W, 455−460 nm). *[b]* A 6% yield (¹H NMR) of **4a** was detected in this reaction.

CONCLUSION

In summary, we have shown that the Co(III) members of our Mabiq family can undergo VLIH and that the metal center can directly engage with substrates in the immediate coordination sphere. The comparative properties of **1** and of the MabiqBr-containing complex **2** demonstrate how ligand modification leads to key differences in photochemical behavior. Co-(MabiqBr)Cl₂, in particular, efficiently catalyzes the light-driven C3-alkylation of indoles with styrenes, the first photocatalytic example of this reaction. The chemistry generally proceeds with high yields, excellent functional group compatibility, as well as regioselectivity with respect to indoles, precluding the need for indole protection. Moreover, the reaction does not require any external oxidant/reductant, hydride donor, or a cocatalyst. Small amounts of added allyl bromide appear to facilitate the reaction, but the reaction catalyzed by **2** also can proceed in the absence of this molecule. Our work is thus particularly significant in the ability of the Co−Mabiq complex to adopt a dual role as both the organometallic and photoactive center. The observed activity of **2** in both C−C and C−N bond forming reactions points to further opportunities to utilize the Mabiq complexes for other light-driven functionalization reactions, which we are currently exploring. Overall, this work not only highlights the photocatalytic potential of the Mabiq complexes but underpins the substantial opportunities in developing first-row transition-metal photoredox catalysts that can adopt dual functions in metallaphotoredox catalytic processes.

ASSOCIATED CONTENT

Supporting Information

The Supporting Information is available free of charge at https://pubs.acs.org/doi/10.1021/jacs.1c10930.

Additional data (synthesis and reaction protocols; photochemical studies; absorption spectroscopy, mass spectrometry, ¹H NMR and ¹³C NMR data; crystallographic parameters) (PDF)

Accession Codes

CCDC 2076238−2076239 and 2115085−2115088 contain the supplementary crystallographic data for this paper. These data can be obtained free of charge via www.ccdc.cam.ac.uk/data_request/cif, or by emailing data_request@ccdc.cam.ac.uk, or by contacting The Cambridge Crystallographic Data Centre, 12 Union Road, Cambridge CB2 1EZ, UK; fax: +44 1223 336033.

AUTHOR INFORMATION

Corresponding Author

Corinna R. Hess − *Technical University of Munich, Department of Chemistry and Catalysis Research Center, 85748 Garching, Germany;* orcid.org/0000-0002-9607-9184; Email: corinna.hess@ch.tum.de

Authors

Oaikhena Zekeri Esezobor − *Technical University of Munich, Department of Chemistry and Catalysis Research Center, 85748 Garching, Germany*

Wenyi Zeng − *Technical University of Munich, Department of Chemistry and Catalysis Research Center, 85748 Garching, Germany*

Lukas Niederegger − *Technical University of Munich, Department of Chemistry and Catalysis Research Center, 85748 Garching, Germany*

Michael Grübel − *Technical University of Munich, Department of Chemistry and Catalysis Research Center, 85748 Garching, Germany*

Complete contact information is available at:
https://pubs.acs.org/10.1021/jacs.1c10930

ABBREVIATIONS

WE, working electrode; CE, counter electrode; RE, reference electrode

37

◾ REFERENCES

(1) Abderrazak, Y.; Bhattacharyya, A.; Reiser, O. Visible-Light-Induced Homolysis of Earth-Abundant Metal-Substrate Complexes: A Complementary Activation Strategy in Photoredox Catalysis. *Angew. Chem., Int. Ed.* **2021**, *60*, 21100−21115.

(2) Larsen, C. B.; Wenger, O. S. Photoredox Catalysis with Metal Complexes Made from Earth-Abundant Elements. *Chem. Eur. J.* **2018**, *24* (9), 2039−2058.

(3) Traub, L.; Reiser, O. Homogeneous visible light mediated transition metal catalysis other than Ruthenium and Iridium. *Phys. Sci. Rev.* **2019**, *4* (7), 1−19.

(4) Hockin, B. M.; Li, C.; Robertson, N.; Zysman-Colman, E. Photoredox catalysts based on earth-abundant metal complexes. *Catal. Sci. Technol.* **2019**, *9* (4), 889−915.

(5) Cheung, S. K. P.; Sarkar, S.; Gevorgyan, V. Visible Light-Induced Transition Metal Catalysis. *Chem. Rev.* **2022**, *122*, 1543.

(6) Prier, C. K.; MacMillan, D. W. C. Dual Photoredox Catalysis: The Merger of Photoredox Catalysis with Other Catalytic Activation Modes. *Visible Light Photocatalysis in Organic Chemistry* **2018**, 299−333.

(7) Skubi, K. L.; Blum, T. R.; Yoon, T. P. Dual Catalysis Strategies in Photochemical Synthesis. *Chem. Rev.* **2016**, *116* (17), 10035−10074.

(8) Zhu, C.; Yue, H.; Chu, L.; Rueping, M. Recent advances in photoredox and nickel dual-catalyzed cascade reactions: pushing the boundaries of complexity. *Chem. Sci.* **2020**, *11* (16), 4051−4064.

(9) Engl, S.; Reiser, O. Copper Makes the Difference: Visible Light-Mediated Atom Transfer Radical Addition Reactions of Iodoform with Olefins. *ACS Catal.* **2020**, *10* (17), 9899−9906.

(10) Ting, S. I.; Garakyaraghi, S.; Taliaferro, C. M.; Shields, B. J.; Scholes, G. D.; Castellano, F. N.; Doyle, A. G. (3)d-d Excited States of Ni(II) Complexes Relevant to Photoredox Catalysis: Spectroscopic Identification and Mechanistic Implications. *J. Am. Chem. Soc.* **2020**, *142* (12), 5800−5810.

(11) Hossain, A.; Bhattacharyya, A.; Reiser, O. Copper's rapid ascent in visible-light photoredox catalysis. *Science* **2019**, *364* (6439), eaav9713.

(12) Kariofillis, S. K.; Doyle, A. G. Synthetic and Mechanistic Implications of Chlorine Photoelimination in Nickel/Photoredox C(sp(3))-H Cross-Coupling. *Acc. Chem. Res.* **2021**, *54* (4), 988−1000.

(13) Hwang, S. J.; Powers, D. C.; Maher, A. G.; Anderson, B. L.; Hadt, R. G.; Zheng, S. L.; Chen, Y. S.; Nocera, D. G. Trap-Free Halogen Photoelimination from Mononuclear Ni(III) Complexes. *J. Am. Chem. Soc.* **2015**, *137* (20), 6472−6475.

(14) Giedyk, M.; Goliszewska, K.; Gryko, D. Vitamin B_{12} catalysed reactions. *Chem. Soc. Rev.* **2015**, *44* (11), 3391−404.

(15) Jones, A. R. The photochemistry and photobiology of vitamin B_{12}. *Photochem. Photobiol. Sci.* **2017**, *16* (6), 820−834.

(16) Pattenden, G. Cobalt-mediated Radical Reactions in Organic Synthesis. *Chem. Soc. Rev.* **1988**, *17*, 361−382.

(17) Schrauzer, G. N.; Sibert, J. W.; Windgassen, R. J. Photochemical and Thermal Cobalt-Carbon Bond Cleavage in Alkylcobalamins and Related Organometallic Compounds. A Comparative Study. *J. Am. Chem. Soc.* **1968**, *90* (24), 6681−6688.

(18) Potrzasaj, A.; Musiejuk, M.; Chaladaj, W.; Giedyk, M.; Gryko, D. Cobalt Catalyst Determines Regioselectivity in Ring Opening of Epoxides with Aryl Halides. *J. Am. Chem. Soc.* **2021**, *143* (25), 9368−9376.

(19) Bam, R.; Pollatos, A. S.; Moser, A. J.; West, J. G. Mild olefin formation via bio-inspired vitamin B_{12} photocatalysis. *Chem. Sci.* **2021**, *12* (5), 1736−1744.

(20) Kräutler, B. Photochemical Reactions of Vitamin B_{12} Derivatives. *Coord. Chem. Rev.* **1991**, *111*, 215−220.

(21) Toraya, T. Radical Catalysis in Coenzyme B12-Dependent Isomerization (Eliminating) Reactions. *Chem. Rev.* **2003**, *103*, 2095−2127.

(22) Debuigne, A.; Poli, R.; Jérôme, C.; Jérôme, R.; Detrembleur, C. Overview of cobalt-mediated radical polymerization: Roots, state of the art and future prospects. *Prog. Polym. Sci.* **2009**, *34* (3), 211−239.

(23) Demarteau, J.; Debuigne, A.; Detrembleur, C. Organocobalt Complexes as Sources of Carbon-Centered Radicals for Organic and Polymer Chemistries. *Chem. Rev.* **2019**, *119* (12), 6906−6955.

(24) Grübel, M.; Bosque, I.; Altmann, P. J.; Bach, T.; Hess, C. R. Redox and photocatalytic properties of a Ni(II) complex with a macrocyclic biquinazoline (Mabiq) ligand. *Chem. Sci.* **2018**, *9* (13), 3313−3317.

(25) Lauenstein, R.; Mader, S. L.; Derondeau, H.; Esezobor, O. Z.; Block, M.; Romer, A. J.; Jandl, C.; Riedle, E.; Kaila, V. R. I.; Hauer, J.; Thyrhaug, E.; Hess, C. R. The central role of the metal ion for photoactivity: Zn- vs. Ni-Mabiq. *Chem. Sci.* **2021**, *12* (21), 7521−7532.

(26) Puttock, E. V.; Banerjee, P.; Kaspar, M.; Drennen, L.; Yufit, D. S.; Bill, E.; Sproules, S.; Hess, C. R. A Series of [Co(Mabiq)Cl$_{2-n}$] (n = 0, 1, 2) Compounds and Evidence for the Elusive Bimetallic Form. *Inorg. Chem.* **2015**, *54* (12), 5864−5873.

(27) Kaspar, M.; Altmann, P. J.; Pothig, A.; Sproules, S.; Hess, C. R. A macrocyclic 'Co(0)' complex: the relevance of ligand non-innocence to reactivity. *Chem. Commun. (Camb)* **2017**, *53* (53), 7282−7285.

(28) Goyal, D.; Kaur, A.; Goyal, B. Benzofuran and Indole: Promising Scaffolds for Drug Development in Alzheimer's Disease. *ChemMedChem.* **2018**, *13* (13), 1275−1299.

(29) Kaushik, N. K.; Kaushik, N.; Attri, P.; Kumar, N.; Kim, C. H.; Verma, A. K.; Choi, E. H. Biomedical Importance of Indoles. *Molecules* **2013**, *18* (6), 6620−6662.

(30) Chadha, N.; Silakari, O. Indoles as therapeutics of interest in medicinal chemistry: Bird's eye view. *Eur. J. Med. Chem.* **2017**, *134*, 159−184.

(31) Nam, M. H.; Park, M.; Park, H.; Kim, Y.; Yoon, S.; Sawant, V. S.; Choi, J. W.; Park, J. H.; Park, K. D.; Min, S. J.; Lee, C. J.; Choo, H. Indole-Substituted Benzothiazoles and Benzoxazoles as Selective and Reversible MAO-B Inhibitors for Treatment of Parkinson's Disease. *ACS Chem. Neurosci.* **2017**, *8* (7), 1519−1529.

(32) Zhang, S. G.; Liang, C. G.; Zhang, W. H. Recent Advances in Indazole-Containing Derivatives: Synthesis and Biological Perspectives. *Molecules* **2018**, *23* (11), 2783.

(33) Festa, A. A.; Voskressensky, L. G.; Van der Eycken, E. V. Visible light-mediated chemistry of indoles and related heterocycles. *Chem. Soc. Rev.* **2019**, *48* (16), 4401−4423.

(34) Leitch, J. A.; Bhonoah, Y.; Frost, C. G. Beyond C2 and C3: Transition-Metal-Catalyzed C−H Functionalization of Indole. *ACS Catal.* **2017**, *7* (9), 5618−5627.

(35) Chen, J. B.; Jia, Y. X. Recent progress in transition-metal-catalyzed enantioselective indole functionalizations. *Org. Biomol. Chem.* **2017**, *15* (17), 3550−3567.

(36) Sandtorv, A. H. Transition Metal-Catalyzed C-H Activation of Indoles. *Adv. Synth. Catal.* **2015**, *357* (11), 2403−2435.

(37) Bandini, M.; Eichholzer, A. Catalytic functionalization of indoles in a new dimension. *Angew. Chem., Int. Ed.* **2009**, *48* (51), 9608−44.

(38) Milcendeau, P.; Sabat, N.; Ferry, A.; Guinchard, X. Gold-catalyzed enantioselective functionalization of indoles. *Org. Biomol. Chem.* **2020**, *18* (31), 6006−6017.

(39) Ghosh, S.; Mondal, S.; Hajra, A. Direct Catalytic Functionalization of Indazole Derivatives. *Adv. Synth. Catal.* **2020**, *362* (18), 3768−3794.

(40) Moselage, M.; Li, J.; Ackermann, L. Cobalt-Catalyzed C−H Activation. *ACS Catal.* **2016**, *6*, 498−525.

(41) Ye, Y.; Kim, S. T.; Jeong, J.; Baik, M. H.; Buchwald, S. L. CuH-Catalyzed Enantioselective Alkylation of Indole Derivatives with Ligand-Controlled Regiodivergence. *J. Am. Chem. Soc.* **2019**, *141* (9), 3901−3909.

(42) Pathak, T. P.; Sigman, M. S. Palladium-catalyzed Hydrofunctionalization of Vinyl Phenol Derivatives with Heteroaromatics. *Org. Lett.* **2011**, *13*, 2774−2777.

(43) Pathak, T. P.; Gligorich, K. M.; Welm, B. E.; Sigman, M. S. Synthesis and Preliminary Biological Studies of 3-substituted Indoles

accessed by a Palladium-catalyzed Enantioselective Alkene Difunctionalization Reaction. *J. Am. Chem. Soc.* **2010**, *132*, 7870−7871.

(44) Sun, H.-L.; Yang, F.; Ye, W.-T.; Wang, J.-J.; Zhu, R. Dual Cobalt and Photoredox Catalysis Enabled Intermolecular Oxidative Hydrofunctionalization. *ACS Catal.* **2020**, *10* (9), 4983−4989.

(45) Stark, H. S.; Altmann, P. J.; Sproules, S.; Hess, C. R. Structural Characterization and Photochemical Properties of Mono- and Bimetallic Cu-Mabiq Complexes. *Inorg. Chem.* **2018**, *57* (11), 6401−6409.

(46) Hopkinson, M. N.; Gomez-Suarez, A.; Teders, M.; Sahoo, B.; Glorius, F. Accelerated Discovery in Photocatalysis using a Mechanism-Based Screening Method. *Angew. Chem., Int. Ed.* **2016**, *55* (13), 4361−4366.

(47) Buzzetti, L.; Crisenza, G. E. M.; Melchiorre, P. Mechanistic Studies in Photocatalysis. *Angew. Chem., Int. Ed.* **2019**, *58* (12), 3730−3747.

(48) Berger, A. L.; Donabauer, K.; König, B. Photocatalytic Barbier reaction − visible-light induced allylation and benzylation of aldehydes and ketones. *Chem. Sci.* **2018**, *9* (36), 7230−7235.

(49) Kondo, T.; Takagi, D.; Tsujita, H.; Ura, Y.; Wada, K.; Mitsudo, T.-a. Highly Selective Dimerization of Styrenes and Linear Co-dimerization of Styrenes with Ethylene Catalyzed by a Ruthenium Complex. *Angew. Chem., Int. Ed.* **2007**, *46* (31), 5958−5961.

(50) Khlebnikov, V.; Meduri, A.; Mueller-Bunz, H.; Montini, T.; Fornasiero, P.; Zangrando, E.; Milani, B.; Albrecht, M. Palladium Carbene Complexes for Selective Alkene Di- and Oligomerization. *Organometallics* **2012**, *31* (3), 976−986.

(51) Miyake, Y.; Moriyama, T.; Tanabe, Y.; Onodera, G.; Nishibayashi, Y. Remarkable Effect of Valence Electrons in Thiolato-Bridged Diruthenium Complexes toward Catalytic Dimerization of α-Methylstyrenes. *Organometallics* **2011**, *30* (21), 5972−5977.

(52) Cabrero-Antonino, J. R.; Leyva-Pérez, A.; Corma, A. Iron-Catalysed Regio- and Stereoselective Head-to-Tail Dimerisation of Styrenes. *Adv. Synth. Catal.* **2010**, *352* (10), 1571−1576.

(53) Lee, D. W.; Yi, C. S. Chain- and Regioselective Ethylene and Styrene Dimerization Reactions Catalyzed by a Well-Defined Cationic Ruthenium-Hydride Complex: New Insights on the Styrene Dimerization Mechanism. *Organometallics* **2010**, *29* (15), 3413−3417.

(54) Shey, J.; McGinley, C. M.; McCauley, K. M.; Dearth, A. S.; Young, B. T.; van der Donk, W. A. Mechanistic Investigation of a Novel Vitamin B$_{12}$-Catalyzed Carbon-Carbon Bond Forming Reaction, the Reductive Dimerization of Arylalkenes. *J. Org. Chem.* **2002**, *67*, 837−846.

(55) Wang, C.-C.; Lin, P.-S.; Cheng, C.-H. Cobalt-catalyzed dimerization of alkenes. *Tetrahedron Lett.* **2004**, *45* (32), 6203−6206.

(56) Shevick, S. L.; Wilson, C. V.; Kotesova, S.; Kim, D.; Holland, P. L.; Shenvi, R. A. Catalytic hydrogen atom transfer to alkenes: a roadmap for metal hydrides and radicals. *Chem. Sci.* **2020**, *11* (46), 12401−12422.

(57) Crossley, S. W.; Obradors, C.; Martinez, R. M.; Shenvi, R. A. Mn-, Fe-, and Co-Catalyzed Radical Hydrofunctionalizations of Olefins. *Chem. Rev.* **2016**, *116* (15), 8912−9000.

(58) Yahata, K.; Kaneko, Y.; Akai, S. Cobalt-Catalyzed Intermolecular Markovnikov Hydroamination of Nonactivated Olefins: N(2)-Selective Alkylation of Benzotriazole. *Org. Lett.* **2020**, *22* (2), 598−603.

(59) Shen, X.; Chen, X.; Chen, J.; Sun, Y.; Cheng, Z.; Lu, Z. Ligand-promoted cobalt-catalyzed radical hydroamination of alkenes. *Nat. Commun.* **2020**, *11* (1), 783.

(60) Kattamuri, P. V.; West, J. G. Hydrogenation of Alkenes via Cooperative Hydrogen Atom Transfer. *J. Am. Chem. Soc.* **2020**, *142* (45), 19316−19326.

(61) Sun, J.; Deng, L. Cobalt Complex-Catalyzed Hydrosilylation of Alkenes and Alkynes. *ACS Catal.* **2016**, *6* (1), 290−300.

(62) Nguyen, T. M.; Manohar, N.; Nicewicz, D. A. anti-Markovnikov hydroamination of alkenes catalyzed by a two-

component organic photoredox system: direct access to phenethyl-amine derivatives. *Angew. Chem., Int. Ed.* **2014**, *53* (24), 6198−201.

(63) Romero, N. A.; Nicewicz, D. A. Mechanistic insight into the photoredox catalysis of anti-markovnikov alkene hydrofunctionalization reactions. *J. Am. Chem. Soc.* **2014**, *136* (49), 17024−35.

(64) Wilger, D. J.; Grandjean, J. M.; Lammert, T. R.; Nicewicz, D. A. The direct anti-Markovnikov addition of mineral acids to styrenes. *Nat. Chem.* **2014**, *6* (8), 720−6.

(65) Weiser, M.; Hermann, S.; Penner, A.; Wagenknecht, H. A. Photocatalytic nucleophilic addition of alcohols to styrenes in Markovnikov and anti-Markovnikov orientation. *Beilstein J. Org. Chem.* **2015**, *11*, 568−575.

(66) Yang, Q.; Wang, Y.-H.; Qiao, Y.; Gau, M.; Carroll, P. J.; Walsh, P. J.; Schelter, E. J. Photocatalytic C−H activation and the subtle role of chlorine radical complexation in reactivity. *Science* **2021**, *372*, 847−852.

(67) Jia, P.; Li, Q.; Poh, W. C.; Jiang, H.; Liu, H.; Deng, H.; Wu, J. Light-Promoted Bromine-Radical-Mediated Selective Alkylation and Amination of Unactivated C(sp3)−H Bonds. *Chem.* **2020**, *6* (7), 1766−1776.

(68) Holmberg-Douglas, N.; Nicewicz, D. A. Photoredox-Catalyzed C-H Functionalization Reactions. *Chem. Rev.* **2022**, *122*, 1925.

(69) Lin, R.; Amrute, A. P.; Perez-Ramirez, J. Halogen-Mediated Conversion of Hydrocarbons to Commodities. *Chem. Rev.* **2017**, *117* (5), 4182−4247.

(70) Date, S.; Hamasaki, K.; Sunagawa, K.; Koyama, H.; Sebe, C.; Hiroya, K.; Shigehisa, H. Catalytic Direct Cyclization of Alkenyl Thioester. *ACS Catal.* **2020**, *10* (3), 2039−2045.

(71) Discolo, C. A.; Touney, E. E.; Pronin, S. V. Catalytic Asymmetric Radical-Polar Crossover Hydroalkoxylation. *J. Am. Chem. Soc.* **2019**, *141* (44), 17527−17532.

(72) Ebisawa, K.; Izumi, K.; Ooka, Y.; Kato, H.; Kanazawa, S.; Komatsu, S.; Nishi, E.; Shigehisa, H. Catalyst- and Silane-Controlled Enantioselective Hydrofunctionalization of Alkenes by Cobalt-Catalyzed Hydrogen Atom Transfer and Radical-Polar Crossover. *J. Am. Chem. Soc.* **2020**, *142* (31), 13481−13490.

(73) Inoue, M.; Sumii, Y.; Shibata, N. Contribution of Organo-fluorine Compounds to Pharmaceuticals. *ACS Omega* **2020**, *5* (19), 10633−10640.

39

Chapter 3

The central role of the metal ion for photoactivity: Zn– vs. Ni–Mabiq

Authors: Raphael Lauenstein, Sophie L. Mader, Henrieta Derondeau, **Oaikhena Z. Esezobor**, Matthias Block, Armin J. Römer, Christian Jandl, Eberhard Riedle, Ville R. I. Kaila, Jürgen Hauer, Erling Thyrhaug and Corinna R. Hess

Summary: This work describes the photophysical and photocatalytic properties of Ni- and Zn-complexes based on the non-innocent macrocyclic biquinazoline ligand (Mabiq). A comparative study of both complexes employing steady state, time resolved optical spectroscopy, time-dependent density functional theory (TDDFT) calculations and photoredox catalyzed reactions was carried out. Although the [Ni(Mabiq)]OTf and [Zn(Mabiq)]OTf complexes have comparable UV-Vis characteristics, photochemical studies revealed that both complexes are different in the excited state. While [Ni(Mabiq)]OTf exhibits metal-centered excited states, [Zn(Mabiq)]OTf on the other hand exhibit ligand-centered excited state, a property that influences the activity of both complexes in photoredox catalyzed reactions. The complexes were able to catalyze, via SET, the cyclization of bromo-alkyl substituted indole, photo-driven aza-Henry reaction, and oxidative coupling of methoxybenzylamine, producing different yields of the products. A fundamental difference between both complexes during photoinduced catalysis is the stability of the complexes – the reduced $Zn^{II}(Mabiq^\bullet)$ *(formally denoted as $Zn^I(Mabiq))$,* is unstable upon continued irradiation, while the $Ni^{II}(Mabiq^\bullet)$ *(formally denoted as $Ni^I(Mabiq)),$* remains stable over a long period of time.

Contributions of Authors:

Oaikhena Z. Esezobor planned and performed the photoredox catalyzed reactions under the supervision of Corinna R. Hess.

Check for updates

The central role of the metal ion for photoactivity: Zn– *vs.* Ni–Mabiq†

Raphael Lauenstein,[a] Sophie L. Mader, [b] Henrieta Derondeau, [c] Oaikhena Z. Esezobor,[a] Matthias Block,[c] Armin J. Römer,[b] Christian Jandl,[a] Eberhard Riedle, [c] Ville R. I. Kaila, ‡[b] Jürgen Hauer,[a] Erling Thyrhaug *[a] and Corinna R. Hess *[a]

Photoredox catalysts are integral components of artificial photosystems, and have recently emerged as powerful tools for catalysing numerous organic reactions. However, the development of inexpensive and efficient earth-abundant photoredox catalysts remains a challenge. We here present the photochemical and photophysical properties of a Ni–Mabiq catalyst ([Ni^{II}(Mabiq)]OTf (**1**); Mabiq = 2-4:6-8-bis(3,3,4,4-tetramethyldihydropyrrolo)-10-15-(2,2-biquinazolino)-[15]-1,3,5,8,10,14-hexaene1,3,7,9,11,14-N$_6$)—and of a Zn-containing analogue ([Zn^{II}(Mabiq)OTf] (**2**))—using steady state and time resolved optical spectroscopy, time-dependent density functional theory (TDDFT) calculations, and reactivity studies. The Ni and Zn complexes exhibit similar absorption spectra, but markedly different photochemical properties. These differences arise because the excited states of **2** are ligand-localized, whereas metal-centered states account for the photoactivity of **1**. The distinct properties of the Ni and Zn complexes are manifest in their behavior in the photo-driven aza-Henry reaction and oxidative coupling of methoxybenzylamine.

Introduction

The breadth of light-driven chemical transformations has rapidly expanded over the last decade, due to a surge of research in photoredox catalysis.[1–8] Photoredox catalysts are used not only for solar fuel applications,[9–13] but also as components of complex catalytic processes that couple photosensitizers with secondary organic, transition metal or Lewis acid catalysts.[14–16] Consequently, contemporary developments in light mediated catalysis have enabled unique reactivities beyond what organometallic catalysts alone can achieve. Photocatalysts thus have emerged as important tools for sustainable chemistry and renewable energy needs.

An ensuing challenge within the field is to develop an array of photosensitizers for these varied catalytic processes. The conventional noble metal complexes, Ru and Ir polypyridyl complexes, remain the 'workhorses' of photoredox catalysis.[1,17–19] However, the scarcity and cost of these elements significantly limits their applications. Alternative catalysts based on low-cost, earth-abundant elements are clearly needed.

While chemical behavior is generally similar within a given group of elements, the simple approach of replacing 2nd and 3rd row transition metal complexes with earth-abundant 1st row analogues is not straightforward. A major complicating factor is the often dramatically different photophysics of the lighter elements. A striking example is provided by the Ru^{II} polypyridyl complexes, which tend to form metal-to-ligand charge transfer (MLCT) states with lifetimes approaching microseconds.[17] In contrast, ferrous analogues are notoriously short lived, with relaxation to high-spin metal-centered (MC) states often proceeding on the sub-picosecond timescale.[20] Nevertheless, there have been several exciting developments with respect to earth-abundant photoredox catalysts, including first-row transition metal complexes based on Zr, and Cr through Zn.[21–24] Moreover, sophisticated efforts are being made to design and tailor ligand scaffolds and impose desirable electronic structure features on the coordinated metal. Variation of the transition metal clearly can also alter the photophysical and chemical properties among complexes based on a given ligand system. However, systematic investigations with a broad range of M–ligand complexes in this context are limited.

Our own efforts in this regard center on the development of photosensitizers based on the macrocyclic biquinazoline ligand, Mabiq. We recently demonstrated that both

[a] Department of Chemistry and Catalysis Research Center, Technical University of Munich, Lichtenbergstr. 4, 85747 Garching, Germany. E-mail: corinna.hess@ch.tum.de; erling.thyrhaug@tum.de

[b] Department of Chemistry, Technical University of Munich, Lichtenbergstr. 4, 85747 Garching, Germany

[c] Lehrstuhl für BioMolekulare Optik, Fakultät für Physik, Ludwig-Maximilians-Universität München, Oettingenstr. 67, 80538 Munich, Germany

† Electronic supplementary information (ESI) available: Experimental procedures, spectroscopic and TDDFT data, crystallographic tables and CIF file. CCDC 1949717. For ESI and crystallographic data in CIF or other electronic format see DOI: 10.1039/d0sc06096h

‡ Present address: Department of Biochemistry and Biophysics, Stockholm University, Stockholm, Sweden.

[Cu^{II}(Mabiq)OTf] and [Ni^{II}(Mabiq)]OTf (**1**, Fig. 1) can be photoreduced in the presence of a sacrificial donor to the corresponding neutral [M^{II}(Mabiq·)]^0—formally 'M^I·§—forms.[25,26] Likewise, we have now verified the ability to photoreduce the Fe–, Co–, and Zn–Mabiq complexes (*vide infra*). Furthermore, **1** acts as an effective photoredox catalyst for the cyclization of a bromoalkyl-substituted indole.[25] To our knowledge, no other ligand system can support similar photoredox behavior with such a wide range of metal ions, but the excited state mechanisms involved in these processes remain elusive.

In this work, we have focused our attention on the detailed photochemical and photophysical studies of the Ni complex **1**, a confirmed photocatalyst. We aimed to obtain a deeper understanding of the root of its photoactivity by probing the excited state structure and dynamics of this compound, using spectroscopic and computational methods. As a benchmark, we compare the results with the zinc–Mabiq analogue ([Zn^{II}(Mabiq)OTf], **2**, Fig. 1). In contrast to the Ni compound, the fully occupied d-orbitals of the redox-inert Zn ion are not expected to contribute significantly to the spectroscopic and redox properties of the complex. Thus, a comparative study of these complexes is expected to yield valuable information about how the overall properties are altered by varied metal–ligand interactions. We present results for both complexes using a combination of steady state and transient optical spectroscopy, time-dependent density functional theory (TDDFT) calculations, and reactivity studies. In addition, we examined the comparative activities of the two compounds in select photocatalytic reactions. The comparative properties and

reactivity of **1** and **2**—alongside select supporting studies of the Fe– and Co–Mabiq complexes—provide insight into the unique characteristics and potential applications of the metal–Mabiq (M–Mabiq) system.

Results and discussion

Compound **2** was generated according to an established procedure for M^{II}–Mabiq synthesis,[27] and its composition was verified by mass spectrometry, ^{1}H NMR spectroscopy and CHN analysis (see ESI and Fig. S1† for details).

In the solid state, complex **2** adopts a square pyramidal geometry (Fig. 1), with the triflate ligand in the apical position (Zn–O = 2.0661(15) Å). The ligand is significantly less buckled than the uncomplexed HMabiq,[28] as also observed in the structure of **1**.[25] The ^{19}F NMR spectra (Fig. S2 and S3†) of **2** show a single resonance in both DCM-d$_2$ (−79 ppm) and MeCN-d$_3$ (−78 ppm), similar to the spectrum of **1** (−79 ppm, MeCN-d$_3$; Fig. S4†). Thus, the triflate molecule of **2** may dissociate in solution. The ^{1}H NMR of the complex in MeCN-d$_3$ with added Et$_3$N (500 equiv., Fig. S6†) shows two species, which indicates that the amine also may coordinate at high concentrations.

Optical properties: steady-state spectra

The absorption spectra of **1** and **2** (Fig. 2, top) are overall similar in structure. Both feature a moderately intense progression of bands in the blue-green spectral region (λ_{max} = 489 nm/2.53 eV and 457 nm/2.71 eV, respectively), followed by more intense transitions in the near-UV. These characteristic absorption features also dominate the visible spectra of Co^{III}– and Cu^{II}– Mabiq complexes,[26,29] and are recognizable in the spectra of
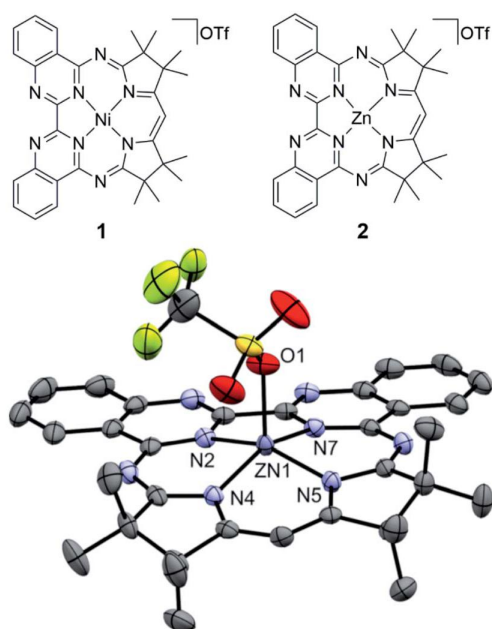
Fig. 1 (Top) Chemical structure of **1** and **2**. (Bottom) Molecular structure of the newly synthesized **2** (50% ellipsoids; solvent molecules and hydrogen atoms omitted for clarity).
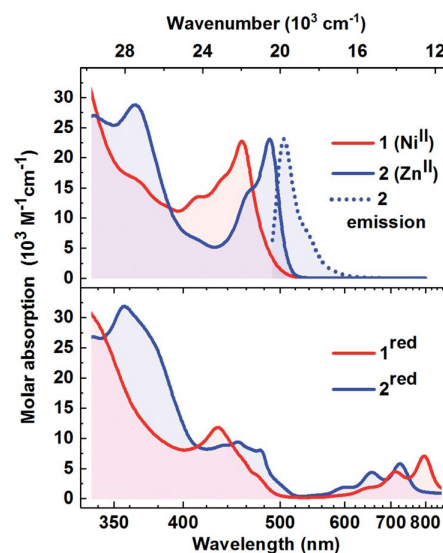
Fig. 2 Top: Absorption spectra (1 : 1, THF : MeCN) of **1** (red) and **2** (blue). The emission spectrum of **2** (λ_{max} = 505 nm) is shown by the dotted trace. Bottom: Absorption spectra of the photoreduced forms of **1** (**1**^{red}; red) and of **2** (**2**^{red}; blue); 1 : 1, THF : MeCN (see Fig. S13 and S16† for photoreduction data).

other M^n–Mabiq compounds.[27] The similarity among a fairly large range of coordination compounds suggests that these features predominantly involve ligand-localized (singlet) states. In support of this, we note that for both **1** and **2** (Fig. S8 and S9†) the absorption spectra are essentially solvent-insensitive, implying that at least the initial excitation has negligible charge-transfer (CT) character. Despite the similarities among the absorption spectra, the photo-chemical and -physical behavior of the complexes differ markedly and are strongly dependent on the metal center, as illustrated by our studies with **1** and **2** (*vide infra*).

Appreciable luminescence is only observed for **2**, which has an emission quantum yield approaching 0.7 in DCM. The Stokes shift is modest and the emission spectrum (Fig. 2, top, dotted line) exhibits mirror-image symmetry with the absorption. The emission wavelength is close in energy to the very weak emission observed for the [Cu^{II}(Mabiq)OTf] (513 nm),[26] as well as of the uncoordinated Mabiq ligand (501 nm; Fig. S7b†), as a further indication of the ligand-centered character of the transitions. In stark contrast to this dye-like optical behaviour, the Ni-containing **1**—as well as the other open d-shell M^n–Mabiq compounds that we have examined (*vide infra*)—is effectively non-emissive (quantum yield $< 10^{-4}$). This might be expected, as the open-shell configuration of **1** allows for relaxation pathways involving optically dark MC and MLCT/LMCT states.

O$_2$ sensitization

Structurally related Zn pyrrin- and pyrrole-based complexes act as singlet oxygen photosensitizers, which has prompted interest in such compounds for photodynamic therapy.[30–32] To probe the potential formation of triplet states in our system, we examined singlet oxygen generation by **1** and **2**, using dihydroxynapthalene (DHN) as a $^1O_2$ scavenger (Fig. S28 and S30†). Based on the absorption of the oxidized product, juglone, a reaction yield of 10% was determined using **2** as the photosensitizer. In contrast to **2**, **1** does not act as a $^1O_2$ photosensitizer: no changes were observed in the absorption spectrum upon irradiation of an aerated **1**/DHN solution (Fig. S30†). This could suggest that intersystem crossing (ISC) is not the primary luminescence quenching route for **1**. However, other factors should be taken into consideration: the triplet excited state may be too short-lived to efficiently participate in diffusion-controlled reactions with O$_2$; the $^3Ni^{II*}$ energy may be insufficient for the sensitization; or triplet–triplet annihilation may be sterically hindered. Our work (*vide infra*), as well as recent work on other Ni^{II} photocatalysts,[33] implies that this lack of sensitization is predominantly due to the low energy of the $^3Ni^{II*}$ state.

Photoreduction

Compound **2** can be photoreduced in the presence of Et$_3$N as a sacrificial donor, in accord with the photochemical behaviour of **1** and the Cu–Mabiq complexes (Scheme 1).[25,26] Upon irradiation of a solution of **2** (λ = 455 nm), a series of new bands appears in the red spectral region, coincident with a decrease in the higher energy absorption bands of [Zn(Mabiq)OTf] (Fig. 2,
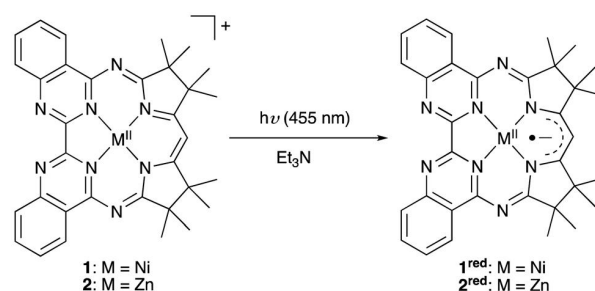
Scheme 1 The series of M–Mabiq complexes (M = Fe, Co, Ni, Cu, Zn) can be photoreduced upon irradiation at λ = 455 nm, in the presence of a sacrificial donor.

S15 and S16†). The product spectrum is identical to that of the chemically generated [Zn^{II}(Mabiq$^{\cdot}$)] (**2^{red}**),[27] confirming that **2** undergoes one-electron reduction during the photochemical reaction. The photoreduction to **2^{red}** is both fast, reaching completion within seconds (at [**2**] = 77 μM, P_{ref} = 248 mW, [Et$_3$N] = 38.5 mM, MeCN : THF = 1 : 1; Fig. S15†), and efficient (quantum yield of 0.79 as determined at P_{ref} = 1.4 mW, [Et$_3$N] = 345 μM; Fig. S16 and S17†). The yield is three orders of magnitude larger than the photoreduction yield of **1** (see ref. 25 and Fig. S13 and S14;† Φ = 2.9 × 10^{-4} at [**1**] = 67 μM, P_{ref} = 245 mW, [Et$_3$N] = 33.5 mM). However, the photogenerated **2^{red}** decays shortly after its formation, as seen by the disappearance of its 550–800 nm features, and the concomitant emergence of new bands below 500 nm. These latter bands also subsequently decrease in intensity. We note that the ability to chemically synthesize and isolate [Zn^{II}(Mabiq$^{\cdot}$)][27] indicates that the reduced form of the Zn complex is not inherently unstable, but that the decomposition is light-driven under the photoreduction conditions. The photo-decomposition of **2^{red}** is unique in the M^n–Mabiq series, as the corresponding Ni and Cu complexes are stable indefinitely under analogous conditions.[25,26] Similarly, the photoreduction of the two open-shell Fe^{II}– and Co^{II}–Mabiq complexes, [Fe^{II}(Mabiq)(MeCN)$_2$]PF$_6$ and [Co^{II}(Mabiq)(THF)]PF$_6$, also leads to photostable reduced products (Fig. S18 and S21†) with quantum yields comparable to that of **1** (Fe: 1.8 × 10^{-4}; Co: 3.6 × 10^{-4}). The ability of Et$_3$N to coordinate to **2**, as evidenced by ^{1}H NMR, may contribute to the rapid photoreduction of this particular complex in the series, as well as the subsequent instability of **2^{red}**.

In order to assess potential specific interactions between the reducing agent and the M–Mabiq compounds, we additionally examined the photoreduction of **1** by two other sacrificial donors: dimethylaniline (DMA) and *N*-(2,4,6-trimesitylbenzyl)dicyclohexylamine (N(CH$_2$Mes)Cy$_2$). Structurally, the donors differ significantly from Et$_3$N. The nitrogen atom of N(CH$_2$Mes)Cy$_2$ is hindered by the bulky cyclohexyl and mesityl groups, which might (partially) inhibit collisional quenching and ground-state pre-association. The aniline moiety of DMA also is a poor ligand relative to triethylamine. However, these molecules have comparable oxidation potentials to Et$_3$N (E^{ox} (*vs.* SCE, MeCN): DMA = *ca.* 0.7 V;[34] N(CH$_2$Mes)Cy$_2$ = 0.78 V (ref. 25)). Therefore, the

amines should readily reduce $Ni^{II}*$ if photoreduction occurs in an outer-sphere, diffusion-controlled manner.

The NMR spectrum of the Ni complex was unaltered upon addition of >100 equiv. (>0.5 M) of any of the three reductants to solutions of **1** (see ESI and Fig. S5a and b†). Thus, as expected for the square planar d^8 complex we find no evidence of ground-state coordination or non-covalent interactions of the reductants to **1**. Nevertheless, we observe substantial differences in the photoreduction efficiency. The photoreduction of **1** by $N(CH_2Mes)Cy_2$ proceeds with a yield that is nearly identical to that using triethylamine ($\Phi = 2.1 \times 10^{-4}$ at $[\mathbf{1}] = 67$ μM, $P_{ref} = 245$ mW, $[(N(CH_2Mes)Cy_2)] = 33.5$ mM; Fig. S23†). However, only low yields of $\mathbf{1}^{red}$ were obtained using DMA, even with 10-fold higher concentrations of the reductant ($\Phi = 5 \times 10^{-5}$ at $[\mathbf{1}] = 51$ μM, $P_{ref} = 245$ mW, $[DMA] = 255$ mM; Fig. S24†). The oxidized forms of all three donor molecules examined here should have limited chemical stability; a factor which is critical to efficient photoreduction.[34] Nonetheless, factors beyond the redox potential clearly have an impact on the photoreduction.

Excited-state relaxation dynamics

The steady state absorption/emission spectroscopy, oxygen sensitization, and photoreduction experiments described above imply that, although the initial excitation of **1** and **2** is to states of similar character, the subsequent relaxation dynamics are substantially different. To elucidate these relaxation processes, time-resolved optical spectroscopies are the method of choice.

Using time-resolved fluorescence spectroscopy, only the excited state dynamics of **2** can be addressed conveniently (Fig. S27†). As **1** is essentially non-emissive, its relaxation dynamics must be followed by ultrafast transient absorption (TA) spectroscopy.[35,36] To investigate both **1** and **2** on common footing, and to monitor dynamics beyond the relaxation of the Mabiq-localized excited singlet state, we recorded their fs/ps TA spectra in the 1 : 1 MeCN : THF solvent system relevant to the photocatalytic experiments (Fig. 3; noteworthy delay times and spectral positions are indicated by the horizontal and vertical lines in (a) and (d)). Spectra for both complexes during the subsequent ns/μs time range are shown in Fig. S35 and S38.† All decay constants determined from a comprehensive analysis, along with our assignments, are summarized in Table 1. While the statistical errors (see Table S11†) in the multi-exponential fit model are small, multi-component models are delicate. We therefore supply this uncertainty estimate with an estimate of the upper bound of possible parameter ranges from the peak-widths of a maximum entropy analysis (*vide infra*). This analysis yields ranges of approximately 50% of the mean value. Notably, even using this highly conservative upper bound the time constants remain well separated and we can safely consider the reported time-constants as meaningful.

A number of significant differences in the spectral evolution of the two complexes are readily apparent—in particular, the dynamics of **1** are faster and more complicated on the fs/ps time scale. We outline these differences in detail in the following sections.

Time-evolution of transient spectra. The time-resolved fluorescence of **2** shows that the initially populated state—a ligand-centered singlet—decays mono-exponentially with a 1.1 ns lifetime (Fig. S27†). While fluorescence provides only limited information about the excited-state behaviour, it suggests that at least the initial photophysics is relatively simple.

The fluorescence properties can be compared with observations from TA. Immediately on excitation, both **1** and **2** feature stimulated emission (SE) to the red of the excitation wavelength—*i.e.*, the longest wavelength absorption band—and a broad featureless excited-state absorption (ESA) band extending into the near-IR. These early time spectra can be assigned to ligand-localized singlet states, referred to as $^1Ni^{II}*$ and $^1Zn^{II}*$ respectively from here on (singlet and triplet notations refer to the overall spin state of the complex).

We can follow the dynamics of these initial singlet excited states by the transient kinetics around the excitation wavelength and in the long-wavelength region (magenta and brown vertical cuts in Fig. 3a and d, respectively).

The initial TA kinetics of **2** semi-quantitatively matches the time constant of the fluorescence decay, as the SE decays with a time-constant close to the 1 ns length of the optical delay stage. Beyond this loss of stimulated emission, only subtle changes occur in the spectra during this time period, as illustrated by both vertical (Fig. 3e) and horizontal cuts (Fig. 3f) through the TA data. These changes can be attributed to solvation dynamics and small-scale geometric relaxation.

The corresponding kinetic traces of **1** (Fig. 3b), on the other hand, exhibit much faster and more complicated behaviour, with a concomitant decay of the long-wavelength ESA and SE on a timescale of only ∼1 ps. This rapid decay of the SE signal of **1** explains the negligible luminescence: the population transfers out of the initial, optically bright, $^1Ni^{II}*$ state with a rate constant far larger than the radiative relaxation rate.

After the decay of the initial $^1Zn^{II}*$ excited state, the relaxation of **2** continues at longer timescales (see Fig. S38 and S39†). We assign these slower dynamics, as described in Table 1, to processes within a ligand-centered $^3Zn^{II}$ state. This triplet state decays on timescales of 580 ns and 1 μs, followed by formation of lower-amplitude signals that decay on timescales up to 140 μs. A possible explanation of the latter processes is ligand dissociation and finally non-geminate re-association; unlike **1**, the Zn complex can coordinate a fifth ligand in the axial position.

In contrast to **2**, **1** displays substantial spectral dynamics over much of the sub-ns range—also after the initial ∼1 ps decay phase. The complexity of the spectral time-evolution clearly demonstrates that the $^1Ni^{II}*$ state relaxes *via* multiple distinct intermediates before the ground state is recovered. This complexity contrasts with the essentially two-state relaxation dynamics observed for bipyridyl (bpy) based Ni^{II} photocatalysts.[33]

To shed light on these dynamics, we show the transient spectra of **1** at selected delay times in Fig. 3c. As the spectra demonstrate significant time-dependent changes in the excited states, we have subtracted the ground state bleach contribution
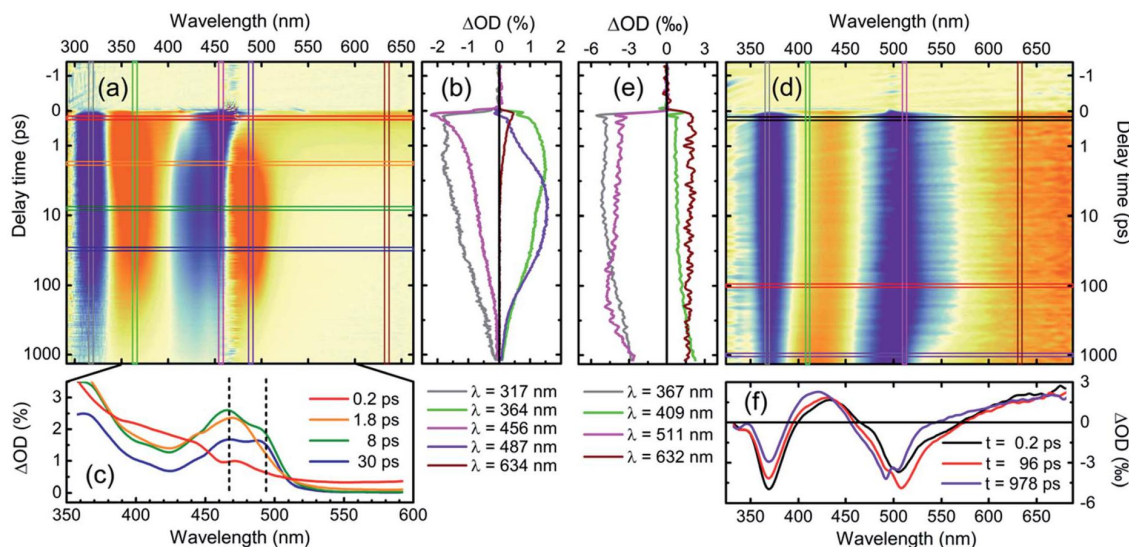
Fig. 3 (a) and (d) Transient absorption data of **1** and **2** in degassed 1 : 1 MeCN : THF after excitation at 460 nm (70 fs pulse) and 493 nm (49 fs pulse), respectively. Red-hued colors denote increased absorption due to, *e.g.*, excited absorption or product absorption, blue-hued colors denote decreased absorption due to, *e.g.*, ground state bleach or stimulated emission. (b) and (e) Kinetic traces extracted along the areas marked by the vertical lines. (c) and (f) Transient spectra extracted at selected probe-delays according to the horizontal lines. Note that in (c), the ground state bleach was subtracted for clarity (see text for details), while the cuts in (f) were unaltered. The ESA features marked by the vertical dashed lines in (c) are discussed in detail in the text.

Table 1 Summary of the dynamics observed for **1** and **2** in the transient spectroscopy[a]

	Assignment
1 (Ni[II])	
0.37 ps	Solvation dynamics
1.1 ps	^{1}Ni[II]* → MC/CT
2.5 ps	MC/CT → MC
14 ps	Spectral narrowing, *e.g.*, vibrational relaxation
81 ps	Combined MC → GS and MC → MC/CT
772 ps	MC/CT → ground state (GS)
2 (Zn[II])	
2 ps	Solvation dynamics
62 ps	Geometric relaxation
1.1 ns[b]	SE loss/^{1}Zn[II]* → ^{3}Zn[II]
580 ns	Relaxation within ^{3}Zn[II] manifold
1 µs	Decay of ligand-centered ^{3}Zn[II] state
5 µs	Ligand dissociation (tentative)
140 µs	Ligand re-association (tentative)

[a] Fit statistics, selected traces and residuals can be found in the ESI, Fig. S66, S67 and Table S11. [b] Time constant determined from fluorescence decay. The same constant as determined from the fs–ps TA measurements is 770 ps with a large error, since this is close to the full scanning range. For the ns–µs experiment a value of 1.5 ns is obtained, shorter than the 2.7 ns excitation pulse.

using a published weighting procedure[37,38] to clearly illustrate these changes. As such, these spectra directly show the time-evolution of the excited-state absorption spectra, distorted only at early times by the stimulated emission contribution.

The excited-state spectrum we observe at the earliest times (Fig. 3c, red trace, 0.2 ps) is, as noted above, typical for locally excited organic molecules—with a largely featureless photo-induced absorption extending into the near-infrared (NIR). Over the next ten ps, well-defined spectral structures emerge. Two features of particular interest are highlighted with vertical dashed lines in Fig. 3c: First, a relatively narrow ESA feature appears at approximately 465 nm concomitant with the decay of the ligand-localized ^{1}Ni[II]* state. This is followed by the emergence of a feature at 490 nm. Accordingly, kinetic traces from the main ESA bands at 487 and 364 nm, which capture both of these contributions (Fig. 3b, violet and green traces), are relatively complex; an indication of the formation and decay of several distinct spectral species. Such dynamics—fast decay of SE and broad ESA features, followed by well-defined ESA bands slightly red-shifted relative to the absorption spectrum—are often seen in association with energy-transfer from optically bright ligand-localized states to dark metal-centered states in open d-shell transition metal complexes (exemplified, *e.g.*, by the photoinduced dynamics of nickel porphyrin).[39,40] The time-evolution of the spectra here shows, however, that this transition from ligand-localized to metal-centered states involves at least one short-lived intermediate state.

Global kinetic analysis. A more complete picture of the spectral evolution of **1**, and thus the overall relaxation dynamics, requires global analysis of the whole dataset. In order to ensure maximal reliability of the extracted model, we performed two independent analyses: a model independent maximum entropy analysis (Fig. S34†),[41,42] as well as singular-value decomposition followed by a global fit to a sum-of-exponentials model.[43] We find good agreement of timescales from both approaches, implying good consistency of the extracted physical model. In agreement with the complex

dynamics suggested by the single-wavelength kinetic traces, we find that six components are necessary to describe the observed spectra within an exponential decay model.

The wavelength-dependence of this multi-component fit is best represented by the spectra associated with the decay components. The two most common representations of these "global" spectra are the Decay Associated Spectra (DAS) and the Evolutionary Associated difference Spectra (EAS), where the former is simply a plot of the amplitude of each decay component as a function of wavelength, and the model can be interpreted as representing the parallel decay of six independent species. In the EAS model, we rather assume a strictly sequential organization of compartments—or "states" (not necessarily electronic eigenstates of the system)—and the time-constants refer to the (unidirectional) population transfer between these. Hence, the EAS can be considered the spectra of these individual "states". In Fig. 4 we plot the DAS and EAS corresponding to the decay-component of **1**. The corresponding global component spectra for **2** can be found in Fig. S41.† The effective picture emerging from the analysis of these global spectra is summarized in Table 1 and depicted in Fig. 6.

At early times, the dynamics are dominated by components with characteristic times of 370 fs and 1.1 ps (Fig. 4, top). The faster component can be assigned to solvation, as it occurs with

the average solvation times of the two pure solvents.[44] The 1.1 ps spectra on the other hand prominently contain the decay of the SE contribution as well as the appearance of a characteristic ESA feature close to the excitation wavelength. Thus, these spectral dynamics reveal the transfer of the initially excited ligand-localized $^1Ni^{II}*$ state to states that are optically dark from the ground state.

This energy-transfer step is accompanied by the (quasi-) ground state recovery of the Mabiq ligand: *i.e.*, after this initial relaxation phase, the excited population resides almost completely on the metal center, while the ligand is in a ground state distorted by the excited metal center. Consequently, we can assign the spectra of the intermediate time components (14 and 81 ps lifetimes. Fig. 4, central panels) to transitions of ligand-localized $\pi–\pi*$ character. The 14 ps component is primarily associated with spectral narrowing—as demonstrated by the second-derivative profile of the DAS and slightly broadened EAS spectral profile—which suggests vibrational cooling[45] or heat dissipation.[46]

Interestingly, the fast appearance and subsequent decay of a 465 nm feature highlighted with a vertical dashed line in Fig. 3c is clearly mirrored in the global analysis: immediately after the $^1Ni^{II}*$ decay, the transient spectrum in Fig. 3 takes on a shape similar to—although strongly distorted—the 81 ps EAS. The global analysis captures this behaviour as a corresponding EAS with 1.1 ps growth and 2.5 ps decay (Fig. 4, bottom panel). The presence of a short-lived intermediate in the ligand → MC transfer demonstrated by this component is by itself interesting; in addition, we find that a state with an essentially identical spectrum re-emerges at long times as the MC states decay. This state subsequently decays on a much longer timescale, with a time constant of approximately 770 ps.

While short-lived intermediates as observed here can be assigned to, *e.g.*, vibrational cooling, we stress that the re-emergence of long-lived states with essentially identical spectral characteristics—as shown by the strong resemblance between the 2.5 ps and 770 ps EAS—makes such an assignment here highly implausible.

Earlier studies on macrocyclic nickel systems instead point to contributions from charge-transfer (CT) states in the electronic structure—both indirectly through the relaxation rate dependency on solvent polarity,[39] and through spectroscopic signatures in ultrafast XANES experiments.[47] While a complete one-electron ligand-to-metal charge transfer in **1** is unlikely, as one would then expect to observe the Mabiq cation spectrum, we find admixture of states with CT character to the MC states to be plausible in the relatively polar solvent environment in these experiments. This contrasts with photocatalytically active Ni^{II}–bpy complexes, where the long-lived lowest energy states appear to be of purely d–d character.[33,48]

Comparing the profiles of the DAS spectra, we find that both the 80 ps component assigned to population of MC states and the 772 ps component clearly contain the GSB signature in the 400–460 nm range. In other words, the ground state of the complex recovers bi-exponentially, implying a branching in the relaxation pathway: only a fraction of the initial excited state population reaches the long-lived states with admixture of CT

Fig. 4 Decay associated- (DAS, left column) and evolutionary associated- (EAS, right column) decay spectra extracted from a global fit of the relaxation dynamics of **1**. DAS amplitudes are shown on absolute scale, while the EAS are normalized to their maximum for easier comparison of spectral shapes. The component spectra are organized to highlight similarities in EAS component spectra. The time-constants are component lifetimes extracted from the relaxation dynamics of **1**. SE contributions to the spectra are found only around the 460 nm excitation wavelength at the earliest two times.

states, while the remainder presumably relaxes directly from the fully metal-centered states.

We can compare the observed excited-state dynamics with those inferred from the photoreduction of **1**. The dependence of the reaction quantum yield on TEA concentration was determined in our previous study.[25] Based on analysis of the results using a standard diffusion model[49] and a diffusion-limited quenching rate typical of molecules comparable to our system ($\sim 10^{10}$ M^{-1} s^{-1}),[50] the lifetime of the reactive excited state is predicted to be between 580 and 900 ps. This is in excellent agreement with the measured lifetime of 770 ps, which indicates that the outer-sphere electron transfer (ET) process with TEA can occur from this mixed MC/CT state.

Electronic structure

To correlate the spectroscopic signals with the electronic states involved in the optical response of the complexes, we employed electronic structure calculations at the linear response time-dependent density functional theory (DFT) level. The TDDFT-derived energy level diagrams for **1** and **2** are shown in Fig. 5a (see also Fig. S42 and S43†). To highlight the electronic structure of the states—*i.e.*, the parts of the complexes involved in the photo-excitation and relaxation—we computed the electron density differences between the ground and excited states (the density differences; Fig. 5b, S44–S47†), the spin density distributions of the lowest energy triplet states (Fig. 5c), and performed a Mulliken population analysis (Table S5†).

Our interpretation that the absorption consists of π–π* singlet transitions between Mabiq localized states is supported by the TDDFT calculations. This is also consistent with the observation that the optically bright transitions for **1** and **2** are of similar character in both complexes, as well as in other

transition metal–Mabiq complexes.[27–29] The calculated excitation energies of **1** and **2** are of similar magnitude (Fig. 5a; **1**: 2.85 eV S$_0$ → S$_4$; **2**: 2.77 eV S$_0$ → S$_1$), and the density differences associated with these transitions (Fig. 5b; corresponding natural transition orbitals (NTO) in Fig. S48†) demonstrate ligand-localized motion of charge. Similar vertical excitation energies are also obtained at the second-order correlated (ADC(2)/TZVP) level (Table S4†).

The DFT results also suggest an explanation for the experimentally observed differences in the relaxation dynamics of the two complexes. The spin densities of the ^{3}Zn^{II} triplet excited states (Fig. 5c) show that the excitation remains on the ligand, regardless of spin state, upon excited-state relaxation of **2**. The minimal contribution of MC states to the electronic structure and dynamics again suggests that **2** can be considered as an organic chromophore (*i.e.*, Mabiq) confined to a limited conformational range by the coordinating Zn^{2+} ion. The $\sim$1 ns intersystem crossing to the Mabiq triplet state is reasonable for an organic chromophore with an associated metal.

The structure and relaxation effects of **1** contrast with this simple behaviour. The ^{1}Ni^{II}*–^{3}Ni^{II}* energy gap is substantially larger than the corresponding singlet-triplet energy difference of **2**. While the electronic structure of the ^{1}Zn^{II}* and ^{3}Zn^{II} states are both predominantly ligand-localized, the corresponding ^{1}Ni^{II}* and ^{3}Ni^{II} states are clearly different (Fig. 5b and c), with a ^{3}Ni^{II} state that is essentially metal-centered. Thus, the computational data suggest that intersystem crossing in **1** involves energy transfer from the Mabiq ligand to the metal center, in agreement with our experimental observations. A large number of additional states are located between the ground and the optically bright ^{1}Ni^{II}* state, many of which are also metal-centered, of both singlet and triplet character. The
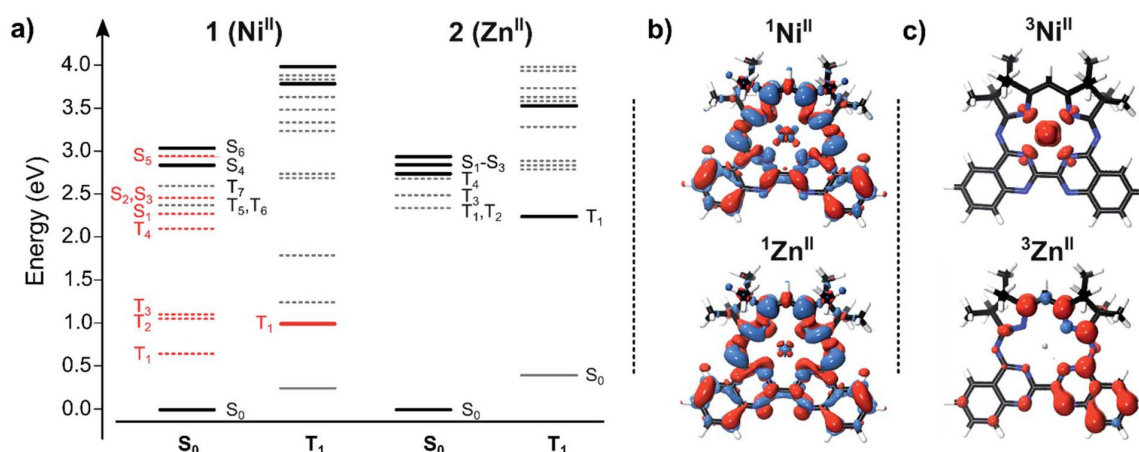
Fig. 5 (a) Vertical excitation energies (VEEs) derived at the TDDFT/B3LYP level for **1** and **2** at the optimized singlet (S$_0$) and lowest energy triplet (T$_1$) geometries. Optically allowed states are shown with solid lines, optically dark states are denoted by dashed lines; MC states are shown in red, and ligand-centered states in black. Note that the lowest energy optically allowed state in **1** is the ligand-centered S$_4$ state, whereas in **2** the lowest optically active singlet is the ligand-centered S$_1$ state. (b) Total electron density difference upon photo-excitation into the lowest energy optically bright state for **1** (S$_4$, top) and **2** (S$_1$, bottom), with positive and negative differences between the excited and ground states marked in blue and red, respectively. The charge migration takes place almost exclusively on the ligand for both species. (c) Spin density ($\alpha - \beta$) for the lowest energy triplet state of **1** (top) and **2** (bottom), with positive and negative differences between alpha and beta spin densities marked in red and blue, respectively. Note that the excess spin is almost entirely metal localized for **1**, while it is distributed on the ligand for **2**.

large number of states facilitates the observed rapid ligand-to-metal energy transfer. A similar electronic picture is also obtained at the TDDFT/CAM-B3LYP level (Fig. S43†), suggesting that the results are robust and do not arise from, *e.g.*, DFT charge transfer problems. The calculations also suggest that spin–orbit coupling (SOC) effects are small for the Zn–Mabiq complex, but could contribute into transition between singlet and triplet states for Ni–Mabiq (Fig. S49†).

The implicit assumption that intersystem crossing is an efficient quenching channel for the ^{1}Ni^{II}* state is well-founded, given the typical behaviour of open-shell transition metals.[21] The optical spectra themselves only reveal that the final state in the relaxation cascade is (i) optically dark from the ground state (at least in the UV/Vis spectral region), and (ii) has a prominent ESA band slightly redshifted from, but close in energy to, the (^{1}Ni^{II} → ^{1}Ni^{II}*) ground state absorption band. In this regard, the calculations support our expectation of relaxation *via* metal centered states. All MC transitions with energies in the range of the TA measurements, either from the singlet ground state or from the triplet state, are dark; any optically active transitions primarily involve the Mabiq ligand.

With the assignment of triplet character to the low-lying energy levels of **1** and **2**, we can reconcile and at least semi-quantitatively explain the photoreduction quantum yields and the time constants from the TA measurements. The quantum yield, QY, of the photoinduced reduction of the M–Mabiq catalysts by Et$_3$N is given by:

$$QY = \frac{k_{red}}{k_{tot}}$$

with the effective quenching rate, k_{red}, and the total relaxation rate, k_{tot}, as determined from the TA measurements. With a QY of 2.9×10^{-4} for Ni–Mabiq and $k_{tot} = 1/772$ ps, we obtain a surprisingly long quenching time of $t = 1/k_{red} = 2.7$ μs. The low QY is therefore the consequence of a low electron transfer rate and the rapid decay of the excited **1**. Using the same value of k_{red} as a first guess for **2**, we predict a total decay time of 10 μs, which is well within the range of the slow time constants obtained from the TA data for the Zn complex. In summary, the reduction is rather slow, and the QY is limited by the lifetime of the triplet states.

Catalysis

Given the distinctive photophysics, differing behaviour with respect to photoreduction, and activity toward O$_2$, we examined the comparative ability of **1** and **2** to act as a photoredox catalyst in a series of photo-driven reactions. The first of these is the previously reported cyclization of an *N*-(ω-bromoalkyl)-substituted indole (dimethyl 2-(3-(1*H*-indol-1-yl)propyl)-2-bromomalonate) by **1** (Table 2, top scheme; mechanism in Scheme S1†), which gave the product in high yield.[25] In this case, irradiation of the reaction mixture facilitates reduction of **1** by Et$_3$N, and the resultant **1**^{red} triggers the ring closing in a diffusive manner. A catalytic cycle for the formation of the cyclized indole should also be feasible using **2**, based on its redox properties alone. However, low product yields were

Table 2 Photoredox-catalysed cyclization of an *N*-(ω-bromoalkyl)-substituted indole (top), aza-Henry reaction (middle) and oxidative coupling of 4-methoxybenzylamine (bottom)

Entry	Catalyst	% yield[a]
1	1	86 ± 5 (13 h)
2	2	35 (13 h)

Entry	Catalyst	% yield[b] (time)
1	1	82 ± 7 (5 h)
2	1/without irradiation	—
3	None	14 ± 6 (5 h)
4	2	36 ± 13 (30 min)

Entry	Catalyst	% yield[c] (time)
1	1	27 ± 0 (17 h)
2	1/without irradiation	— (12 h)
3	None	— (12 h)
4	2	73 ± 12 (30 min)

[a] For details see ref. 25 and 50. [b] Yields are mean ± standard deviation of measurements performed at least in duplicate. Reactions were run on a 0.05 mmol scale. Product yields were determined by ^{1}H NMR using mesitylene as an internal standard. [c] For the oxidative coupling of benzylamine, ESI-MS was further used to confirm the presence of the desired product ([M + H]$^+$ $m/z = 256.09$).

obtained and degradation of the metal complex occurred, as evidenced by bleaching of the solution throughout the reaction.[51] Conversely, while the photoreduction quantum yield is relatively low, **1** is an effective photoredox catalyst, as it appears resistant to degradation and remains active throughout the extended reaction period.[25] In related preliminary work, we observed that the Fe^{II}–, Co^{II}– and Cu^{II}–Mabiq complexes all exhibit varying reaction yields and selectivities,[51] further demonstrating that the choice of metal center clearly influences the activity.

We next examined the photocatalytic ability of **1** and **2** in two reactions that do not rely on initial reduction of the catalyst by a sacrificial donor: the oxidative C–H functionalization of *N*-phenyl-tetrahydroisoquinoline (THIQ), and the oxidative coupling of 4-methoxybenzylamine (Table 2; see ESI† for details).

The THIQ functionalization represents a photoredox catalysed aza-Henry reaction (Table 2, middle scheme; mechanism in Scheme S2†).[52] In the initial step, reductive quenching of the excited state of the catalyst by the isoquinoline leads to formation of a cationic amine radical. As discussed above, this step is expected to proceed on the low μs timescale. The solvent nitromethane (CH_3NO_2) can serve to regenerate the catalyst, and facilitates iminium ion formation. The resultant reduced oxidant and amine cation radical will likely remain in close proximity due to the lack of time for diffusion; alternatively the reduced oxidant readily combines with CH_3NO_2 *via* a hopping process. Either way, catalyst reoxidation and iminium ion formation *via* a quasi-geminate step should be fast and efficient.

The final product of the aza-Henry reaction is generated upon addition of the nitromethane-derived CH_2NO_2 to the iminium. Thus, nitromethane also acts as the co-substrate. The aza-Henry reaction exploits the direct reaction of $M^{II}*$ with the substrate, unlike the previously examined indole cyclization, which reflected the interaction of a substrate with the reduced 'M^I'–Mabiq forms. The reaction also allowed us to probe the ability to regenerate the reduced catalyst forms in the presence of an oxidant, which would allow application of the Mabiq complexes in a broader range of chemistry.

The product yields obtained in the photoredox catalysed aza-Henry reaction by **1** and **2**, using nitromethane as the solvent, were 82% (**1**, after 5 h) and 36% (**2**, after 30 min). With the illumination power and total time, we can estimate a lower limit of the overall reaction quantum yield of 1.5×10^{-3}. The yields obtained for the Ni-complex are comparable to those reported using $[Ru(bpy)_2]^{2+}$ and $[Ir(ppy)_2(dtbbpy)]^+$.[52] Thus, **1** shows promise as an effective catalyst for such C–H functionalization reactions. The lower yields of **2** in the reaction are again due to degradation of the Zn-complex. A significant decrease in the absorption bands of **2** was already observed within the first 30 minutes reaction time (Fig. S55†). This contrasts with the behaviour of **1**, which remained intact throughout the reaction, as evidenced by both absorption and NMR spectroscopies (Fig. S56 and S57†). We note that irradiation of a solution of **1** and the isoquinoline in the absence of a suitable oxidant also leads to rapid decomposition of the Ni-complex (Fig. S58 and S59†), which we speculate is due to attack of **1^{red}** by the isoquinoline radical.

The final reaction that was examined, the oxidative coupling of 4-methoxybenzylamine (Table 2, bottom scheme), depends on the participation of O_2 in the catalytic cycle (Scheme S3†). Both energy transfer and photoredox mechanisms have been proposed for this reaction—in the latter case, O_2 would serve as an oxidant and to generate an imine intermediate.[53] The Ni–Mabiq complex was able to catalyse the coupling reaction, albeit with only 27% product yield even after 17 h. No significant amount of side product was detected. Nevertheless, **1** remained stable under these conditions (Fig. S60†). Using **2** as the photocatalyst, a larger amount of *N*-(4-methoxybenzyl)-1-(4-methoxyphenyl)methanimine was obtained (73% yield, 30 min). However, complete degradation of the Zn compound was again observed after 30 min (Fig. S61†).

To supplement the basic reactivity studies, we examined the ability of 4-methoxybenzylamine to photoreduce the Mabiq compounds—the first step in the photoredox pathway. Both **1** and **2** can be photoreduced using 4-methoxybenzylamine under inert atmosphere, indicating that an electron transfer pathway is feasible (Fig. S62 and S63†). However, after the initial formation of some **2^{red}** by the amine, the spectrum of the Zn-complex is further altered. Evaluation of the photoreduction data shows that the reduction of Ni$^{II}*$ by methoxybenzylamine is photo-reversible, with comparable quantum yield values for the forward and back electron transfer processes (*ca.* 1.7×10^{-5}; Fig. S62†). The low yield is consistent with the low coupling product yields obtained with **1**, even after 17 h. From the illumination conditions of 4-methoxybenzylamine with **1** we can estimate a lower limit of the overall reaction quantum yield of 4.3×10^{-4}. In comparison, for the quenching QY—taking into account the concentration of methoxybenzylamine under the reaction conditions (25 mM), and the linear dependence of the process on the quencher concentration[25]—we obtain a value of 8.5×10^{-4}. Within the uncertainty of this estimate the two yields are equal, showing that indeed all steps after the first ET occur with near unity.

The quenching of the photo-excited **2** is associated with QYs of 0.12 to the reduced form, and 0.20 to an unidentified side product, both of which rapidly convert further to some final species with an optical spectrum that is distinct from that of **2** or **2^{red}** (Fig. S63†). Clearly any accumulation of **2^{red}** also leads to degradation of the original form of the Zn catalyst. A slight shift in both the ^{1}H NMR resonances and absorption spectrum of **2** in the presence of the substrate is observed (Fig. S64 and S65†), which suggests that the ability of the amine to coordinate to the Zn may contribute to the activity and degradation of **2**. However, overall, the high reduction yields together with the ability of O_2 to reoxidize any accumulated **2^{red}** enables significant product formation before the catalyst is fully consumed.

While the above reactions are quite distinct, the photoredox catalytic activity of the M–Mabiq complexes in all of the reactions hinges on the ability of the excited states to engage in single electron transfer with a sacrificial donor or the substrate. Our model for the excited state relaxation pathways for **1** and **2**, based on spectroscopic characteristics and the calculated electronic structure, is summarized in Fig. 6. ET involving the singlet states is precluded by the short lifetimes—the close vicinity of the resulting ion pair also would likely lead to a rapid back-ET and therefore be unproductive. Single electron transfer between the amine substrates and M–Mabiq will occur *via* the triplet states, where back ET is consequently blocked by the Pauli principle.[54] In the Zn-containing **2**, all relevant excited states, including the triplet states, are ligand-localized. As a result, photoreduction results in formation of what is essentially a Mabiq radical anion coordinated by a Zn^{II}; decomposition proceeds as is typical for organic radical ions. The longer excited state lifetime of **2** should favor catalytic activity, but the instability of **2** hinders its use as a photoredox catalyst. Oxidants, as used in the light-driven aza-Henry and oxidative coupling reactions, regenerate **2** to some degree. However, even in the presence of excess oxidant the degradation
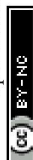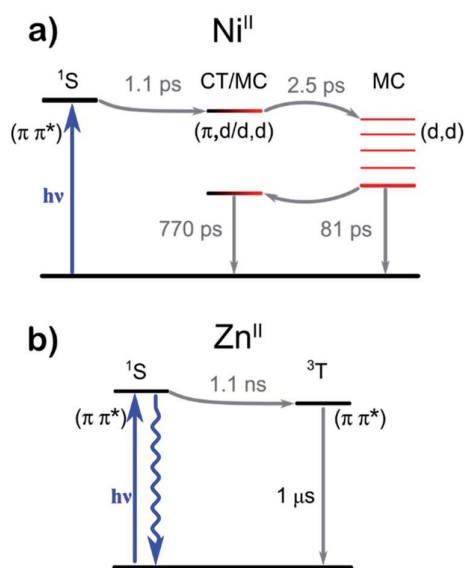
Fig. 6 Effective relaxation model of the compounds **1** (a) and **2** (b) as extracted from the time-resolved absorption data. Components assigned to solvation and vibrational cooling omitted for clarity. Metal-centered states are depicted in red; ligand-centered states are indicated in black.

of 2^{red} appears to outcompete its reoxidation. In contrast, the initial ligand-centered excited state of **1** relaxes rapidly towards states of metal-centered and partial CT character. The involvement of metal-centered states in 1^{red} appears to make this complex more robust, further highlighting the synergy between the metal and redox-active ligand.

Our preliminary studies with alternate electron donors and select substrates demonstrate, however, that the nature of the donor is crucial. Electron transfer between **1** and either DMA or 4-methoxybenzylamine was sluggish; in the latter case this significantly limited the catalysis. Moreover, the isoquinoline radical can destroy the complex if subsequent transformations of the intermediate are not fast enough (Fig. S58 and S59†). More detailed studies will be required to determine the specific donor/M–Mabiq interactions and their importance in the mechanism of excited state electron transfer. Finally, the generally greater stability of 1^{red} allows this species to be more effectively regenerated by oxidants, allowing **1** to engage in various stages of a photoredox cycle.

The $^3Zn^{II}*$ state of the Zn complex may be more suited for select energy transfer reactions, as for singlet O_2 sensitization. With respect to singlet-oxygen sensitization, the $(^1Ni^{II}-^3Ni^{II})$ energy gap is much smaller than the $(^3O_2-^1O_2)$ energy gap, and consequentially the process is energetically disfavored. Thus, **1** may be less effective for energy transfer processes.

Overview of photodynamics

It is worth comparing the photophysics of our Mabiq complexes to that of M-bpy based compounds. The bpy ligand is essential to the functionality of $[Ru(bpy)_3]^{2+}$, whose underlying photophysical properties have been studied in great depth.[17] Excitation of $[Ru(bpy)_3]^{2+}$ in the visible region leads to population of long-lived ^3MLCT excited states, which subsequently engage in single electron transfer. The sub-ps excited state lifetimes of the ^3MLCT states of $[Fe(bpy)_3]^{2+}$ on the other hand can be attributed to relaxation to MC states, which in contrast to those of the Ru complex lie below the MLCT states.[55] This altered ordering reflects the general problem of first row transition metal complexes, where low lying d–d states lead to short excited state lifetimes and limit the photoredox capacity of the compounds. A notable exception is the behavior of the other class of Ni^{II} photoredox catalysts ($^{tBu}bpy)Ni^{II}(Ar)(X)$; X = halide or OR^-, also based on the bpy ligand.[33,48,56] The low-lying $^3d–d$ states are not only long lived, but allow this complex to undergo photoinduced Ni–aryl bond homolysis.

The Mabiq ligand likewise contains a bipyridine-like moiety—as well as a second redox-active functionality in the diketiminate. The presence of multiple redox-active units in the macrocyclic M–Mabiq systems results in photophysics that are more complex than the bipyridyl systems, with ligand-centered, CT and MC character all involved (Fig. 6). The initially accessed ligand-centered π–π* state of **2** can also engage in single electron transfer, whereas the CT and MC states become more relevant for **1**. Our findings suggest that these latter states lie closer in energy than what is observed in bpy-based compounds. Interactions between CT, MC, and π–π* states account for the complex photodynamics of **1**, and further underscores the synergy between the redox-active ligand and the metal centers. The nature of the bound metal center may alter the relative energies of these CT and MC states. For the Fe, Co and Cu complexes, which possess additional axial ligands, the d–d states might also enable M–L bond homolysis. Overall, the unique features of the Mabiq ligand allow for rich and varied photochemistry.

Conclusions

The nature of the coordinated metal ion clearly has a significant influence on the photophysical properties and reactivity of the Mabiq complexes, as exemplified by the Ni and Zn complexes **1** and **2**. Our findings unravel contributions of the various ligand-centered, charge transfer and MC states, and provide initial insight into how the interactions between the metal and redox-active ligands influence activity and stability of photoredox catalysts. With the exception of the Zn complex, the chemical stability of the M–Mabiq series is a notable feature of this class of photocatalysts. Light-driven access to the reduced, stable forms of M^{II}–Mabiq complexes containing Fe → Cu may also permit more diverse organic transformations.

In our system, the Mabiq system scaffold provides a highly unique degree of freedom in a second metal binding site at the complex periphery. Incorporation of a second metal ion may enable alterations to the electronic structure of the core metal complex, while circumventing the need to modify the ligand backbone. As such, the second coordination site may have an influence on stability and electron transfer efficiencies. The photochemical properties of a series of bimetallic Mabiq

50

compounds can be systematically studied. The second coordination site also opens up entirely new possibilities for bifunctional photoredox catalysis. Overall, we believe the properties of the Mabiq system will allow these complexes to become valuable additions to the growing repertoire of earth-abundant photoredox catalysts.

Author contributions

RL carried out synthesis and characterization of compounds, and performed photoreduction experiments. RL & HD performed data analysis for photoreduction experiments. OZE performed photocatalytic addition- and coupling-reactions. RL, HD, and MB performed the time-resolved optical experiments. SLM and VRIK designed and performed the DFT calculations. RL, SLM, HD and OZE made comparable and substantial contributions to experiments and analysis. AJR carried out additional DFT calculations. CJ was responsible for X-ray crystallography. ER, ET, JH, and CRH planned, designed, and analyzed the experiments. CRH and ET conceived the project and wrote the paper with contributions from all authors.

Conflicts of interest

There are no conflicts to declare.

Acknowledgements

Notes and references

§ In our previous studies, we have shown that all of the previously isolated, formal M^I–Mabiq complexes are best described by $[M^{II}(Mabiq^{\cdot})]$, containing the reduced Mabiq radical, rather than a monovalent metal center.

1 C. K. Prier, D. A. Rankic and D. W. C. MacMillan, *Chem. Rev.*, 2013, **113**, 5322–5363.

2 M. H. Shaw, J. Twilton and D. W. C. MacMillan, *J. Org. Chem.*, 2016, **81**, 6898–6926.

3 D. M. Schultz and T. P. Yoon, *Science*, 2014, **343**, 1239176.

4 L. Marzo, S. K. Pagire, O. Reiser and B. König, *Angew. Chem., Int. Ed.*, 2018, **57**, 10034–10072.

5 C. R. J. Stephenson, D. W. C. MacMillan and T. P. Yoon, *Visible light photocatalysis in organic chemistry*, Wiley-VCH Verlag GmbH & Co., Weinheim, Germany, 2018.

6 J. M. R. Narayanam and C. R. J. Stephenson, *Chem. Soc. Rev.*, 2011, **40**, 102–113.

7 Y. Xi, H. Yi and A. Lei, *Org. Biomol. Chem.*, 2013, **11**, 2387–2403.

8 *Chemical Photocatalysis*, ed. B. König, De Gruyter, Berlin, 2013.

9 L. Hammarstrom, *Acc. Chem. Res.*, 2015, **48**, 840–850.

10 D. L. Ashford, M. K. Gish, A. K. Vannucci, M. K. Brennaman, J. L. Templeton, J. M. Papanikolas and T. J. Meyer, *Chem. Rev.*, 2015, **115**, 13006–13049.

11 S. Berardi, S. Drouet, L. Francas, C. Gimbert-Surinach, M. Guttentag, C. Richmond, T. Stoll and A. Llobet, *Chem. Soc. Rev.*, 2014, **43**, 7501–7519.

12 S. Archer and J. A. Weinstein, *Coord. Chem. Rev.*, 2012, **256**, 2530–2561.

13 M. K. Brennaman, R. J. Dillon, L. Alibabaei, M. K. Gish, C. J. Dares, D. L. Ashford, R. L. House, G. J. Meyer, J. M. Papanikolas and T. J. Meyer, *J. Am. Chem. Soc.*, 2016, **138**, 13085–13102.

14 J. A. Terrett, J. D. Cuthbertson, V. W. Shurtleff and D. W. C. MacMillan, *Nature*, 2015, **524**, 330–334.

15 J. Twilton, C. Le, P. Zhang, M. H. Shaw, R. W. Evans and D. W. C. MacMillan, *Nat. Rev. Chem.*, 2017, **1**, 0052.

16 K. L. Skubi, T. R. Blum and T. P. Yoon, *Chem. Rev.*, 2016, **116**, 10035–10074.

17 D. M. Arias-Rotondo and J. K. McCusker, *Chem. Soc. Rev.*, 2016, **45**, 5803–5820.

18 J. W. Tucker and C. R. J. Stephenson, *J. Org. Chem.*, 2012, **77**, 1617–1622.

19 T. Koike and M. Akita, *Inorg. Chem. Front.*, 2014, **1**, 562–576.

20 M. C. Carey, S. L. Adelman and J. K. McCusker, *Chem. Sci.*, 2019, **10**, 134–144.

21 C. B. Larsen and O. S. Wenger, *Chem.–Eur. J.*, 2018, **24**, 2039–2058.

22 O. S. Wenger, *J. Am. Chem. Soc.*, 2018, **140**, 13522–13533.

23 A. Hossain, A. Bhattacharyya and O. Reiser, *Science*, 2019, **364**, eaav9713.

24 L. Traub and O. Reiser, *Phys. Sci. Rev.*, 2019, **4**, 20170172.

25 M. Grübel, I. Bosque, P. J. Altmann, T. Bach and C. R. Hess, *Chem. Sci.*, 2018, **9**, 3313–3317.

26 H. S. Stark, P. J. Altmann, S. Sproules and C. R. Hess, *Inorg. Chem.*, 2018, **57**, 6401–6409.

27 P. Banerjee, A. Company, T. Weyhermuller, E. Bill and C. R. Hess, *Inorg. Chem.*, 2009, **48**, 2944–2955.

28 E. Müller, G. Bernardinelli and A. von Zelewsky, *Inorg. Chem.*, 1988, **27**, 4645–4651.

29 E. V. Puttock, P. Banerjee, M. Kaspar, L. Drennen, D. S. Yufit, E. Bill, S. Sproules and C. R. Hess, *Inorg. Chem.*, 2015, **54**, 5864–5873.

30 L. M. Moreira, F. V. d. Santos, J. P. Lyon, M. Maftoum-Costa, C. Pacheco-Soares and N. S. d. Silva, *Aust. J. Chem.*, 2008, **61**, 741–754.

31 G. Linden, L. Zhang, F. Pieck, U. Linne, D. Kosenkov, R. Tonner and O. Vazquez, *Angew. Chem., Int. Ed.*, 2019, **58**, 12868–12873.

32 P. M. Antoni, A. Naik, I. Albert, R. Rubbiani, S. Gupta, P. Ruiz-Sanchez, P. Munikorn, J. M. Mateos, V. Luginbuehl, P. Thamyongkit, U. Ziegler, G. Gasser,

51

G. Jeschke and B. Spingler, *Chem.–Eur. J.*, 2015, **21**, 1179–1183.

33 S. I. Ting, S. Garakyaraghi, C. M. Taliaferro, B. J. Shields, G. D. Scholes, F. N. Castellano and A. G. Doyle, *J. Am. Chem. Soc.*, 2020, **142**, 5800–5810.

34 S. Saeedi and T. A. White, *ACS Appl. Energy Mater.*, 2020, **3**, 56–65.

35 U. Megerle, I. Pugliesi, C. Schriever, C. F. Sailer and E. Riedle, *Appl. Phys. B*, 2009, **96**, 215–231.

36 E. Riedle, M. Bradler, M. Wenninger, C. F. Sailer and I. Pugliesi, *Faraday Discuss.*, 2013, **163**, 139–158.

37 R. Wilcken, M. Schildhauer, F. Rott, L. A. Huber, M. Guentner, S. Thumser, K. Hoffmann, S. Oesterling, R. de Vivie-Riedle, E. Riedle and H. Dube, *J. Am. Chem. Soc.*, 2018, **140**, 5311–5318.

38 S. A. Kovalenko, R. Schanz, H. Hennig and N. P. Ernsting, *J. Chem. Phys.*, 2001, **115**, 3256–3273.

39 A. V. Zamyatin, A. V. Soldatova and M. A. J. Rodgers, *Inorg. Chim. Acta*, 2007, **360**, 857–868.

40 J. L. Retsek, C. M. Drain, C. Kirmaier, D. J. Nurco, C. J. Medforth, K. M. Smith, I. V. Sazanovich, V. S. Chirvony, J. Fajer and D. Holten, *J. Am. Chem. Soc.*, 2003, **125**, 9787–9800.

41 R.-J. Kutta, T. Langenbacher, U. Kensy and B. Dick, *Appl. Phys. B*, 2013, **111**, 203–216.

42 P. Kölle, I. Pugliesi, H. Langhals, R. Wilcken, A. J. Esterbauer, R. de Vivie-Riedle and E. Riedle, *Phys. Chem. Chem. Phys.*, 2015, **17**, 25061–25072.

43 I. H. M. van Stokkum, D. S. Larsen and R. van Grondelle, *Biochim. Biophys. Acta, Bioenerg.*, 2004, **1657**, 82–104.

44 M. L. Horng, J. A. Gardecki, A. Papazyan and M. Maroncelli, *J. Phys. Chem.*, 1995, **99**, 17311–17337.

45 V. Balevicius Jr, T. Wei, D. Di Tommaso, D. Abramavicius, J. Hauer, T. Polivka and C. D. P. Duffy, *Chem. Sci.*, 2019, **10**, 4792–4804.

46 Y. Mizutani, Y. Uesugi and T. Kitagawa, *J. Chem. Phys.*, 1999, **111**, 8950–8962.

47 M. L. Shelby, P. J. Lestrange, N. E. Jackson, K. Haldrup, M. W. Mara, A. B. Stickrath, D. Zhu, H. T. Lemke, M. Chollet, B. M. Hoffman, X. Li and L. X. Chen, *J. Am. Chem. Soc.*, 2016, **138**, 8752–8764.

48 E. R. Welin, C. Le, D. M. Arias-Rotondo, J. K. McCusker and D. W. C. MacMillan, *Science*, 2017, **355**, 380–385.

49 Y. Kaneko, Y. Nishimura, T. Arai, H. Sakuragi, K. Tokumaru and D. Matsunaga, *J. Photochem. Photobiol., A*, 1995, **89**, 37–44.

50 M. Montalti, A. Credi, L. Prodi and M. T. Gandolfi, *Handbook of Photochemistry*, Taylor & Francis Group, LLC, Boca Raton, Florida USA, 3rd edn, 2006.

51 M. Grübel, PhD, Chemistry, PhD dissertation, Technical University Munich, 2019, DOI: 10.14459/2020md1515118.

52 A. G. Condie, J. C. González-Gómez and C. R. Stephenson, *J. Am. Chem. Soc.*, 2010, **132**, 1464–1465.

53 J. A. Johnson, J. Luo, X. Zhang, Y.-S. Chen, M. D. Morton, E. Echevería, F. E. Torres and J. Zhang, *ACS Catal.*, 2015, **5**, 5283–5291.

54 U. Megerle, M. Wenninger, R.-J. Kutta, R. Lechner, B. König, B. Dick and E. Riedle, *Phys. Chem. Chem. Phys.*, 2011, **13**, 8869–8880.

55 J. K. McCusker, *Science*, 2019, **363**, 484–488.

56 B. J. Shields, B. Kudisch, G. D. Scholes and A. G. Doyle, *J. Am. Chem. Soc.*, 2018, **140**, 3035–3039.

52

Chapter 4

Unpublished Results

Visible light induced and Co(Mabiq)-catalyzed acylation of styrenes

4.1 Introduction

Organocobalt complexes are utilized as efficient sources of C-centered radicals due to the low BDEs of the Co–C bonds which ranges from 14 – 45 kcal mol^{-1}.[1] Radical generation from these compounds can be initiated either by heat or light and have been predominantly employed in polymerization reactions.[2] The reversibility of the Co–C bond cleavage also makes these compounds attractive sources of radicals as this reversibility reduces the concentration of free radicals, thus reducing the possibility of free-radical initiated reactions. Organocobalt(III) intermediates generated in situ have therefore been used as sources of C-centered radicals in cobalt catalyzed dimerization, polymerization,[2] dehalogenation,[3] alkylation, and acylation reactions.[4] The generation of organocobalt(III) compounds usually involves the addition of the supernucleophilic Co(I)-intermediate across carbon-halide or pseudohalide bonds in alkyl and acid halides. The accessibility of the supernucleophilic Co(I)-intermediate either chemically or photochemically makes these compounds attractive for generation of C-centered radicals. The commonly used Co-complexes are cobalamins (vitamin B$_{12}$), Co-salens, Co-porphyrins and cobaloximes.[1a, 4a, 4b, 4d]

Acylcobalt(III) complexes are utilized as sources of nucleophilic acyl radicals upon exposure of the compounds to heat or light. These compounds upon generation of the acyl radicals also furnish the metalloradical Co(II)-intermediates which can further engage the generated radicals to reduce free-radical reactions or in the presence of alkyl radicals engage in dehydrocobaltation reactions to generate alkenes.[3, 5] The use of Co-complexes for generation of acyl radicals provides a mild route compared to the use of acids and other harsh conditions. Photocatalytic methods have also been reported in the literature and these involves the use of photocatalysts of precious metals such as Ir and Ru,[6] organocatalyst,[7] and HAT-catalysts such as decatungstate,[8] N-hydroxyphthalimide,[9] and FeCl$_3$ as Cl-HAT source in combination with a photosensitizer.[10]

With regards to transformations in which acylcobalt(III)-compounds were used to generate acyl radicals and functionalize alkenes, only a few reports are available in the literature. In one of the reports, Pattenden and co-workers utilized stoichiometric amounts of acyl-cobalt salophen reagents for the generation of acyl radicals under light irradiation. Reaction of the radicals with electron-deficient alkenes furnished mixtures of saturated and unsaturated ketones **(Scheme 1A)**.[11] In another report, Gryko and co-workers utilized vitamin B$_{12}$ as catalyst in the photo-assisted generation of acyl radicals from acyl-thioesters. The acyl radical intermediates only reacted with electron-deficient alkenes and saturated ketones were formed as the sole products. The catalytic system also required stoichiometric amounts of Zn as reductant, and as a result, commercially available acid halides could not be directly used as acid radical precursors **(Scheme 1B)**.[12]

A. Photogeneration of acyl radicals from acylCo-salophen reagents.

R = alkyl and acyl; EWG = electron-withdrawing group.

B. Vit. B$_{12}$-photocatalyzed acyl radical generation from acylpyridylthioesters.

R = alkyl and acyl; EWG = electron-withdrawing group.
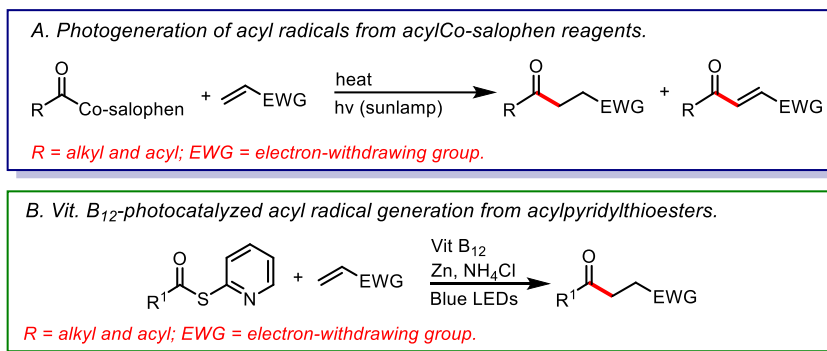
Scheme 1. Generation of acyl radicals from organocobalt(III)-complexes.

Mechanistically, the generation of alkyl or acyl radicals from organocobalt(III) complexes upon irradiation involves an LMCT event which then leads to homolytic cleavage of the Co–C bond. This light-activation pathway for substrates usually involves first the oxidative addition of Co(I)-species to suitable organohalides or pseudohalides and is known as visible light induced homolysis (VLIH).[1b, 11-12] This is an alternative pathway for substrate activation that is different from intermolecular SET or EnT processes. Generally, VLIH is predominant in photoactive 3d-metal complexes and thus makes the development of catalysts based on these earth-abundant transition metals attractive for photoinduced cross-coupling reactions.[13]

4.2 Reaction Development

Our investigations into the photocatalytic activities of metal-Mabiq complexes have recently led to the development of a Markovnikov-selective Co-Mabiq photocatalyzed alkylation of indoles and indazoles with styrenes.[14] Following this report, we wished to further explore the catalytic ability of Co-Mabiq complexes, this time, as direct sources of C–centered or halide radicals for HAT or functionalization of alkenes. We had recently observed that the *Co^{II}(Mabiq•) (formally denoted as Co^{I}(Mabiq))* **1** compound which can be generated chemically via the one-electron reduction of Co^{II}(Mabiq)Cl **2** with cobaltocene can also be photogenerated in the presence of a sacrificial electron donor (Figure 1A). Furthermore, we had already established that the trivalent Co(Mabiq)Cl$_2$ is photoactive and undergoes VLIH of the Co–Cl bond in the absence of a sacrificial electron donor to furnish Cl radical and metalloradical divalent Co(Mabiq)Cl **2**.[14] With these observations, we hypothesized that oxidative addition of Co(Mabiq) to organohalide bonds should generate an organocobalt(III)-Mabiq compound which might also be photoactive and would undergo VLIH to release C–centered or halide radical. The C-centered or halide radical could then be subsequently employed as HAT-catalyst or for functionalization of alkenes. Finally, the reduction of the ensuing metalloradical Co^{II}-species in the presence of a sacrificial electron donor should replenish the Co^{I}(Mabiq) intermediate (Figure 1B).
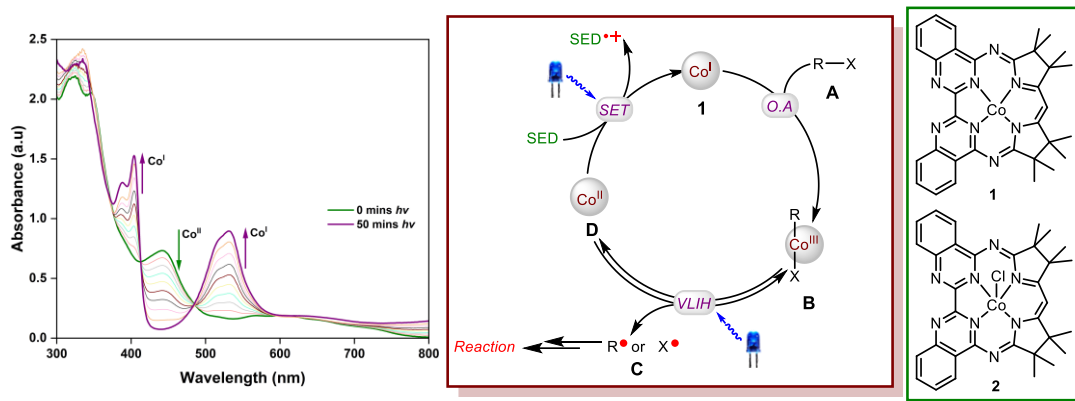
Figure 1. (A) Spectral evolution during irradiation of a solution of **2** (50 μM) in the presence of Et$_3$N (25 mM, 500 equiv.) in MeCN/THF (1:1). Green trace: spectrum prior to irradiation. Purple trace: final spectrum obtained after irradiation of the solution with blue LED (455 nm, P$_{ref}$: 364 mW, φ = 1.95 × 10^{-4}). (B) Mechanistic hypothesis.

Based on the mechanistic hypothesis, a THF solution of chemically synthesized **1** was added to different organohalide solutions and the UV Vis spectra and ESI MS of the different solutions were taken. The results revealed the formation of new organocobalt species in some of the solutions (Figure 2). With these results, we then set up reactions with the organohalides which formed new Co-Mabiq species and irradiated the solutions with added styrene. The reaction containing 2 mol% of **1**, 4-methoxystyrene **3a** (0.2 mmol, 1 equiv.) and benzoyl chloride **4a** (0.2 mmol, 1 equiv.) in THF (2 mL) with blue LED (455 – 460 nm) irradiation under argon for 24 h at 25 °C afforded the chalcone **5aa** in 10% yield as the sole product (Table 1, entry 2; also see Table S1).
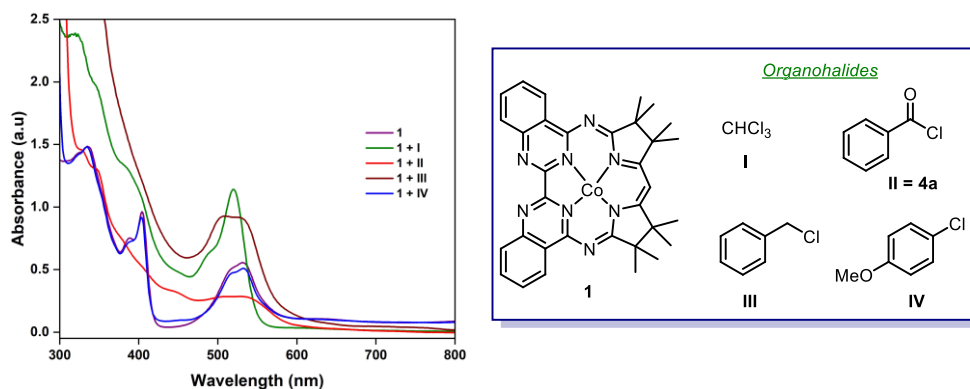
Figure 2. Comparison of UV Vis spectrum of **1** and **1** with different organohalides (I – IV) in THF as solvent.

Table 1. Initial reaction screening.
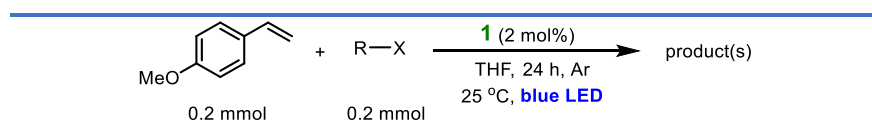
entry	R – X	product	yield (%)
1	CHCl$_3$	NR	–
2	Benzoyl chloride	**5aa**	10
3	Benzyl chloride		3
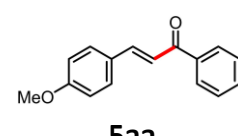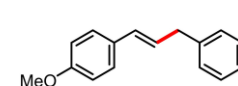
With the products obtained with acyl (10%) and benzyl chlorides (3%), we decided to focus on the reaction with acyl chloride. The product, chalcone, hinted at a unique reactivity of **1** since the formation of this type of product requires the addition of an oxidant and a base; or in the absence of additives, mixtures of saturated and unsaturated products would be formed.[11, 18] Additionally, acyl radicals are nucleophilic radicals and preferentially react with electron-deficient alkenes, hence the product formed also hinted on a catalyst-controlled product formation step.

Control experiments in the absence of **1** and light confirmed the relevance of these components in the reaction. Since we had already established that in the presence of a sacrificial electron donor and under light irradiation, complex **1** can be generated from complex **2**, we decided to carryout further optimization of the reaction with **2**. All optimizations and final optimized reaction condition employed for different substrates are shown in Table 2.

Table 2. Optimization of reaction condition.
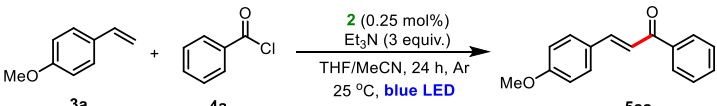
entry	deviation from the standard conditions	Yield (%)
1	none	73[a]
2	**1** (2 mol%)	10[b]
3	without **1**	nr[b]
4	without light	nr[b]
5	air	nr[b]
6	Et₃N (1.1 equiv.), **1** (2 mol%)	40[b]
7	**2** (2 mol%), Et₃N (1.1 equiv.)	27[b]
8	**2** (2 mol%), Et₃N (3 equiv.)	72[a]
9	CoCl₂ instead of **2**	nr[b]
10	CoCp₂ instead of **2**	nr[b]

[a]Reaction conditions (unless otherwise specified): **3a** (0.2 mmol, 1 equiv.), **4a** (0.4 mmol, 2 equiv.), MeCN/THF (1 mL each, dry, deoxygenated), blue LED (3 W, 455–460 nm). [b]**3a** (0.2 mmol, 1 equiv.), **4a** (0.2 mmol, 1 equiv.). Yields were determined by ^{1}H NMR using mesitylene as an internal standard. Yields are the average from at least two experiments. nr = no reaction.

4.3 Substrate Scope

With the optimized reaction conditions in hand, we screened some styrene and acyl chloride substrates to determine the scope of the reaction. Interestingly, all products obtained were *E*-isomers of the respective chalcones. As earlier stated, the acylation of **3a**, an electron-rich styrene, prompted our interest in exploring further the reaction since traditionally, acyl radicals are nucleophilic radicals and as such react with electron-deficient double bonds. Generally, electron-rich styrenes afforded higher yields of the desired product (68 − 72%) when compared to their electron-poor counterparts (36 − 50%). Furthermore, α-methyl 4-methoxystyrene **3g** afforded the desired product **5ga** in 84% yield. In contrast to the product obtained with **3g**, the styrene α-ethyl 4-methoxystyrene **3h** rather yielded the β,γ-unsaturated ketone **5ha** in 53% yield. With respect to acyl chlorides, electron-rich substrates performed slightly better than their electron-poor counterparts. Worth noting is that carbon-halogen bond activation only occurred in acyl carbon and not at any other carbon bearing a halogen bond.
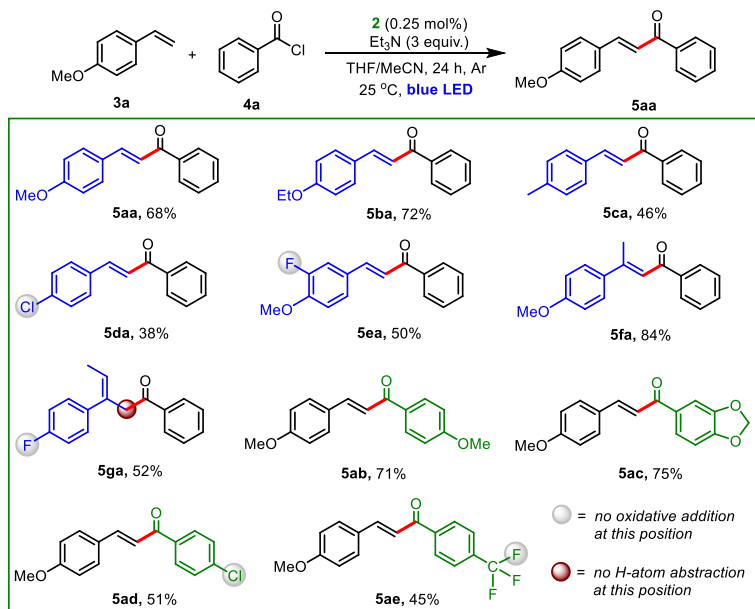
Figure 3. Substrate Scope. [a]Reaction conditions: **2a** (0.2 mmol, 1 equiv.), **3a** (0.4 mmol, 2 equiv.), MeCN/THF (1 mL each, dry, deoxygenated), blue LED (3 W, 455–460 nm).

4.4 Mechanistic Investigations

Due to sensitivity to light and solvents, macrocyclic Co[III]-alkyl and acyl complexes are very unstable. As such, isolation of these intermediates is very challenging.[11, 15] Despite the instability, we were able to isolate crystals suitable for X-ray structure determination when a THF solution of **1** and piperonoyl chloride **4c** and 4-chlorobenzoyl chloride **4d** were stored in the freezer (–35 to –40 °C) for several days. The molecular structures **6** (Figure 4) thus confirmed the oxidative addition of **1** to **4** to furnish Co[III]Mabiq acyl chloride intermediates. We hypothesize that irradiation of this intermediate leads to the formation of acyl radicals and metalloradical Co[II](Mabiq). The Co–C bond in **6a** and **b** (1.950 Å and 1.944 Å, respectively) is shorter than the Co–Cl bond in the same molecule (2.469 Å and 2.444 Å, respectively) but comparable to those reported for Co–C bonds in vitamin B_{12}–alkyl and other macrocyclic Co[III]–alkyl compounds, which have also been reported to undergo Co–C bond homolysis.[15a] Despite the success achieved in obtaining molecular structures of **6**, recording NMR spectra of the intermediates was challenging. The compounds reverted to the parent Co[I](Mabiq) when the crystals were redissolved in NMR solvents such as THF-d8, CD3CN and benzene-d6. Nevertheless, ^{1}H NMR spectra of freshly prepared solutions provided further evidence for the formation of Co(Mabiq)-acyl chloride intermediates (see Appendix III, Figures 7 and 10).
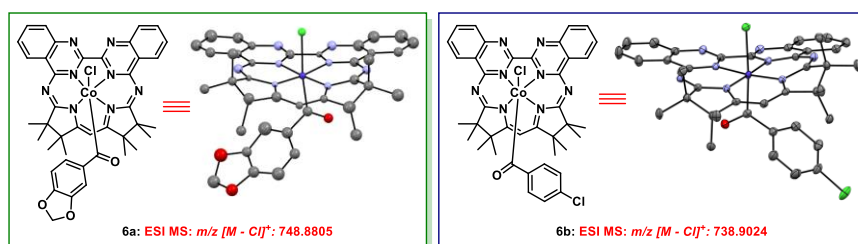
Figure 4. Molecular structures of Co(Mabiq) acyl chloride intermediates.

58

In order to obtain more evidence to support the generation of acyl radical from Co(Mabiq)-acyl chloride, the photo-behaviour of in situ generated Co(Mabiq)-benzoyl chloride species (ESI MS: m/z $[M - Cl]^+$ = 705.0470; see Appendix III, Figure 12) with and without added styrene **3a** were monitored via UV-Vis. Indeed, we observed that the initial spectra obtained in both experiments changed over time upon irradiation producing spectra similar to that of **2** after several minutes of irradiation, indicating that the newly formed Co(Mabiq)-benzoyl chloride species was photoactive (Figure 5A and B). Also, ESI MS analysis of the solution containing styrene **3a** indicated that the chalcone **5aa** was formed (see Appendix III, Figure 13).
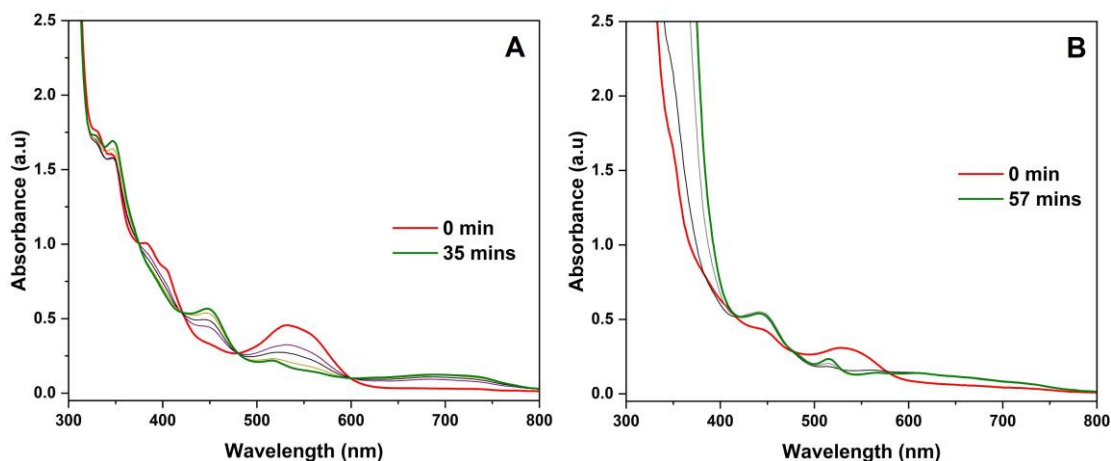
Figure 5. UV-Vis spectral evolution: **(A)** Solution of Co(Mabiq) **1** (50 µM) and benzoyl chloride **4a** (450 µM, 9 equiv.) in THF/MeCN (1:1). *Red trace:* spectrum of the solution prior to irradiation. *Green trace:* spectrum obtained after irradiation of the solution with blue LED (455 nm, P_{ref} = 118 mW). **(B)** Solution of Co(Mabiq) **1** (50 µM), benzoyl chloride **4a** (450 µM, 9 equiv.) and **3a** (450 µM, 9 equiv.) in THF/MeCN (1:1). *Red trace:* spectrum of the solution prior to irradiation. *Green trace:* spectrum obtained after irradiation of the solution with blue LED (455 nm, P_{ref} = 80 mW).

Further mechanistic experiments included a 2-step-one-pot stoichiometric reaction in which **1** and piperonoyl chloride **4c** (1 equiv. each) in MeCN/THF (1:1) (ESI MS: m/z $[M - Cl]^+$ = 748.8805; see Appendix III, Figure 14) was stirred in the dark for one hour after which styrene **3a** (3 equiv.) was added. Irradiation of the solution for 17 hours and analysis by ^{1}H NMR revealed the presence of the cross-coupled product **5ac** in 56% yield (Scheme 2A). Control experiments in the dark did not yield the desired product (Scheme 2A). Finally, a radical clock experiment using styrene **3i**, which afforded the ring-open product **5ia** in 27% yield (Scheme 2B) further confirmed the generation of acyl radicals.
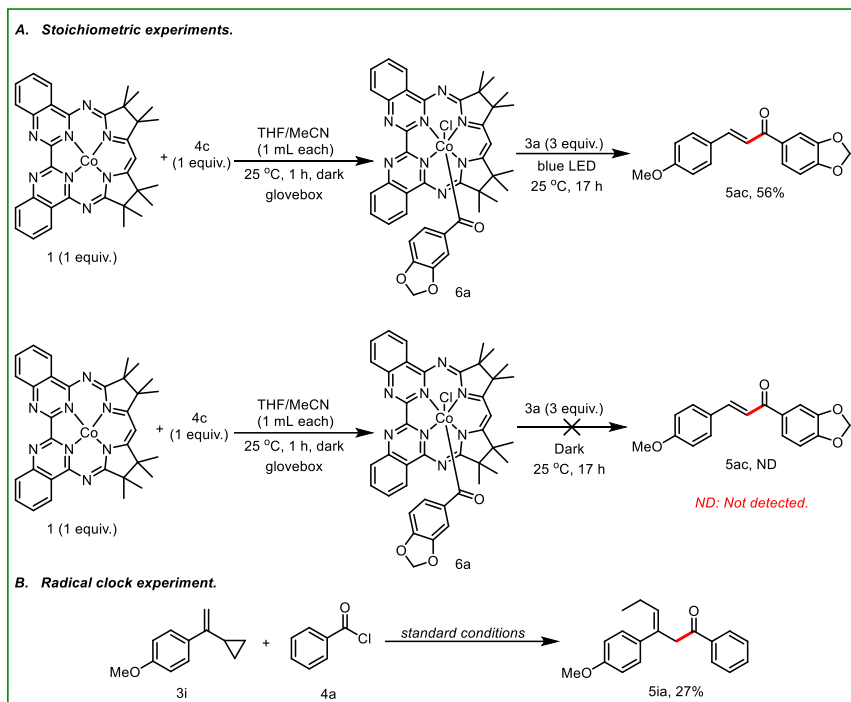
Scheme 2. Stoichiometric and radical clock experiments.

The results from the mechanistic investigations provide evidence in support of the catalytic cycle proposed in Scheme 3. Upon excitation of **2**, a SET ensues from the sacrificial electron donor Et$_3$N to generate **1** which then undergoes oxidative addition to acyl chloride to furnish intermediate **6**. Excitation of **6** leads to a VLIH to produce acyl radical and metalloradical Co^{II}-Mabiq species **A**. These types of radical species **A** are proposed to remain in an intermediate solvent caged radical pair, in which they can recombine to form **6** or diffuse freely out of the solvent cage.[16] Since acyl radicals are traditionally nucleophilic and thus only react with electrophilic double bonds, we speculate that both radicals remained in close proximity, thus determining the regioselectivity of the radical addition step and reactivity of the radical in the presence of styrenes **3**. The proximity of the caged radical pair in **A** may reduce the nucleophilicity of the acyl radical, ensuring that it reacts with styrenes **3** and even affording higher yields of the desired product **5** with styrenes bearing electron-donating substituents (Figure 3). The non-reactivity of the acyl radical intermediate in **A** with aliphatic alkenes and even β-substituted styrenes further supports the assertion that the radical is not a free radical species (see Appendix III, Figure 5 for unsuccessful substrate). Addition of the acyl radical to **3** generates the alkyl radical **B** and this undergoes a radical rebound unto the metalloradical Co^{II}-Mabiq species to produce **C**. At this stage, a dehydrocobaltation reaction (MHAT)[1b, 3, 5, 11, 16-17] step is a plausible pathway that could furnish the desired product. This could occur when intermediate **C** is excited and then undergoes VLIH to generate the alkyl radical and metalloradical Co^{II}-Mabiq species **D** which remain as a solvent caged radical pair. The metalloradical then abstracts a β-hydrogen atom from the alkyl radical to furnish the desired product **5** and hydridocobalt(III) species **E**. Finally, excitation of **E** and SET from Et$_3$N to **E** furnishes the catalyst **1**.
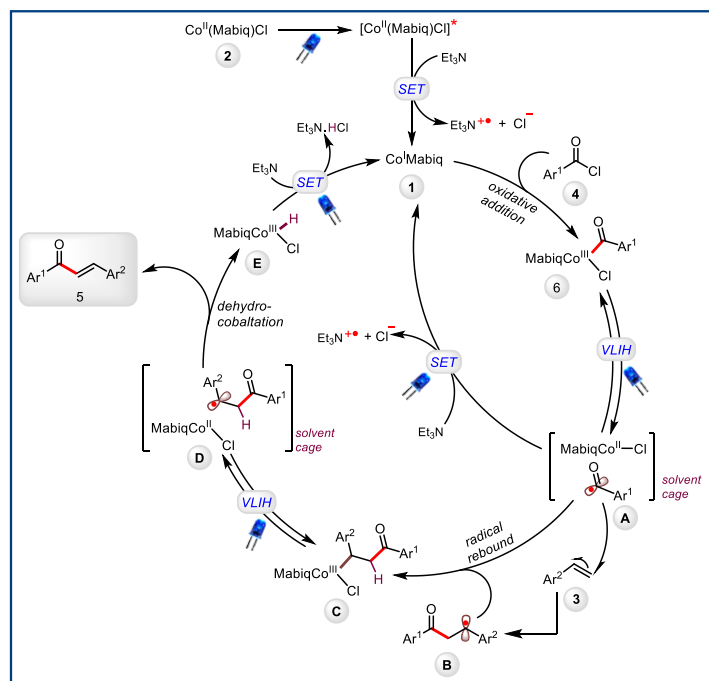
Scheme 3. Plausible mechanism.

While these latter steps require further studies to verify, the mechanistic steps **C → E** above is more plausible when compared to β-hydride elimination (BHE) at metal centers since BHE requires a vacant *cis* site for such elementary step to occur. In the Co-Mabiq complex, a vacant *cis* site is not available and due to the rigidity of the macrocyclic ligand, in situ rearrangement to provide a *cis* site for BHE is highly unlikely. Also, a base assisted dehalo-dehydrogenation was proposed for double-bond retention by Zhu and coworkers.[18] However, since our strategy did not employ external oxidants and the product **5aa** was also formed when **1** was used as the catalyst in the absence of Et₃N, the pathway involving base-assisted dehalo-dehydrogenation is thus excluded as a possible product forming step. Finally, *E*-isomers of α,β-unsaturated ketones were exclusively formed, and this suggests that the Co-Mabiq complex like plays a critical role in the *E*-diastereoselective step with the bulky Mabiq ligand influencing the final isomer that is produced.

4.5 Conclusion

In summary, a visible-light induced protocol for the synthesis of α,β- and β,γ-unsaturated ketones has been developed. The Co-Mabiq catalyzed reaction utilizes the ability of the complex to adopt different roles both in its ground and excited states to forge C–C bonds. Although inconclusive, preliminary mechanistic investigations revealed that the key steps included oxidative addition of the complex to C–Cl bonds in acyl chlorides, generation of acyl radicals via VLIH upon excitation and a plausible dehydrocobaltation to furnish the unsaturated ketones. This mild protocol which precludes the requirement for oxidant/reductants, bases or cocatalyst demonstrates the ability of Co-Mabiq complexes not just to act as metal centers for catalysis but also as photoactive complexes for radical generation and controlled addition to suitable alkenes.

4.6 References

1. (a) Demarteau, J.; Debuigne, A.; Detrembleur, C., Organocobalt Complexes as Sources of Carbon-Centered Radicals for Organic and Polymer Chemistries. *Chem. Rev.* **2019,** *119* (12), 6906-6955; (b) Patel, V. F.; Pattenden, G.; Thompson, D. M., Cobalt-mediated reactions in synthesis. The degradation of carboxylic acids to functionalised noralkanes via acylcobalt salophen intermediates. *J. Chem. Soc. Perkin Trans.* **1990,** *1*, 2729-2734.

2. Debuigne, A.; Poli, R.; Jérôme, C.; Jérôme, R.; Detrembleur, C., Overview of cobalt-mediated radical polymerization: Roots, state of the art and future prospects. *Prog. Polym. Sci.* **2009,** *34* (3), 211-239.

3. Bam, R.; Pollatos, A. S.; Moser, A. J.; West, J. G., Mild olefin formation via bio-inspired vitamin B(12) photocatalysis. *Chem. Sci.* **2020,** *12* (5), 1736-1744.

4. (a) Giedyk, M.; Goliszewska, K.; Gryko, D., Vitamin B12 catalyzed reactions. *Chem. Soc. Rev.* **2015,** *44* (11), 3391-404; (b) Wdowik, T.; Gryko, D., C–C Bond Forming Reactions Enabled by Vitamin B12–Opportunities and Challenges. *ACS Catal.* **2022,** *12* (11), 6517-6531; (c) Bhandal, H.; Pattenden, G., Hydrocobaltation-Dehydrocobaltation Reactions in Synthesis: A New Approach to the Controlled Cross-Coupling between sp^2 Carbon Centers leading to Functionalised Alkenes. *J. Chem. Soc. Commun.* **1988**, 1110-1112; (d) Pattenden, G., Cobalt-mediated Radical Reactions in Organic Synthesis. . *Chem. Soc. Rev.* **1988,** *17*, 361–382.

5. Prusinowski, A. F.; Sise, H. C.; Bednar, T. N.; Nagib, D. A., Radical Aza-Heck Cyclization of Imidates via Energy Transfer, Electron Transfer, and Cobalt Catalysis. *ACS Catal.* **2022,** *12* (8), 4327-4332.

6. Banerjee, A.; Lei, Z.; Ngai, M. Y., Acyl Radical Chemistry via Visible-Light Photoredox Catalysis. *Synthesis (Stuttg)* **2019,** *51* (2), 303-333.

7. de Pedro Beato, E.; Mazzarella, D.; Balletti, M.; Melchiorre, P., Photochemical generation of acyl and carbamoyl radicals using a nucleophilic organic catalyst: applications and mechanism thereof. *Chem. Sci.* **2020,** *11* (24), 6312-6324.

8. Capaldo, L.; Riccardi, R.; Ravelli, D.; Fagnoni, M., Acyl Radicals from Acylsilanes: Photoredox-Catalyzed Synthesis of Unsymmetrical Ketones. *ACS Catal.* **2017,** *8* (1), 304-309.

9. Tripathi, S.; Kapoor, R.; Yadav, L. D. S., Visible Light Activated Radical Denitrative Benzoylation ofβ-Nitrostyrenes: A Photocatalytic Approach to Chalcones. *Adv. Synth. Catal.* **2018,** *360* (7), 1407-1413.

10. Chinchole, A.; Henriquez, M. A.; Cortes-Arriagada, D.; Cabrera, A. R.; Reiser, O., Iron(III)-Light-Induced Homolysis: A Dual Photocatalytic Approach for the Hydroacylation of Alkenes Using Acyl Radicals via Direct HAT from Aldehydes. *ACS Catal.* **2022,** *12*, 13549-13554.

11. Coveney, D. J.; Patel, V. F.; Pattenden, G.; Thompson, D. M., Acylcobalt salophen reagents. Precursors to acyl radical intermediates for use in carbon-to-carbon bond-forming reactions to alkenes. *J. Chem. Soc. Perkin Trans.* **1990,** *1*, 2721-2728.

12. Ociepa, M.; Baka, O.; Narodowiec, J.; Gryko, D., Light-driven vitamin B$_{12}$-catalyzed generation of acyl radicals from 2-S-pyridyl thioesters. *Adv. Synth. Catal.* **2017,** *359* (20), 3560-3565.

13. Abderrazak, Y.; Bhattacharyya, A.; Reiser, O., Visible-light-induced homolysis of earth-abundant metal-substrate complexes: A complementary activation strategy in photoredox catalysis. *Angew. Chem. Int. Ed. Engl.* **2021,** *60* (39), 21100-21115.

14. Esezobor, O. Z.; Zeng, W.; Niederegger, L.; Grubel, M.; Hess, C. R., Co-mabiq flies solo: Light-driven Markovnikov-selective C- and N-alkylation of indoles and indazoles without a cocatalyst. *J. Am. Chem. Soc.* **2022,** *144* (7), 2994-3004.

15. (a) Kofod, P.; Moore, P.; Alcock, N. W.; Clase, H. J., A New Model Compound for Vitamin B$_{12}$ Coenzyme: Synthesis and Crystal Structure of a Tetraazamacrocyclic Alkylcobalt(III)

Compound with a Pendant Coordinating Alkyl Arm. *J. Chem. Soc. Chem. Commun.* **1992,** *1*, 1261-1263; (b) Ociepa, M.; Wierzba, A. J.; Turkowska, J.; Gryko, D., Polarity-Reversal Strategy for the Functionalization of Electrophilic Strained Molecules via Light-Driven Cobalt Catalysis. *J. Am. Chem. Soc.* **2020,** *142* (11), 5355-5361; (c) Li, G.; Zhang, F. F.; Chen, H.; Yin, H. F.; Chen, H. L.; Zhang, S. Y., Determination of Co–C Bond Dissociation Energies for Organocobalt Complexes related to Coenzyme B$_{12}$ using Photoacoustic Calorimetry. *J. Chem. Soc. Dalt. Trans.* **2002,** (1), 105-110.

16. Woska, D. C.; Xie, Z. D.; Gridnev, A. A.; Ittel, S. D.; Wayland, M. F. B. B., Determination of Organo-Cobalt Bond Dissociation Energetics and Thermodynamic Properties of Organic Radicals through Equilibrium Studies. *J. Am. Chem. Soc.* (118), 9102-9109.

17. Giedyk, M.; Goliszewska, K.; o Proinsias, K.; Gryko, D., Cobalt(I)-catalyzed CH-alkylation of Terminal Olefins, and Beyond. *Chem. Comm.* **2016,** *52* (7), 1389-1392.

18. Zhang, M.; Xi, J.; Ruzi, R.; Li, N.; Wu, Z.; Li, W.; Zhu, C., Domino-Fluorination-Protodefluorination Enables Decarboxylative Cross-Coupling of alpha-Oxocarboxylic Acids with Styrene via Photoredox Catalysis. *J. Org. Chem.* **2017,** *82* (18), 9305-9311.

Summary

In this PhD dissertation, photoinduced catalytic reactions utilizing Co, Ni and Zn complexes based on the macrocyclic biquinazoline ligand (Mabiq) were developed. Building on the already established photoredox ability of the Ni-Mabiq complex in the cyclization of bromoalkyl-substituted indole, we further showed that the Ni-Mabiq complex can catalyze other reactions such as the photoinduced oxidative coupling of benzylamines and aza-Henry reaction. A comparative study of the efficiency of the Ni- and Zn-Mabiq complexes in the reactions revealed the distinct behaviours of both catalyst in the reactions studied. The distinct photocatalytic behaviours of the complexes are linked to the excited states properties of the complexes. For the Ni-Mabiq, the excited states are metal-centered while for the Zn-Mabiq, the excited states are ligand centered. Although the Zn-Mabiq possesses a longer excited state lifetime when compared to the Ni-Mabiq, the instability of its reduced form offers a disadvantage for the use of the complex as a photocatalyst. However, the Ni-Mabiq is stable and is as efficient as the well-established $[Ru(bpy)_3]^{2+}$ and $[Ir(ppy)_2(dtbbpy)]^+$.[1]
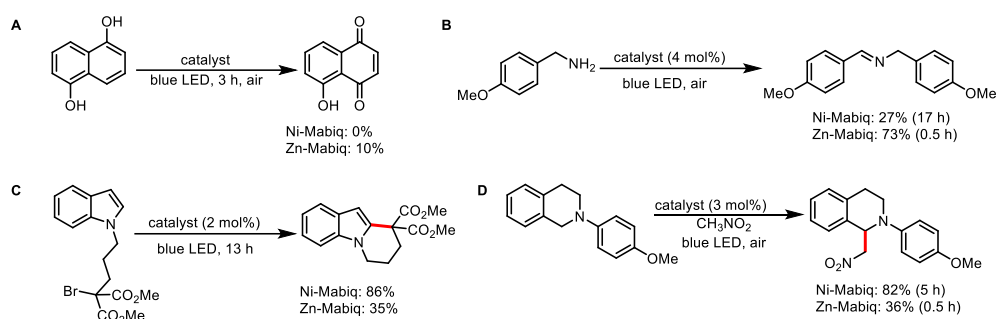
Figure 1. Photocatalyzed reactions by Ni- and Zn-Mabiq.

In the second project, we switched our attention to exploring the photocatalytic activity of Co-Mabiq complexes. Following a mechanistic approach, we observed that the $Co^{III}(Mabiq)Cl_2$ is photoactive and undergoes homolytic cleavage of the Co – Cl bond. Also, the complex showed a distinct behaviour when it was irradiated in the presence of allyl bromide. We further found that upon addition of 4-methoxystyrene to the Co(Mabiq)Cl and allylbromide solution, a head-to-tail dimer of the styrene was formed when the solution was irradiated. Further analysis of the Co(Mabiq)Cl and allylbromide solution revealed the presence of a brominated Co-complex. With this key information, the brominated ligand and subsequently $Co(MabiqBr)Cl_2$ were synthesized. The new complex was characterized and was found to catalyze the Markovnikov-selective C3 and N-alkylation of indoles and indazoles with electron-rich styrenes. Mechanistic investigations provided insights into the several roles of the Co-MabiqBr complex which include oxidation of the electron-rich styrenes upon irradiation, to generate Co^{II}-intermediate and styrene radical cation. Due to the bulky nature of the Mabiq ligand, a controlled radical rebound ensues, affording a Co^{III}-Mabiq alkyl intermediate which upon nucleophilic attack by indole, indazoles or even alcohols produced the Markovnikov-selective alkylated product.
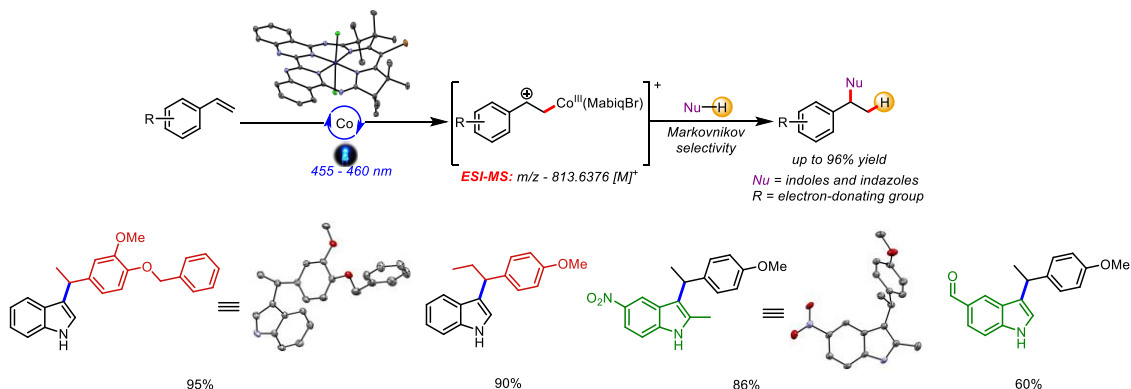
Figure 2. Photoinduced and Co-MabiqBr catalyzed Markovnikov-selective C3 and N-alkylation of indoles and indazoles with styrenes.

The final project in this PhD thesis explored the ability of the supernucleophilic Co^I-Mabiq to engage in oxidative addition to carbon-chloride bond in acyl chloride to furnish Co^{III}-Mabiq acyl adducts. These intermediates upon irradiation released acyl radical which were added to styrenes to furnish α,β- and β,γ-unsaturated ketones. UV-Vis, X-ray and ^{1}H NMR analysis confirmed the formation Co-Mabiq acyl intermediate. Although further mechanistic investigations are required to fully understand the further roles of the Co-Mabiq in the catalytic cycle, preliminary studies revealed that the catalyst adopted several roles, including a plausible dehydrocobaltation step.
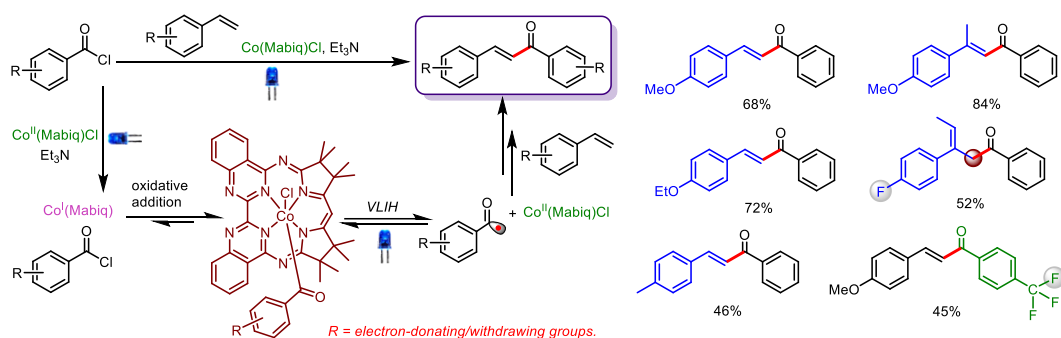
Figure 3. Photoinduced and Co-Mabiq catalyzed acylation of styrenes with acyl chloride.

The catalytic reactions presented in this dissertation highlight the ability of Co-, Ni- and Zn-Mabiq as potent photocatalysts. Intriguingly, the studies employing Co-Mabiq revealed that the complexes can adopt several roles in photoinduced catalytic reactions. This feature makes the Co-Mabiq complexes unique and opens new mechanistic paradigms for photoinduced reactions and use of similar complexes.

1. Lauenstein, R.; Mader, S. L.; Derondeau, H.; Esezobor, O. Z.; Block, M.; Romer, A. J.; Jandl, C.; Riedle, E.; Kaila, V. R. I.; Hauer, J.; Thyrhaug, E.; Hess, C. R., The central role of the metal ion for photoactivity: Zn- vs. Ni-Mabiq. *Chem. Sci.* **2021,** *12* (21), 7521-7532

2. Esezobor, O. Z.; Zeng, W.; Niederegger, L.; Grubel, M.; Hess, C. R., Co-Mabiq flies solo: Light-driven Markovnikov-selective C- and N-alkylation of indoles and indazoles without a cocatalyst. *J. Am. Chem. Soc.* **2022,** *144* (7), 2994-3004.

Appendix

1. ESI MS spectra of solutions of Co(Mabiq) and organohalides
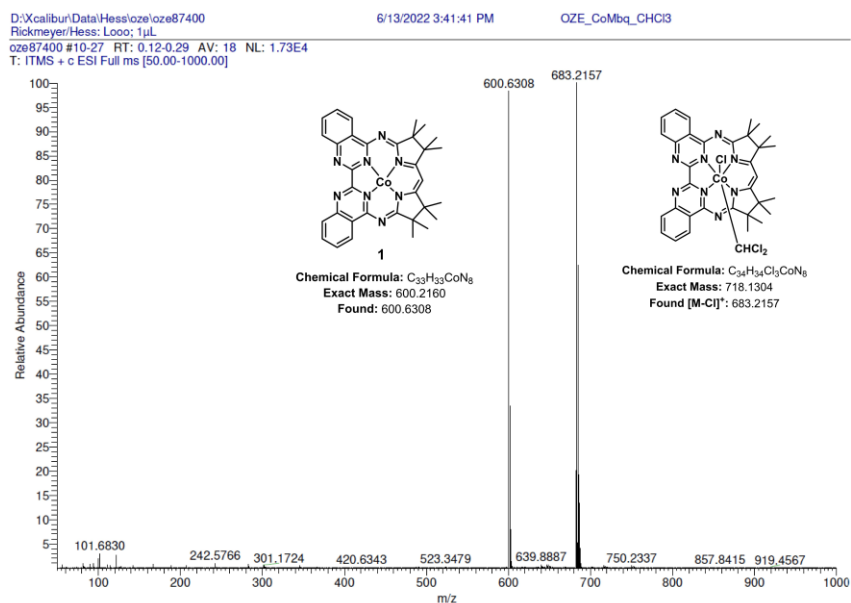
Figure 1. ESI MS spectrum obtained after addition of chloroform to a THF solution of Co(Mabiq).
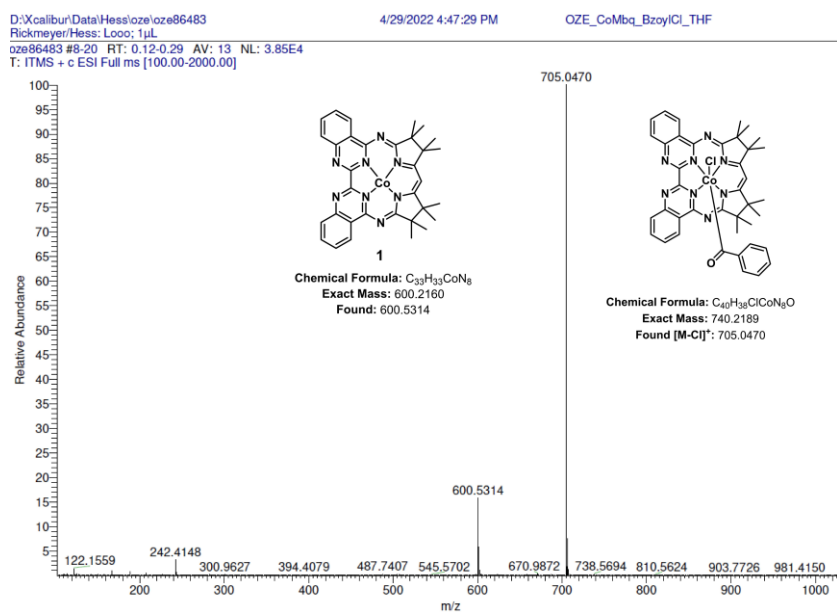
Figure 2. ESI MS spectrum obtained after addition of benzoyl chloride to Co(Mabiq) in THF.
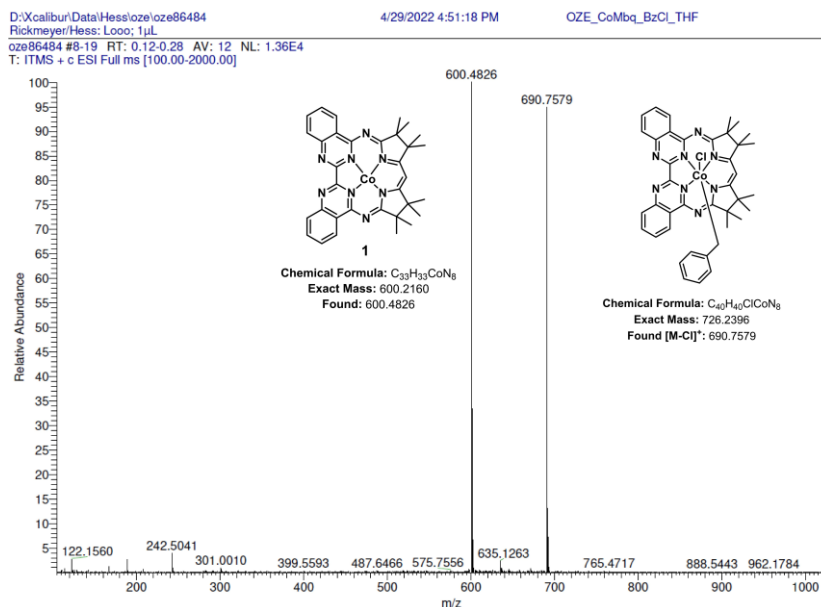
Figure 3. ESI MS spectrum obtained after addition of benzyl chloride to Co(Mabiq) in THF.

2. Description of General Procedure for the Photoinduced Synthesis of Chalcones.

I. Preparation of Catalyst Stock Solution

In a glovebox under argon atmosphere, 0.5 mM solution of catalyst **2** was prepared in MeCN and THF (10 mL each). From the stock solution, 1 mL was taken and made up to 2 mL with MeCN/THF (0.5 mL each) as catalyst solution for all reactions.

II. Reaction Procedure

In a glovebox, 1 mL of catalyst stock solution was added into a 5 mL crimp cap vial equipped with a stir bar and made up to 2 mL with MeCN and THF (0.5 mL each). This gave a catalyst concentration of 0.25 mM (318 μg, 0.25 mol% or 0.0025 equiv. with styrene (0.2 mmol) as limiting reagent). The vial was crimped, removed from the glovebox and the remaining reagents were subsequently added under Ar atmosphere as described below. *All reagents and solvents were deoxygenated prior to addition.*

Addition of reagents – The styrene and acid chloride were purged with argon and 0.2 mmol (1.0 equiv.) of the styrene and 0.4 mmol (2.0 equiv.) of the acid chloride were added to the sealed vial containing the catalyst stock solution with a Hamilton syringe. Deoxygenated triethyl amine (84 μL, 0.6 mmol, 3.0 equiv.) was added to the sealed vial with a Hamilton syringe and the cap was covered with Parafilm. The reaction mixture was placed in the photoreactor setup and irradiated (3 W, 455 – 460 nm LED; T = 25 °C) for 18 hours. After the reaction time, solvent was removed in a rotary evaporator and the products were purified by silica gel flash column chromatography using a mixture of hexane and ethyl acetate as eluent. Alternatively, to directly determine the product yield by ^{1}H NMR, the crude reaction mixture was first filtered through a plug of aluminum oxide and concentrated in a rotatory evaporator. The crude product was dissolved in CDCl$_3$ and mesitylene was added as an internal standard.

3. Reaction Optimization

Table 1. Screening for solvent and amount of Et$_3$N.

entry	solvent	Et$_3$N equiv.	yield (%)
1	MeCN (2 mL)	1.1	25±2
2	THF (2 mL)	1.1	27±3
3	MeCN/THF (1 mL each)	1.1	40±2
4	MeCN/THF (1 mL each)	1.5	55±4
5	MeCN/THF (1 mL each)	2.0	59±5
6	MeCN/THF (1 mL each)	2.5	57±2
7	**MeCN/THF (1 mL each)**	**3.0**	**72±2***

Reaction conditions: **3a** (0.2 mmol, 1 equiv.), **4a** (0.2 mmol, 1 equiv.); *2 equiv. of **4a** was used; Yields were determined by ^{1}H NMR using mesitylene as an internal standard and CDCl$_3$ as NMR solvent.

Table 2. Screening for sacrificial electron donor (SED).

entry	SED	yield (%)
1	Et$_3$N	72±2
2	DIPEA	39±2
3	Triphenyl amine	0
4	DABCO	0
5	2,6-lutidine	25±3
6	DMAP	Traces
7	Zn	Complex reaction mixture
8	CoCp$_2$	61±3

Reaction conditions: **3a** (0.2 mmol, 1 equiv.), **4a** (0.4 mmol, 2 equiv.); MeCN/THF (1 mL each); Yields were determined by ^{1}H NMR using mesitylene as an internal standard and CDCl$_3$ as NMR solvent.

Table 3. Screening for additives.

entry	additive	yield (%)
1	None	72±2
2	K$_2$CO$_3$	45±4
3	NH$_4$Cl	28±3
4	MgSO$_4$	55±5
5	KCl	54±3
6	Molecular sieves	62±9

Reaction conditions: **3a** (0.2 mmol, 1 equiv.), **4a** (0.4 mmol, 2 equiv.); MeCN/THF (1 mL each); Yields were determined by ^{1}H NMR using mesitylene as an internal standard and CDCl$_3$ as NMR solvent.

Table 4. Screening for cobalt complexes.

entry	catalyst	yield (%)
1	**2** (2 mol%)	72±2
2	CoCl$_2$ (10 mol%)	0
3	CoCp$_2$ (10 mol%)	0

Reaction conditions: **3a** (0.2 mmol, 1 equiv.), **4a** (0.4 mmol, 2 equiv.); MeCN/THF (1 mL each); Yields were determined by ^{1}H NMR using mesitylene as an internal standard and CDCl$_3$ as NMR solvent.

Table 5. Screening for time (2 mol%).

entry	time (h)	yield (%)
1	6	36±3
2	12	65±1
3	15	67±1
4	18	70±2
5	24	72±2

Reaction conditions: **3a** (0.2 mmol, 1 equiv.), **4a** (0.4 mmol, 2 equiv.); MeCN/THF (1 mL each); Yields were determined by ^{1}H NMR using mesitylene as an internal standard and CDCl$_3$ as NMR solvent.

Table 6. Screening for time (0.25 mol%).
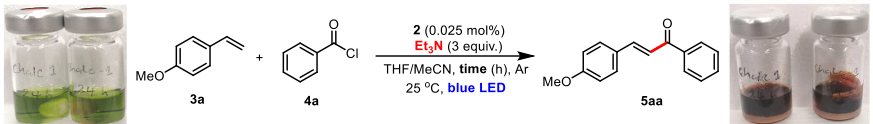
entry	Time (h)	yield (%)
1	3	31±9
2	6	48±1
3	9	54±1
4	12	57±3
5	15	60±1
6	18	64±1
7	24	73±3

Reaction conditions: **3a** (0.2 mmol, 1 equiv.), **4a** (0.4 mmol, 2 equiv.); MeCN/THF (1 mL each); Yields were determined by ^{1}H NMR using mesitylene as an internal standard and CDCl$_3$ as NMR solvent.
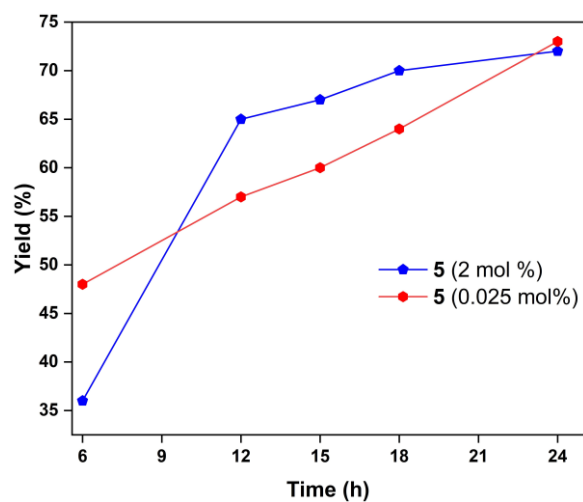
Figure 4. Comparison of yields obtained with different catalyst loading.
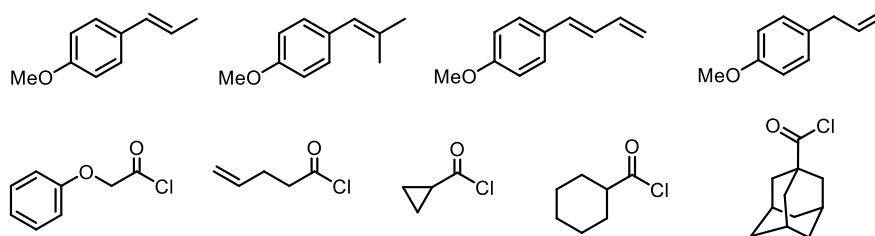
Figure 5. Unsuccessful substrates.

4. Mechanistic Investigations

4.1 Preparation of Stock Solutions

The samples were prepared under an argon atmosphere inside a glovebox and under red light conditions. A cuvette fitted with a ChemGlass valve and stir bar was used for all measurements. The sealed cuvette was removed from the glove box, ensuring that no light reached the sample, and an absorption spectrum was taken. This measurement gave the reference absorption spectrum prior to LED illumination (t = 0 spectrum). The cuvette was then transferred to the QYDS setup and the sample was irradiated with blue LED (455 nm) at various time intervals. An absorption spectrum was taken at each time interval until no further change of the spectrum is observed.

Stock solutions of Co(Mabiq) **1** (0.4 mM in MeCN/THF, 5 mL each), Co(Mabiq)Cl **2** (0.4 mM in MeCN/THF, 5 mL each), Et$_3$N (50 mM in MeCN/THF, 5 mL each), 4-methoxystyrene **3a** (5 mM in MeCN/THF, 5 mL each) and benzoyl chloride **4a** (5 mM in MeCN/THF, 5 mL each) were prepared separately and stirred overnight for the catalyst complexes and reagent to dissolve properly.

4.2 Photoreduction of 2

From the 0.4 mM stock solution of **2**, 250 μL was measured with a Hamilton syringe into a J-Young cuvette equipped with a magnetic stirring bar. Then, 1 mL was measured from the 50 mM Et$_3$N stock solution and added to the cuvette. The combined solution was made up to 2 mL with equal volume of MeCN/THF such that the final concentrations of **2** and Et$_3$N were 50 μM and 25 mM (500 equiv.) respectively. The sample was prepared under red light condition and the experiment was carried out 3 times.

4.3 ^{1}H NMR and ESI MS Studies on Co(Mabiq) acyl chloride Intermediates
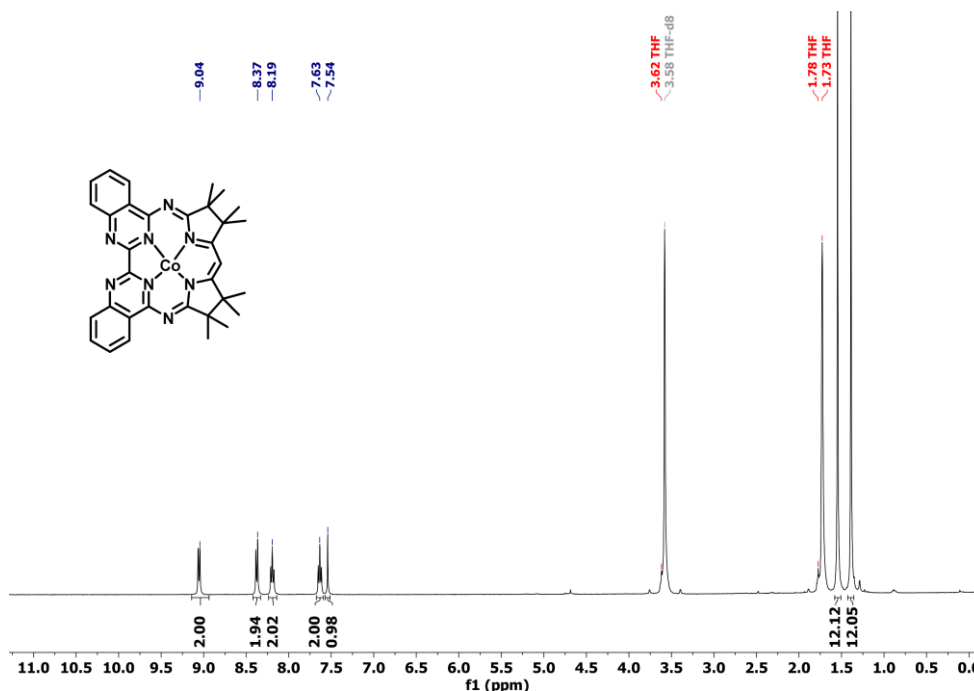
Figure 6. ^{1}H NMR spectrum of **1**.

71
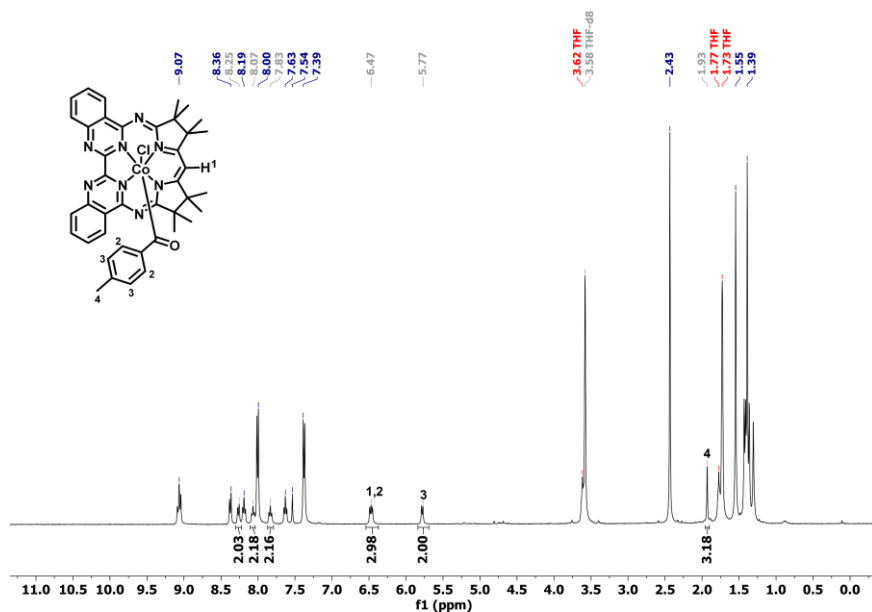
Figure 7. ^{1}H NMR spectrum of in situ generated Co(Mabiq)-4-methylbenzoyl chloride. Grey peaks with integrals correspond to protons of Co(Mabiq)-4-methylbenzoyl chloride. Unintegrated blue peaks correspond to protons of unreacted Co(Mabiq) and 4-methylbenzoyl chloride.
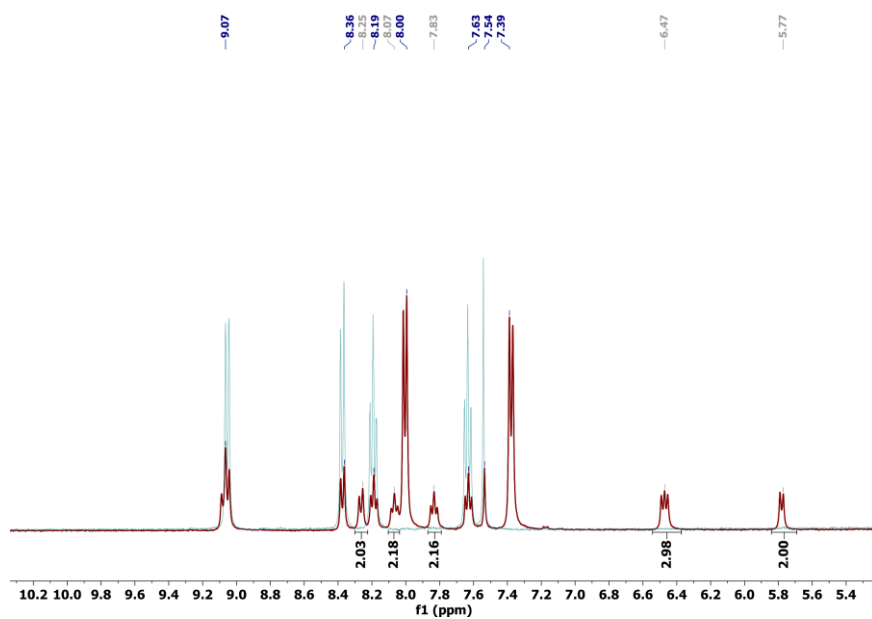
Figure 8. Overlay of Figures 6 (blue) and 7 (red).
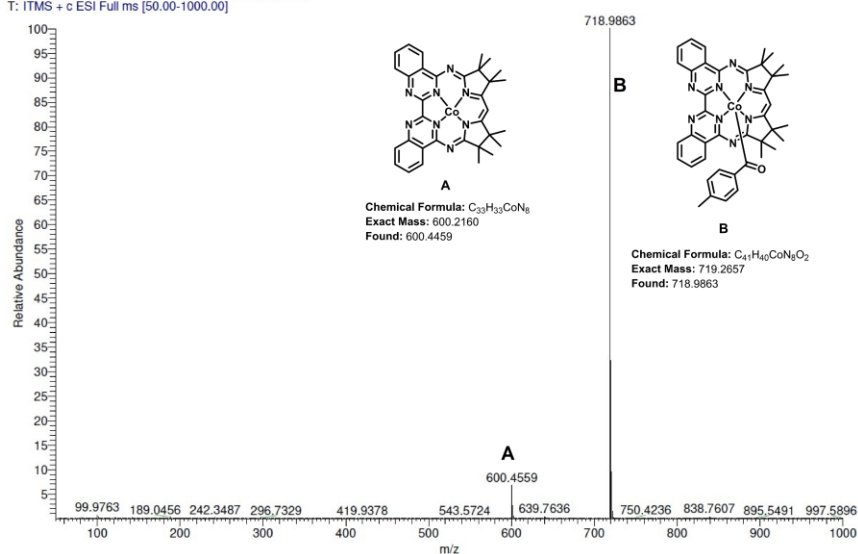
Figure 9. ESI MS spectra of Co(Mabiq) 4-methylbenzoyl chloride **B**, *m/z* = [M–Cl]⁺.
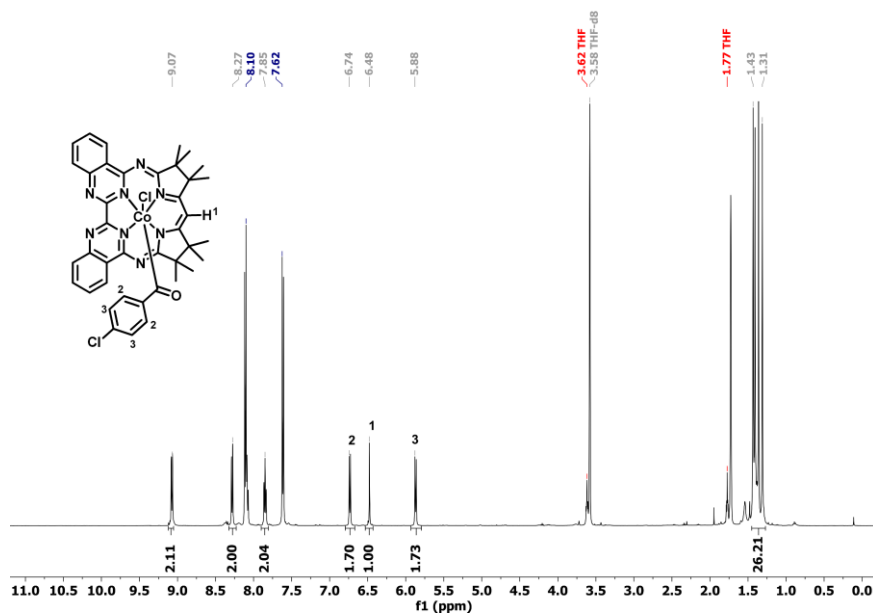
Figure 10. ¹H NMR spectrum of in situ generated Co(Mabiq)-4-chlorobenzoyl chloride. Grey peaks with integrals correspond to protons of Co(Mabiq)-4-chlorobenzoyl chloride.
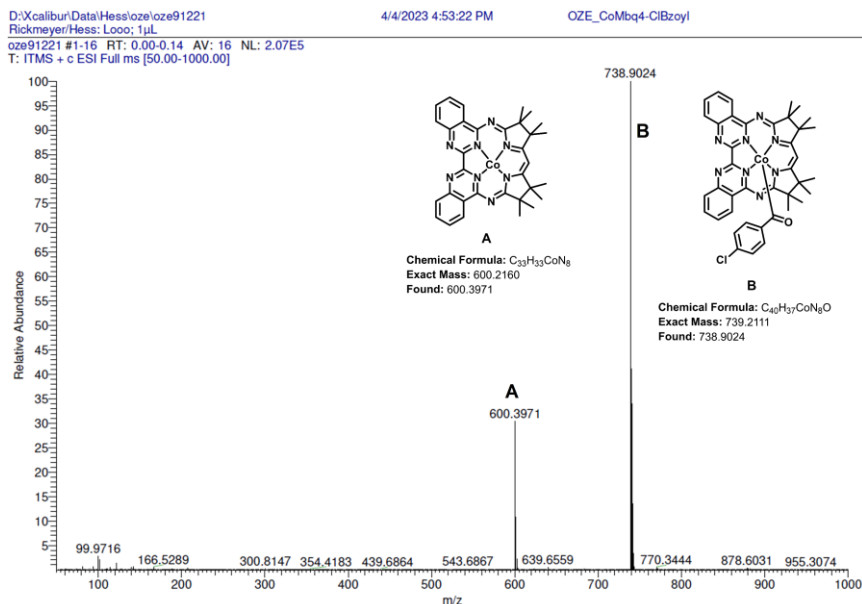
Figure 11. ESI MS spectra of Co(Mabiq) 4-chlorobenzoyl chloride **B**, m/z = [M–Cl]$^+$.
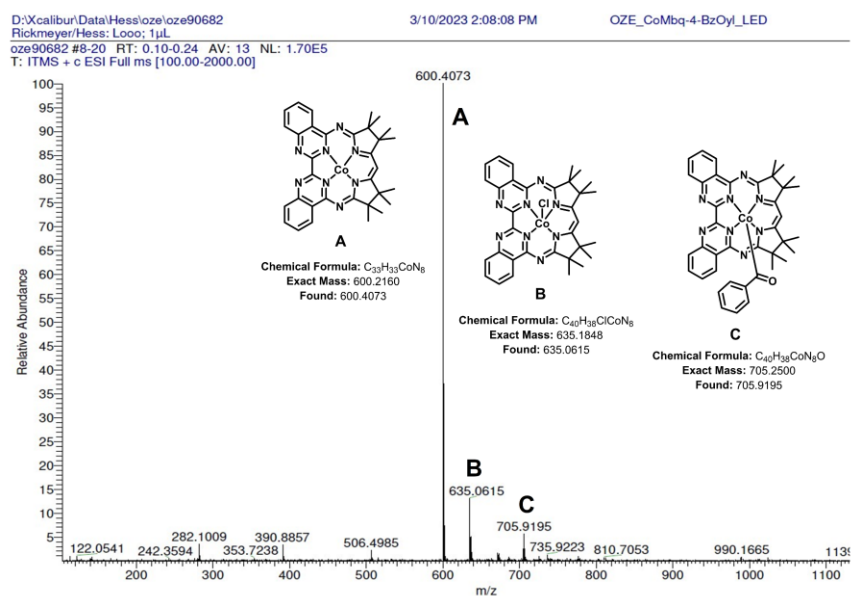
Figure 12. ESI MS of final solution from UV-Vis spectral evolution of a solution of Co(Mabiq) **1** (50 μM) and benzoyl chloride **4a** (450 μM, 9 equiv.) in THF/MeCN (1:1).
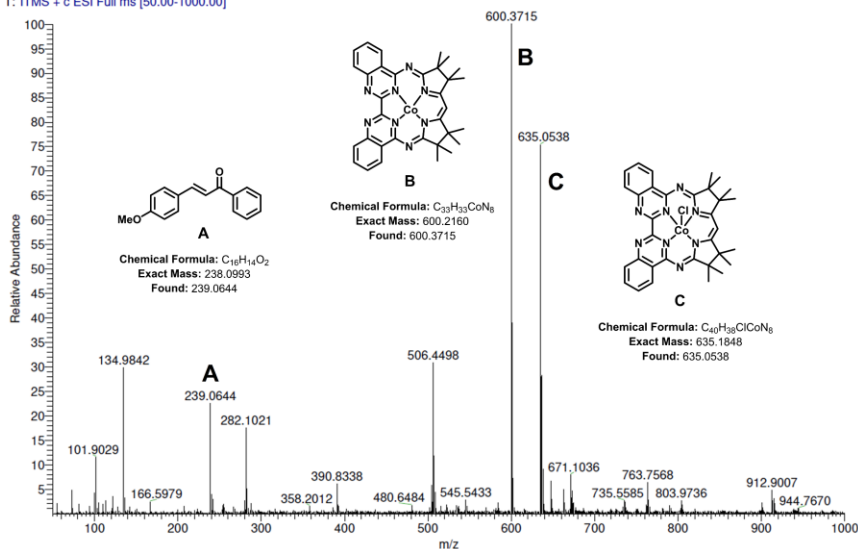
Figure 13. ESI MS of final solution from UV-Vis spectral evolution of a solution of Co(Mabiq) **1** (50 μM), 4-methoxystyrene **3a** (450 μM, 9 equiv.) and benzoyl chloride **4a** (450 μM, 9 equiv.) in THF/MeCN (1:1).
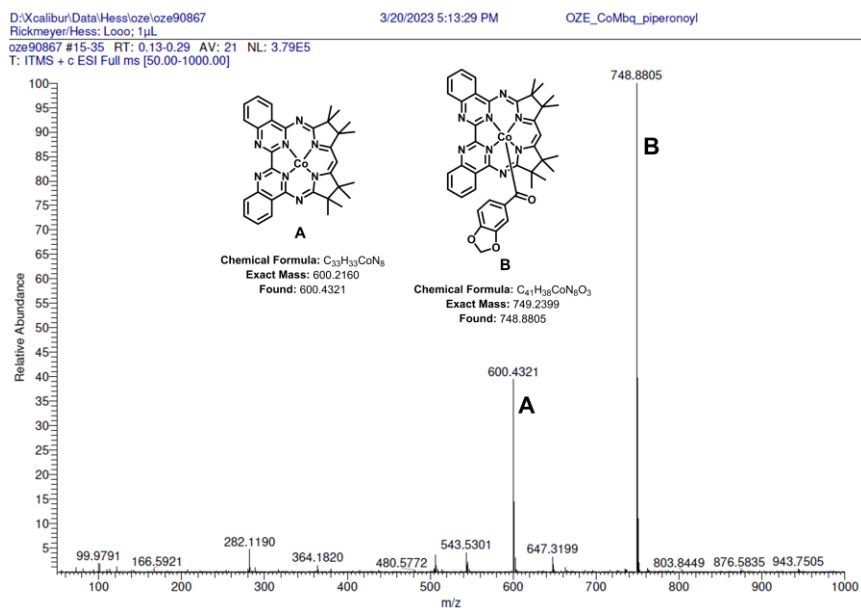
Figure 14. ESI MS spectra of Co(Mabiq) piperonoyl chloride **B**, m/z = [M–Cl]$^+$.

5. Substrate Scope and Analytical Data

(E)-3-(4-methoxyphenyl)-1-phenylprop-2-en-1-one (5aa)
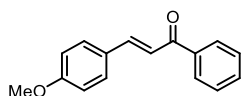
The title compound **5aa** was synthesized according to the general procedure using 4-methoxystyrene (27 µL, 0.2 mmol, 1 equiv.) and benzoyl chloride (46 µL, 0.4 mmol, 2 equiv.). The crude was purified by silica gel flash column chromatography (hexanes: ethyl acetate = 10:1) to afford **5aa** as a yellow solid (33 mg, 68%). 1H NMR (400 MHz, CDCl$_3$) δ 8.02 (d, *J* = 6.9 Hz, 2H), 7.79 (d, *J* = 15.6 Hz, 1H), 7.59 (dd, *J* = 16.2, 8.0 Hz, 3H), 7.50 (t, *J* = 7.4 Hz, 2H), 7.42 (d, *J* = 15.7 Hz, 1H), 6.94 (d, *J* = 8.7 Hz, 2H), 3.86 (s, 3H). ^{13}C NMR (101 MHz, CDCl$_3$) δ 190.6, 161.7, 144.7, 138.5, 132.5, 130.2, 128.5, 128.4, 127.6, 119.7, 114.4, 55.4. GCMS (*m/z*): calc. 238.09, found 238.2.

(E)-3-(4-ethoxyphenyl)-1-phenylprop-2-en-1-one (5ba)
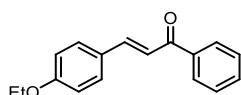
The title compound **5ba** was synthesized according to the general procedure using 4-ethoxystyrene (30 µL, 0.2 mmol, 1 equiv.) and benzoyl chloride (46 µL, 0.4 mmol, 2 equiv.). The crude was purified by silica gel flash column chromatography (hexanes: ethyl acetate = 10:1) to afford **5ba** as a pale-yellow solid (36 mg, 72%). 1H NMR (400 MHz, CDCl$_3$) δ 8.01 (d, *J* = 7.0 Hz, 2H), 7.79 (d, *J* = 15.6 Hz, 1H), 7.58 (dd, *J* = 12.0, 8.1 Hz, 3H), 7.50 (t, *J* = 7.4 Hz, 2H), 7.42 (d, *J* = 15.6 Hz, 1H), 6.93 (d, *J* = 8.6 Hz, 2H), 4.09 (q, *J* = 7.0 Hz, 2H), 1.44 (t, *J* = 7.0 Hz, 3H). ^{13}C NMR (101 MHz, CDCl$_3$) δ 190.7, 161.2, 144.9, 138.6, 132.6, 130.4, 128.7, 128.5, 127.5, 119.7, 115.0, 63.8, 14.8. GCMS (*m/z*): calc. 252.1, found 252.2.

(E)-3-(4-methyphenyl)-1-phenylprop-2-en-1-one (5ca)
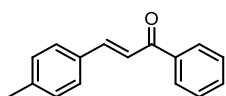
The title compound **4ca** was synthesized according to the general procedure using 4-methylstyrene (26 µL, 0.2 mmol, 1 equiv.) and benzoyl chloride (46 µL, 0.4 mmol, 2 equiv.). The crude was purified by silica gel flash column chromatography (hexanes: ethyl acetate = 10:1) to afford **5ca** as a pale-yellow solid (21 mg, 46%). ^{1}H NMR (400 MHz, CDCl$_3$) δ 8.02 (d, *J* = 6.9 Hz, 2H), 7.80 (d, *J* = 15.7 Hz, 1H), 7.62 − 7.41 (m, 6H), 7.23 (d, *J* = 7.8 Hz, 2H), 2.40 (s, 3H). ^{13}C NMR (101 MHz, CDCl$_3$) δ 190.6, 144.9, 141.1, 138.3, 132.7, 132.1, 129.7, 128.6, 128.5, 128.5, 121.1, 21.5. GCMS (*m/z*): calc. 222.1, found 222.1.

(E)-3-(4-chlorophenyl)-1-phenylprop-2-en-1-one (4da)
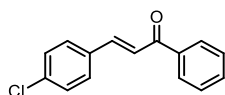
The title compound **4da** was synthesized according to the general procedure using 4-chlorostyrene (24 µL, 0.2 mmol, 1 equiv.) and benzoyl chloride (46 µL, 0.4 mmol, 2 equiv.). The crude was purified by silica gel flash column chromatography (hexanes: ethyl acetate = 10:1) to afford **4da** as a yellow solid (18 mg, 38%). ^{1}H NMR (400 MHz, CDCl$_3$) δ 8.02 (d, *J* = 7.9 Hz, 2H), 7.76 (d, *J* = 15.7 Hz, 1H), 7.64 − 7.47 (m, 6H), 7.39 (d, *J* = 8.4 Hz, 2H). ^{13}C NMR (101 MHz, CDCl$_3$) δ 190.3, 143.4, 138.1, 136.5, 133.4, 133.0, 129.7, 129.3, 128.8, 128.6, 122.5. GCMS (*m/z*): calc. 242.0, found 242.1.

(E)-3-(3-fluoro-4-methoxyphenyl)-1-phenylprop-2-en-1-one (4ea)
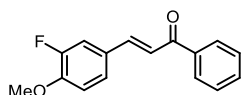
The title compound **4ea** was synthesized according to the general procedure using 3-fluoro-4metoxystyrene (27 µL, 0.2 mmol, 1 equiv.) and benzoyl chloride (46 µL, 0.4 mmol, 2 equiv.). The crude was purified by silica gel flash column chromatography (hexanes: ethyl acetate = 5:1) to afford **4ea** as a yellow oil (25 mg, 50%). ^{1}H NMR (400 MHz, CDCl$_3$) δ 8.01 (d, *J* = 6.9 Hz, 2H), 7.73 (d, *J* = 16.0 Hz, 1H), 7.59 (t, *J* = 7.3 Hz, 1H), 7.51 (t, *J* = 7.4 Hz, 2H), 7.45 − 7.33 (m, 3H), 6.98 (t, *J* = 8.5 Hz, 1H), 3.94 (s, 3H). ^{13}C NMR (101 MHz, CDCl$_3$) δ

190.3, 153.8, 151.3, 149.9, 149.8, 143.6, 143.6, 138.3, 132.9, 128.7, 128.7, 128.5, 128.3, 128.2, 126.2, 126.2, 121.0, 115.0, 114.8, 113.3, 113.3, 56.4. GCMS (*m/z*): calc. 256.1, found 256.1.

3-(4-methoxyphenyl)-1-phenylbut-2-en-1-one (4fa)
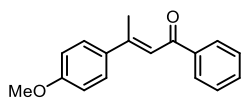
The title compound **4fa** was synthesized according to the general procedure using 1-methoxy-4-(prop-1-en-2-yl)benzene (30 mg, 0.2 mmol, 1 equiv.) and benzoyl chloride (46 μL, 0.4 mmol, 2 equiv.). The crude was purified by silica gel flash column chromatography (hexanes: ethyl acetate = 10:1) to afford **4fa** as a yellow oil (43 mg, 84%). ^{1}H NMR (400 MHz, CDCl$_3$) δ 7.99 (d, *J* = 8.2 Hz, 2H), 7.55 (t, *J* = 8.8 Hz, 3H), 7.48 (t, *J* = 5.0 Hz, 2H), 7.17 (s, 1H), 6.95 (d, *J* = 8.6 Hz, 2H), 3.85 (s, 3H), 2.61 (s, 3H). ^{13}C NMR (101 MHz, CDCl$_3$) δ 191.9, 160.7, 155.0, 139.8, 135.0, 132.5, 128.6, 128.3, 128.0, 120.5, 114.1, 55.5, 18.8. GCMS (*m/z*): calc. 252.1, found 252.1.

3-(4-fluorophenyl)-1-phenylpent-3-en-1-one (4ga)
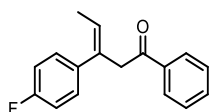
The title compound **4ga** was synthesized according to the general procedure using 1-(but-1-en-2-yl)-4-fluorobenzene (31 μL, 0.2 mmol, 1 equiv.) and benzoyl chloride (46 μL, 0.4 mmol, 2 equiv.). The crude was purified by silica gel flash column chromatography (hexanes: ethyl acetate = 5:1) to afford **4ga** as a yellow oil (27 mg, 52%). ^{1}H NMR (400 MHz, CDCl$_3$) δ 7.99 (d, *J* = 7.4 Hz, 2H), 7.58 (t, *J* = 7.4 Hz, 1H), 7.47 (t, *J* = 7.6 Hz, 2H), 7.26 – 7.20 (m, 2H), 6.95 (t, *J* = 8.6 Hz, 2H), 6.06 (q, *J* = 6.8 Hz, 1H), 4.17 (s, 2H), 1.79 (d, *J* = 6.9 Hz, 3H). ^{13}C NMR (101 MHz, CDCl$_3$) δ 197.1, 163.2, 160.7, 139.1, 139.1, 136.9, 133.3, 133.3, 128.8, 128.3, 127.7, 127.6, 127.0, 115.3, 115.1, 40.7, 14.8. GCMS (*m/z*): calc. 254.1, found 254.2.

(E)-1,3-bis(4-methoxyphenyl)prop-2-en-1-one (4ab)
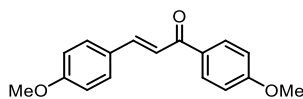
The title compound **4ab** was synthesized according to the general procedure using 4-methoxystyrene (27 μL, 0.2 mmol, 1 equiv.) and 4-methoxybenzoyl chloride (54 μL, 0.4 mmol, 2 equiv.). The crude was purified by silica gel flash column chromatography (hexanes: ethyl acetate = 10:1) to afford **4ab** as a colourless solid (38 mg, 71%). ^{1}H NMR (400 MHz, CDCl$_3$) δ 8.04 (d, *J* = 8.9 Hz, 2H), 7.78 (d, *J* = 15.6 Hz, 1H), 7.60 (d, *J* = 8.7 Hz, 2H), 7.43 (d, *J* = 15.6 Hz, 1H), 6.96 (dd, *J* = 17.6, 8.8 Hz, 4H), 3.87 (d, *J* = 13.3 Hz, 6H). ^{13}C NMR (101 MHz, CDCl$_3$) δ 188.8, 163.3, 161.5, 143.9, 132.9, 131.4, 130.7, 130.1, 127.8, 119.6, 114.4, 114.1, 113.8, 55.5, 55.4. GCMS (*m/z*): calc. 268.1, found 268.2.

(E)-1-(benzo[d][1,3]dioxol-5-yl)-3-(4-methoxyphenyl)prop-2-en-1-one (4ac)
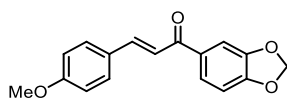
The title compound **4ac** was synthesized according to the general procedure using 4-methoxystyrene (27 μL, 0.2 mmol, 1 equiv.) and 4-piperonyol chloride (74 mg, 0.4 mmol, 2 equiv.). The crude was purified by silica gel flash column chromatography (hexanes: ethyl acetate = 5:1) to afford **4ac** as a yellow solid (42 mg, 75%). ^{1}H NMR (400 MHz, CDCl$_3$) δ 7.77 (d, *J* = 15.6 Hz, 1H), 7.68 – 7.55 (m, 3H), 7.53 (d, *J* = 1.8 Hz, 1H), 7.38 (d, *J* = 15.5 Hz, 1H), 6.91 (dd, *J* = 16.8, 8.4 Hz, 3H), 6.06 (s, 2H), 3.86 (s, 3H). ^{13}C NMR (101 MHz, CDCl$_3$) δ 188.4, 161.7, 151.6, 148.4, 144.2, 133.4, 130.3, 127.8, 124.6, 119.5, 114.5, 108.6, 108.0, 102.0, 55.5. GCMS (*m/z*): calc. 282.1, found 282.2.

(E)-1-(4-chlorophenyl)-3-(4-methoxyphenyl)prop-2-en-1-one (4ad)
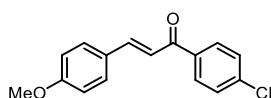
The title compound **4ad** was synthesized according to the general procedure using 4-methoxystyrene (27 μL, 0.2 mmol, 1 equiv.) and 4-chlorobenzoyl chloride (51 μL, 0.4 mmol, 2 equiv.). The crude was purified by silica gel flash column chromatography (hexanes: ethyl acetate = 10:1) to afford **4ad** as a yellow solid (28 mg, 51%). ^{1}H NMR (400 MHz, CDCl$_3$) δ 7.96 (d, *J* = 8.6 Hz, 2H), 7.79 (d, *J* = 15.6 Hz, 1H), 7.61

(d, *J* = 8.8 Hz, 2H), 7.47 (d, *J* = 8.6 Hz, 2H), 7.37 (d, *J* = 15.6 Hz, 1H), 6.94 (d, *J* = 8.8 Hz, 2H), 3.86 (s, 3H). ^{13}C NMR (101 MHz, CDCl$_3$) δ 189.4, 162.0, 145.4, 139.1, 136.9, 130.5, 130.0, 129.0, 127.6, 119.3, 114.6, 55.6. GCMS (*m/z*): calc. 272.1, found 272.1.

(E)-3-(4-methoxyphenyl)-1-(4-(trifluoromethyl)phenyl)prop-2-en-1-one (4ae)
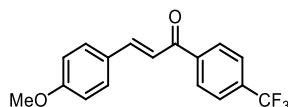
The title compound **4ae** was synthesized according to the general procedure using 4-methoxystyrene (27 μL, 0.2 mmol, 1 equiv.) and 4-trifloromethylbenzoyl chloride (59 μL, 0.4 mmol, 2 equiv.). The crude was purified by silica gel flash column chromatography (hexanes: ethyl acetate = 10:1) to afford **4ae** as a yellow solid (28 mg, 45%). ^{1}H NMR (400 MHz, CDCl$_3$) δ 8.09 (d, *J* = 8.0 Hz, 2H), 7.92 − 7.70 (m, 3H), 7.62 (d, *J* = 8.8 Hz, 2H), 7.37 (d, *J* = 15.6 Hz, 1H), 6.95 (d, *J* = 8.8 Hz, 2H), 3.87 (s, 3H). ^{13}C NMR (101 MHz, CDCl$_3$) δ 189.8, 162.2, 146.2, 141.5, 130.6, 128.8, 127.4, 125.8, 125.7, 119.4, 114.7, 55.6. GCMS (*m/z*): calc. 306.1, found 306.1.

3-(4-methoxyphenyl)-1-phenylhex-3-en-1-one (4la)
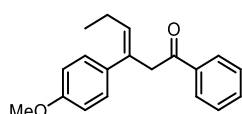
The title compound **4ia** was synthesized according to the general procedure using 1-(1-cyclopropylvinyl)-4-methoxybenzene (26 μL, 0.2 mmol, 1 equiv.) and benzoyl chloride (46 μL, 0.4 mmol, 2 equiv.). The crude was purified by silica gel flash column chromatography (hexanes: ethyl acetate = 10:1) to afford **4ia** as a pale-yellow oil (15 mg, 27%). ^{1}H NMR (400 MHz, CDCl$_3$) δ 7.91 (d, *J* = 6.9 Hz, 2H), 7.41 (t, *J* = 7.6 Hz, 2H), 7.11 (d, *J* = 8.6 Hz, 2H), 6.84 (d, *J* = 8.6 Hz, 2H), 5.56 (t, *J* = 7.3 Hz, 1H), 3.97 (s, 2H), 3.79 (s, 3H), 2.03 (p, *J* = 7.3 Hz, 2H), 0.93 (t, *J* = 7.5 Hz, 3H). ^{13}C NMR (101 MHz, CDCl$_3$) δ 198.4, 162.4, 158.4, 134.5, 133.9, 132.9, 130.6, 129.5, 128.9, 128.5, 128.4, 113.5, 55.2, 48.9, 22.6, 14.4. GCMS (*m/z*): calc. 280.1, found 280.2.

6. NMR Data

^{1}H NMR spectrum of 4aa
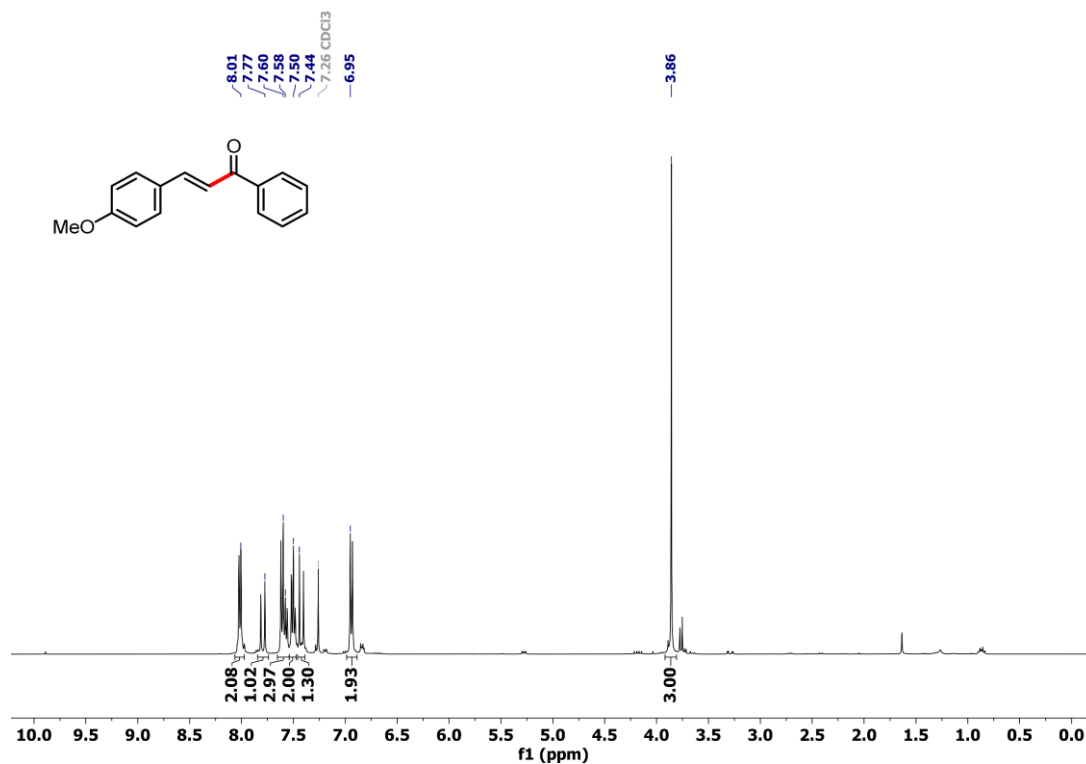
^{13}C NMR spectrum of 4aa
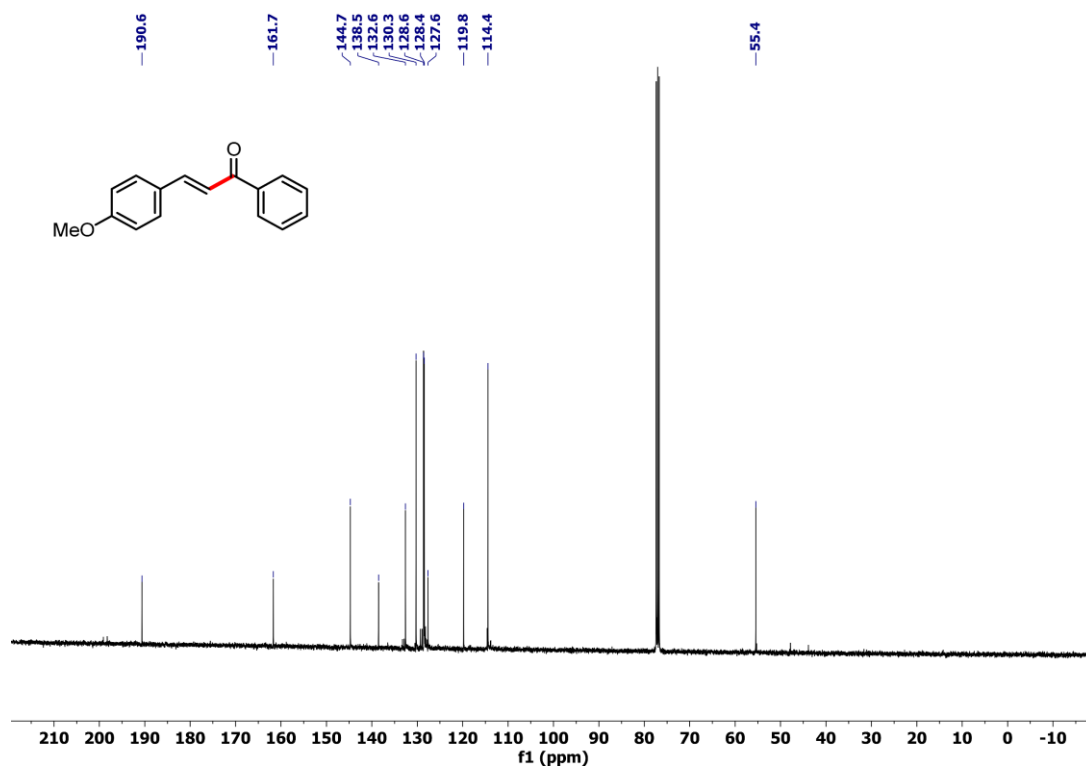
^{1}H NMR spectrum of 4ba
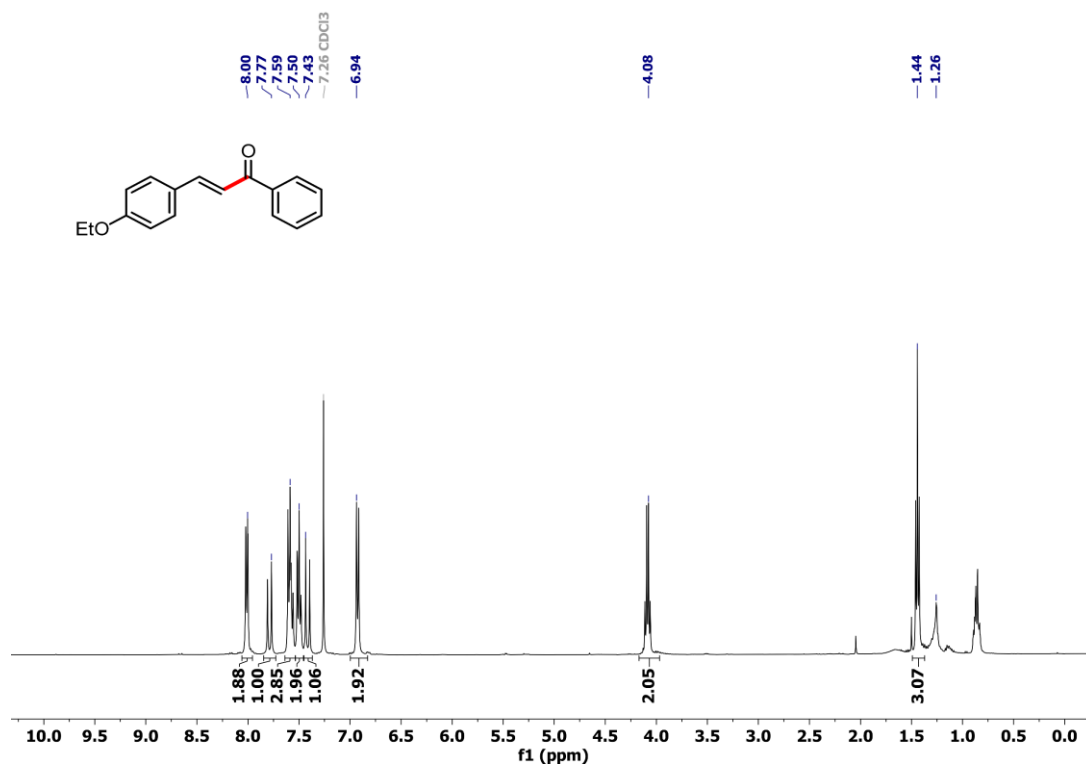
^{13}C NMR spectrum of 4ba

^{1}H NMR spectrum of 4ca

8.01
7.78
7.54
7.26 CDCl3
7.24
2.40

1.98
1.00
6.09
1.93
3.01

f1 (ppm)

^{13}C NMR spectrum of 4ca

190.7
145.0
141.1
138.4
132.7
132.2
129.7
128.6
128.5
128.5
121.1
21.6

f1 (ppm)
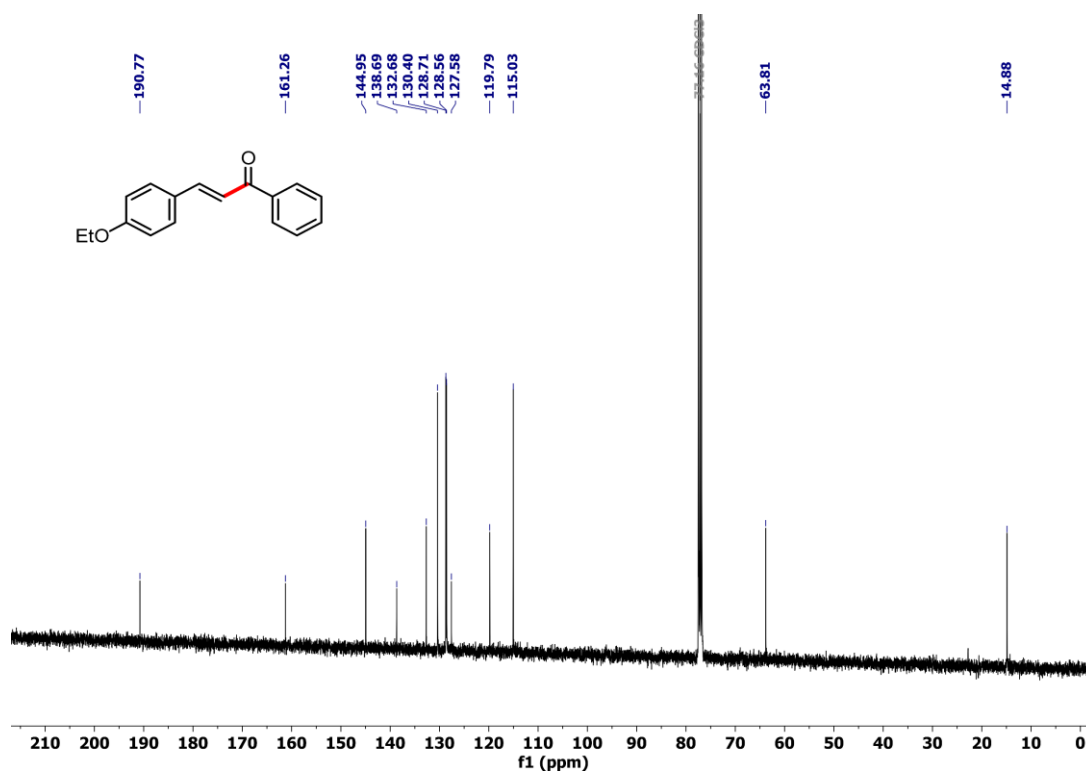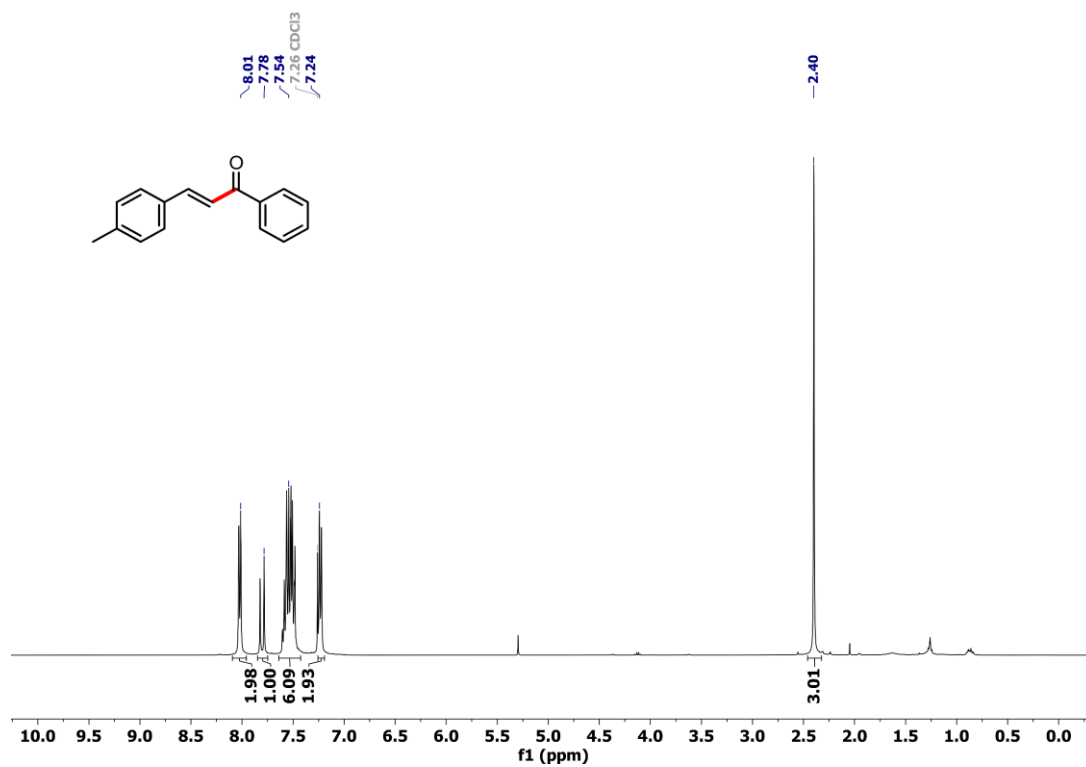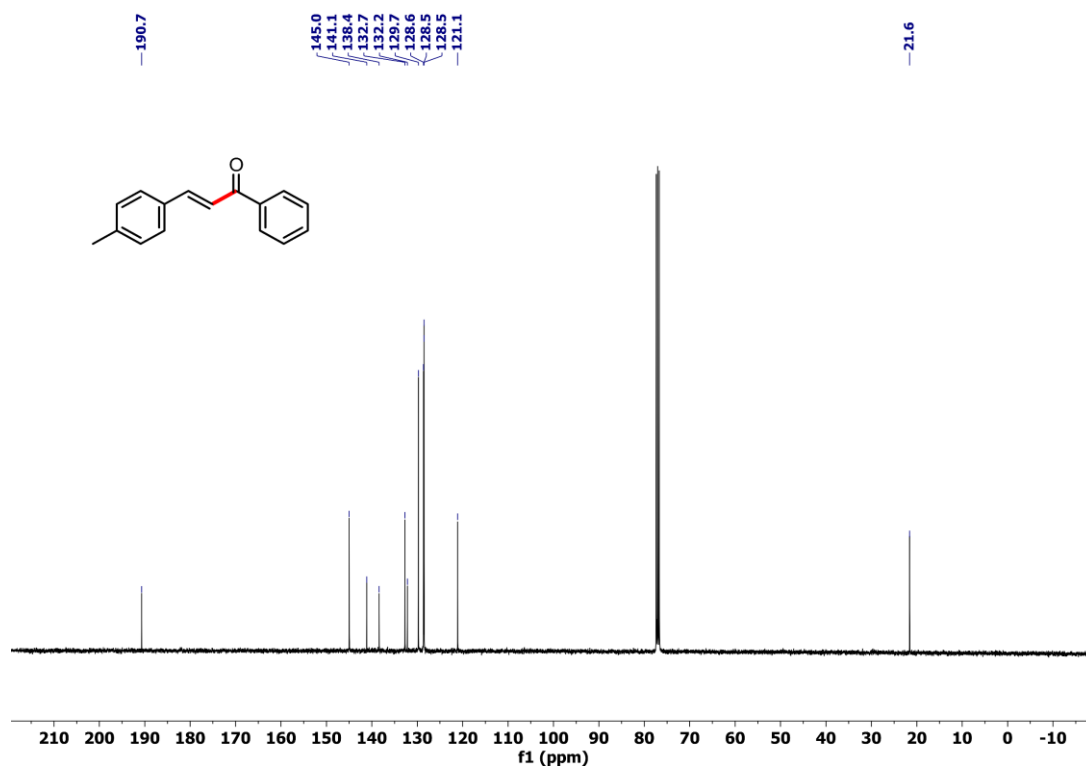
¹H NMR spectrum of 4da
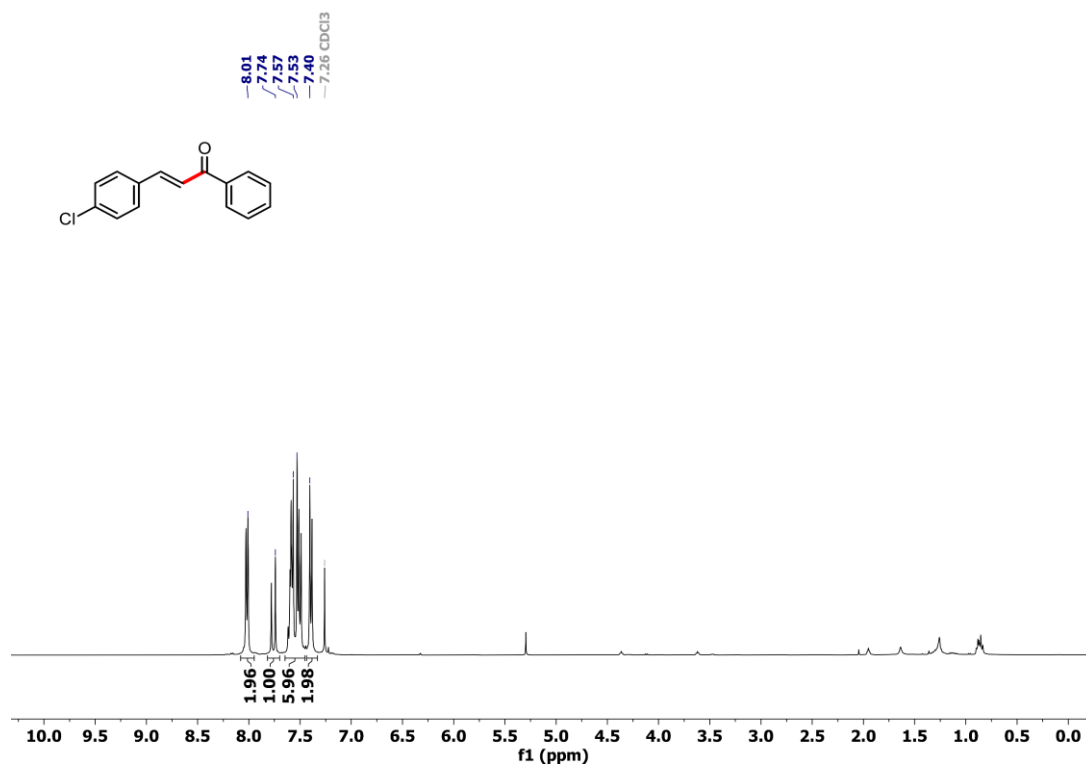
¹³C NMR spectrum of 4da
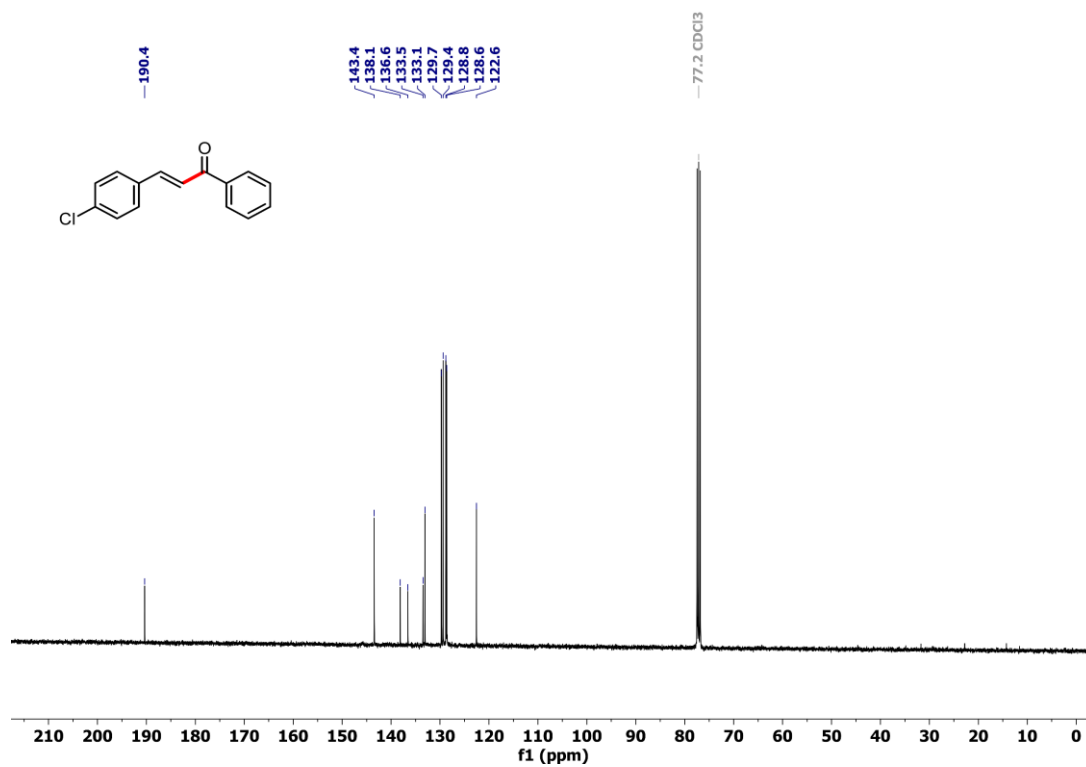
¹H NMR spectrum of 4ea
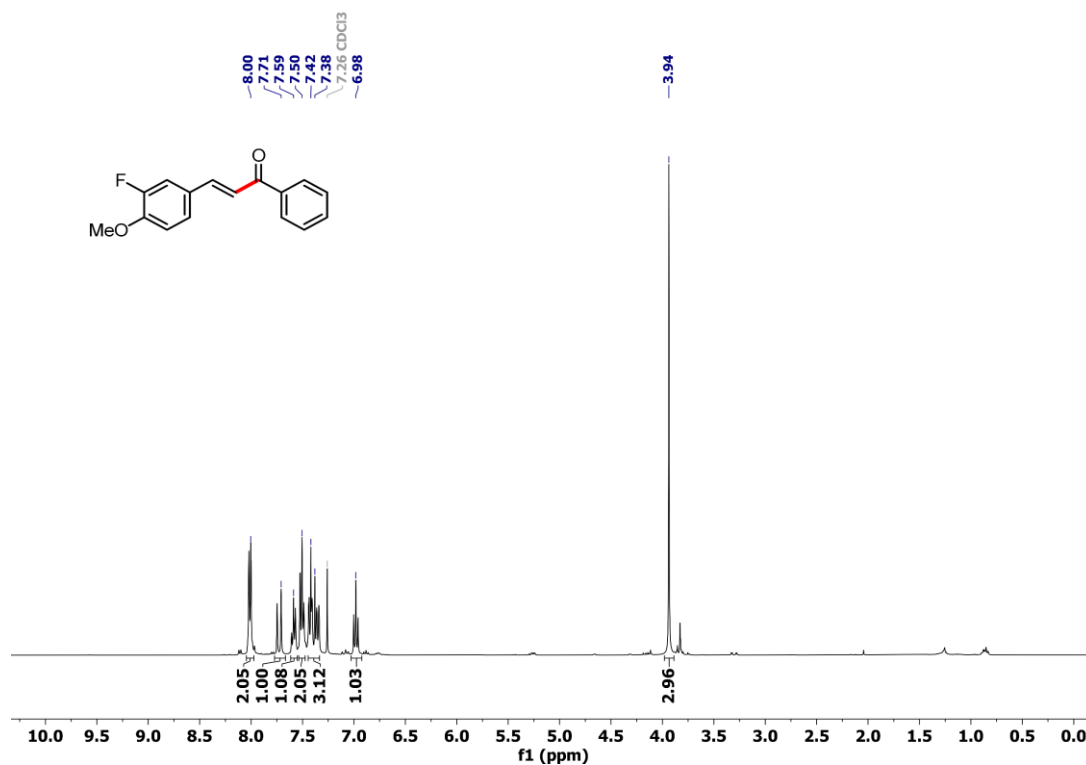
¹³C NMR spectrum of 4ea
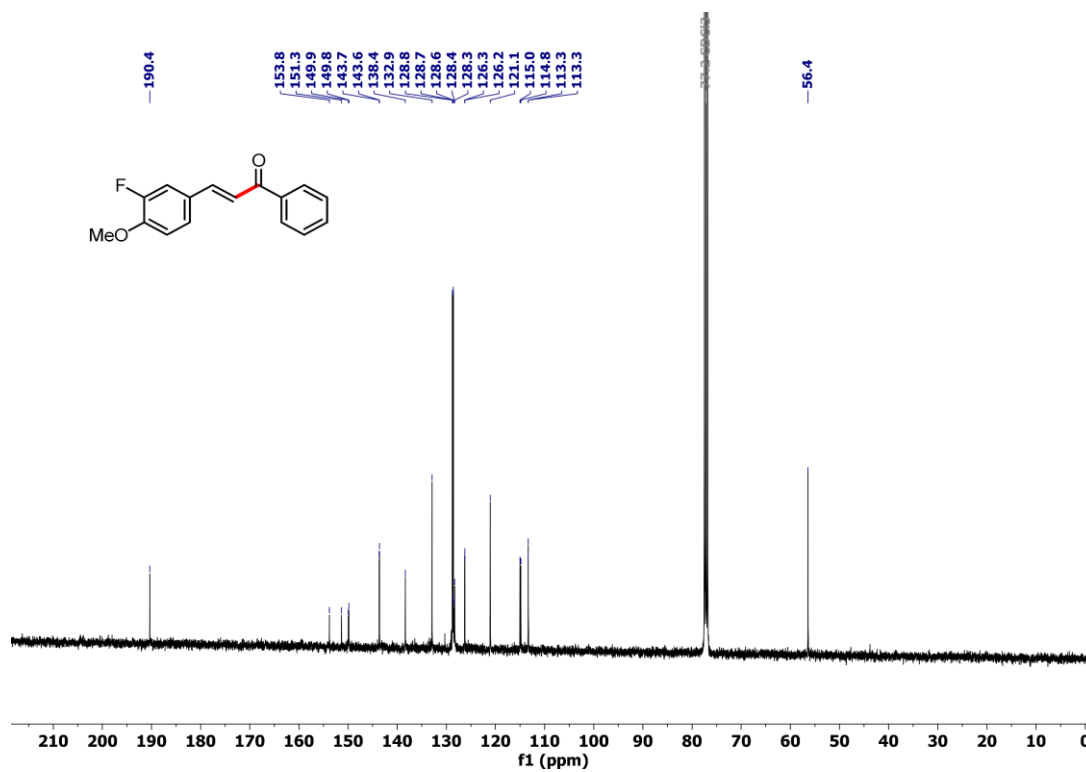
¹H NMR spectrum of 4fa
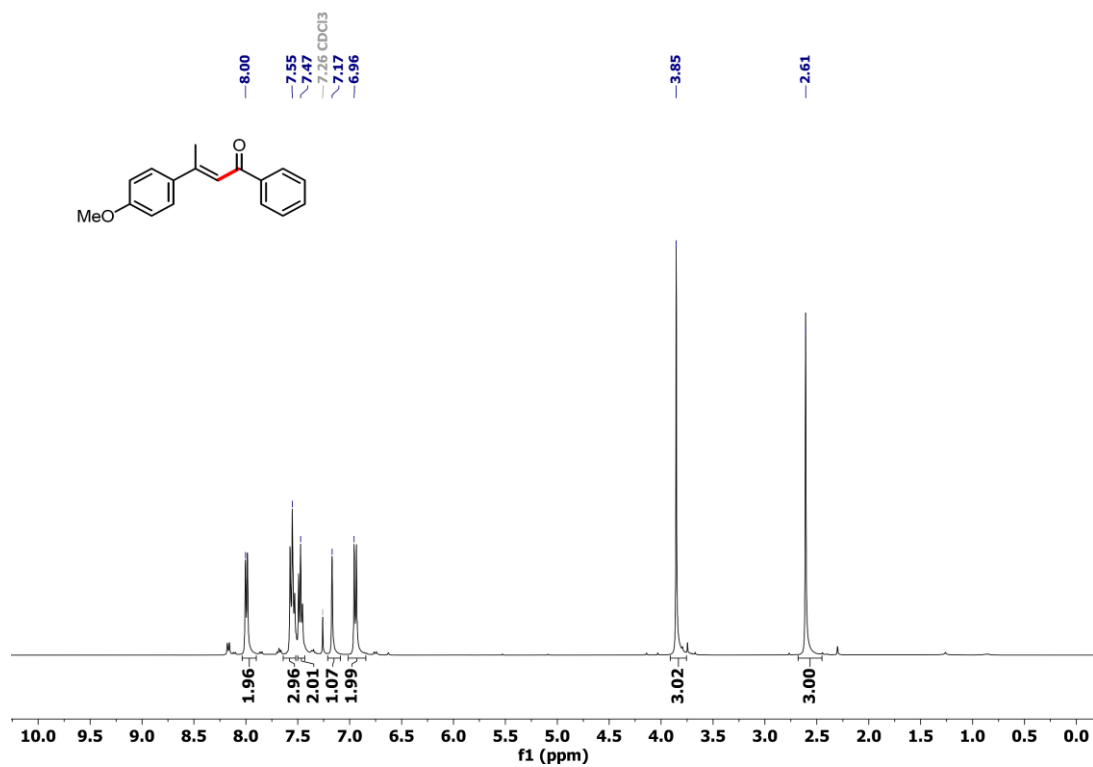
¹³C NMR spectrum of 4fa

¹H NMR spectrum of 4ga
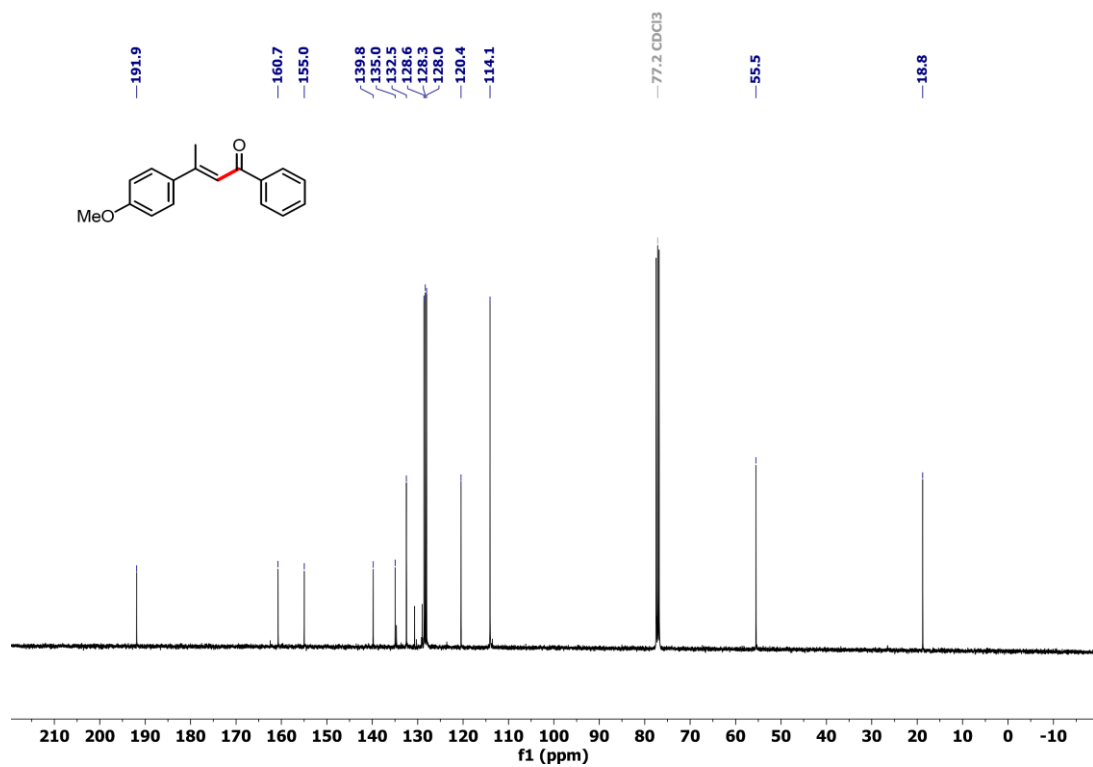
¹H NMR spectrum of 4ga

¹³C NMR spectrum of 4ga

¹H NMR spectrum of 4ab
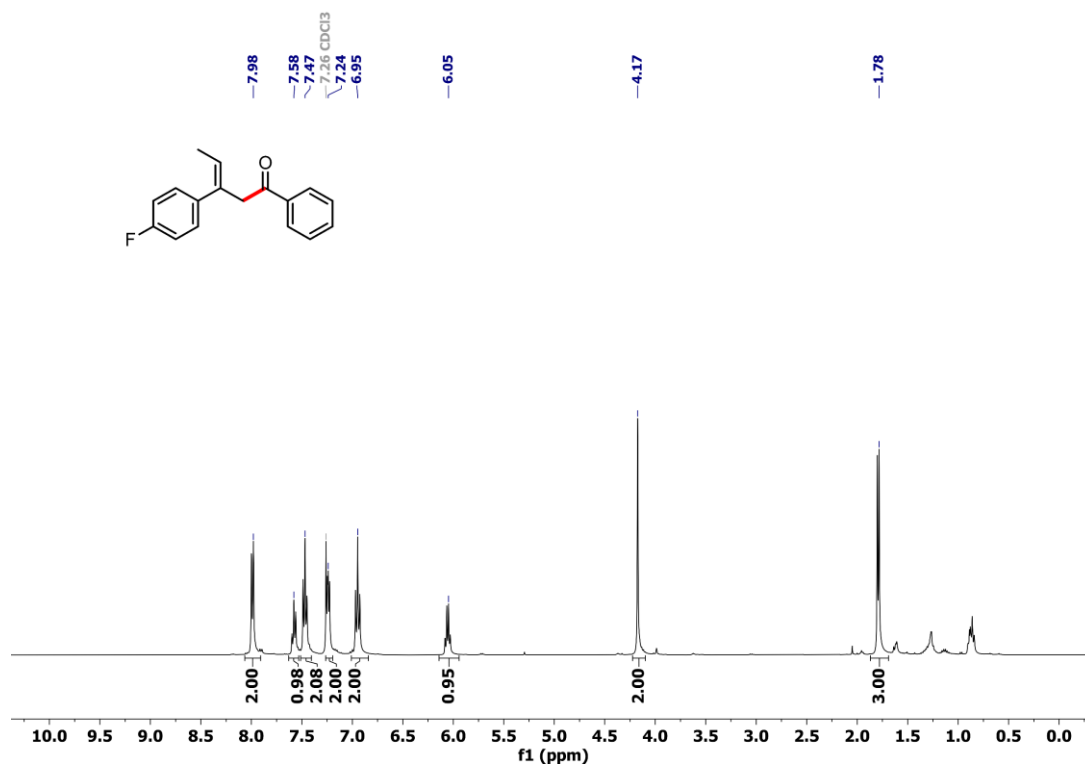
¹H NMR spectrum of 4ab
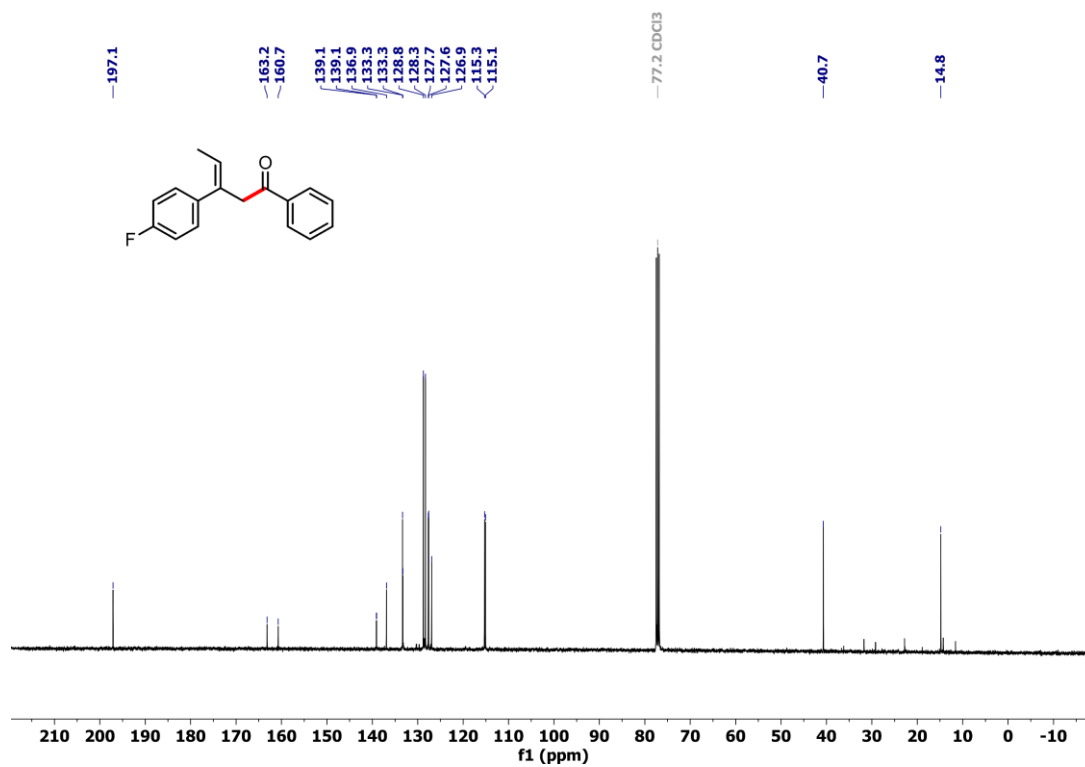
¹³C NMR spectrum of 4ab
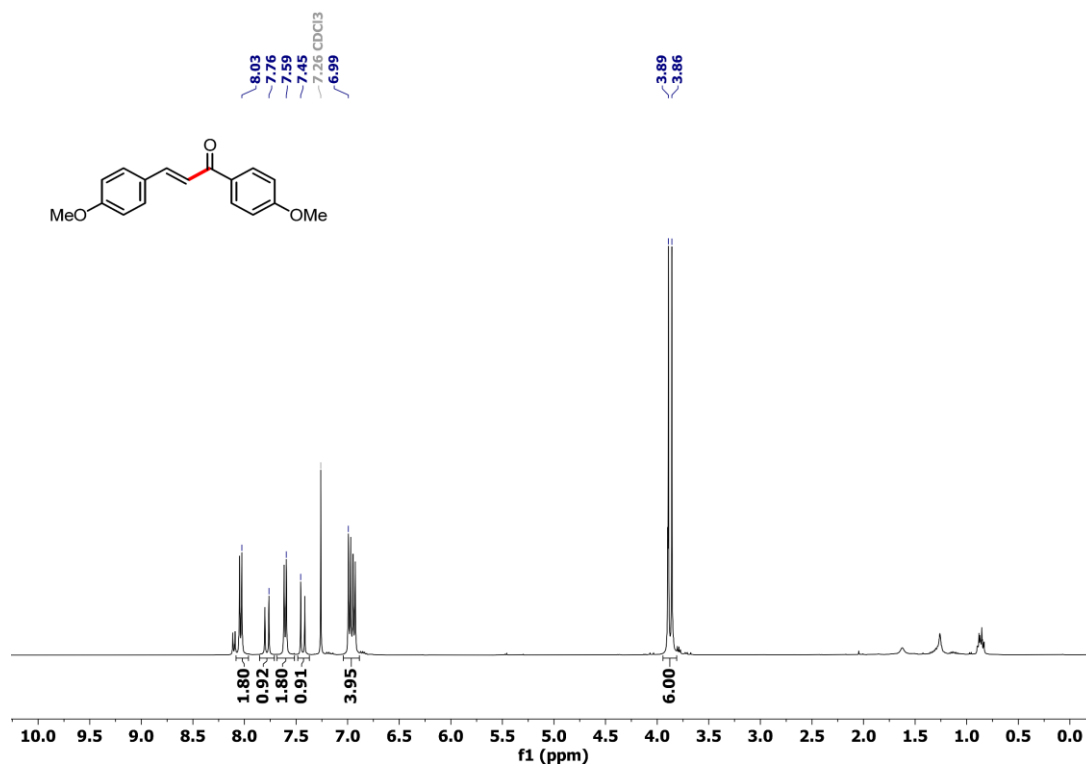
¹³C NMR spectrum of 4ab
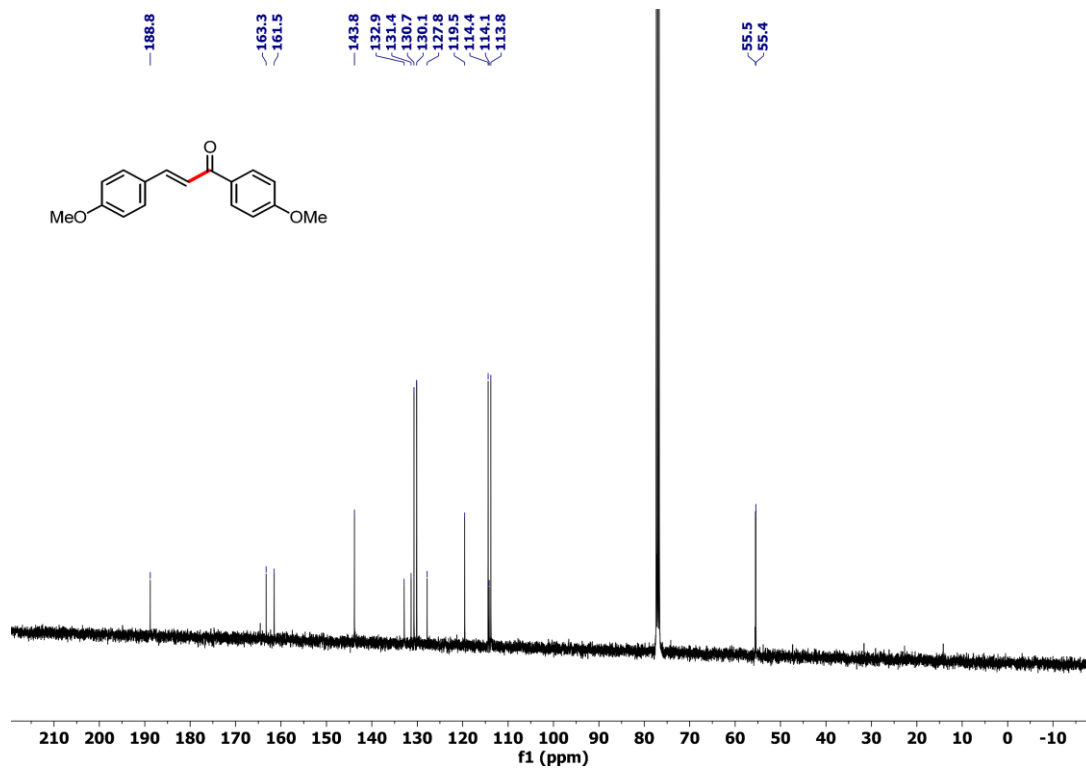
¹H NMR spectrum of 4ac
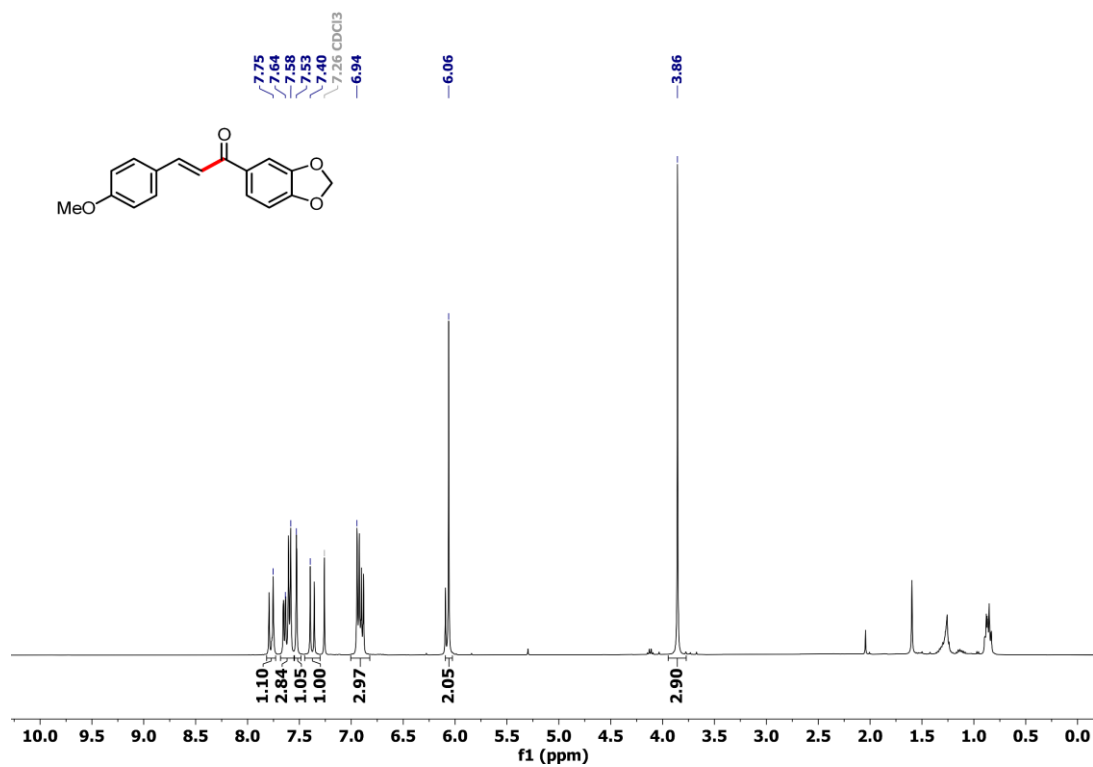
¹³C NMR spectrum of 4ac
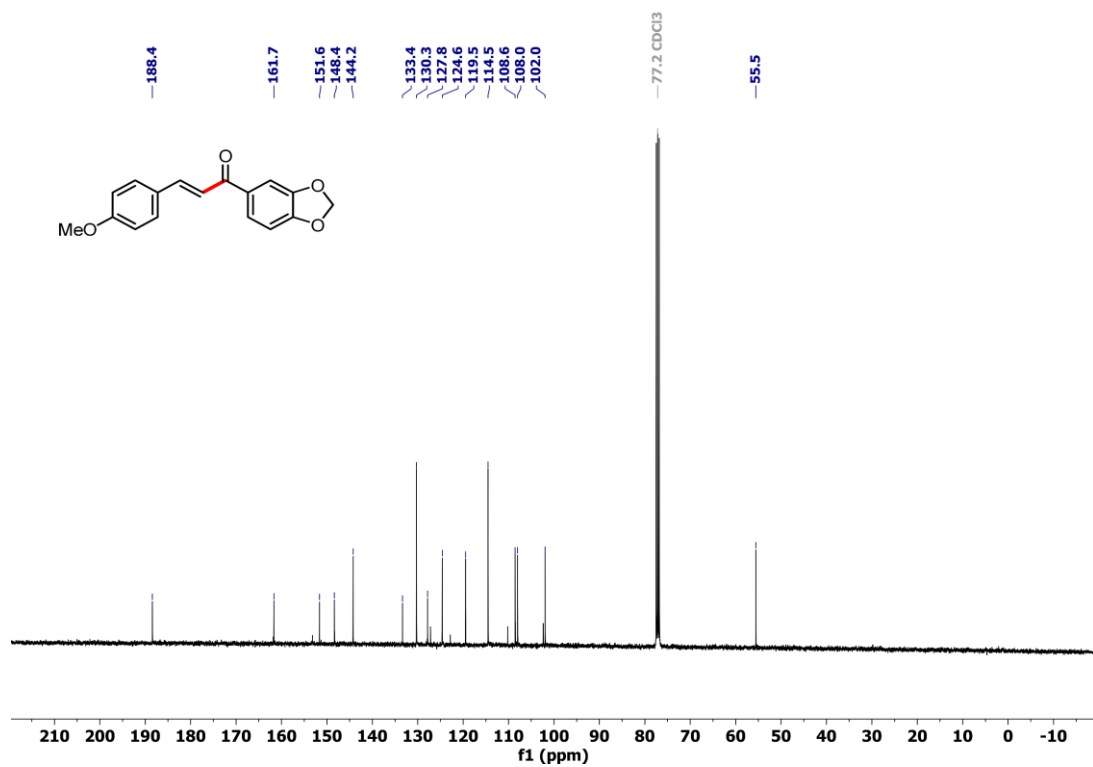
¹H NMR spectrum of 4ad
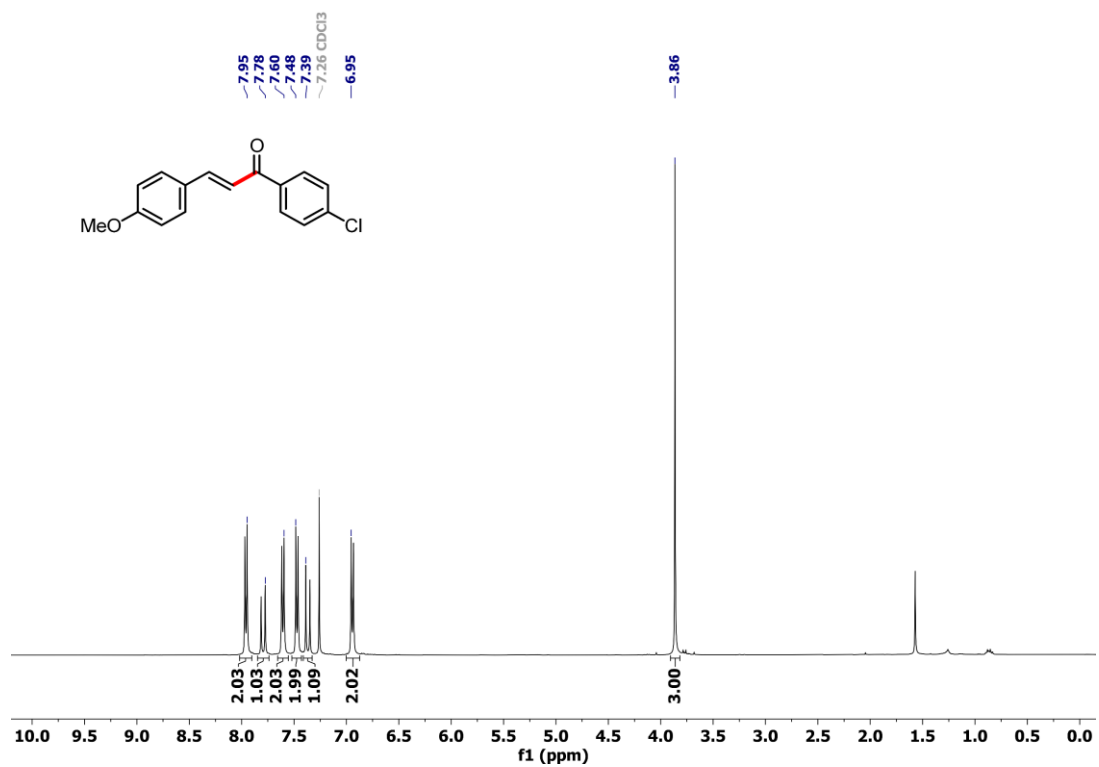
¹³C NMR spectrum of 4ad
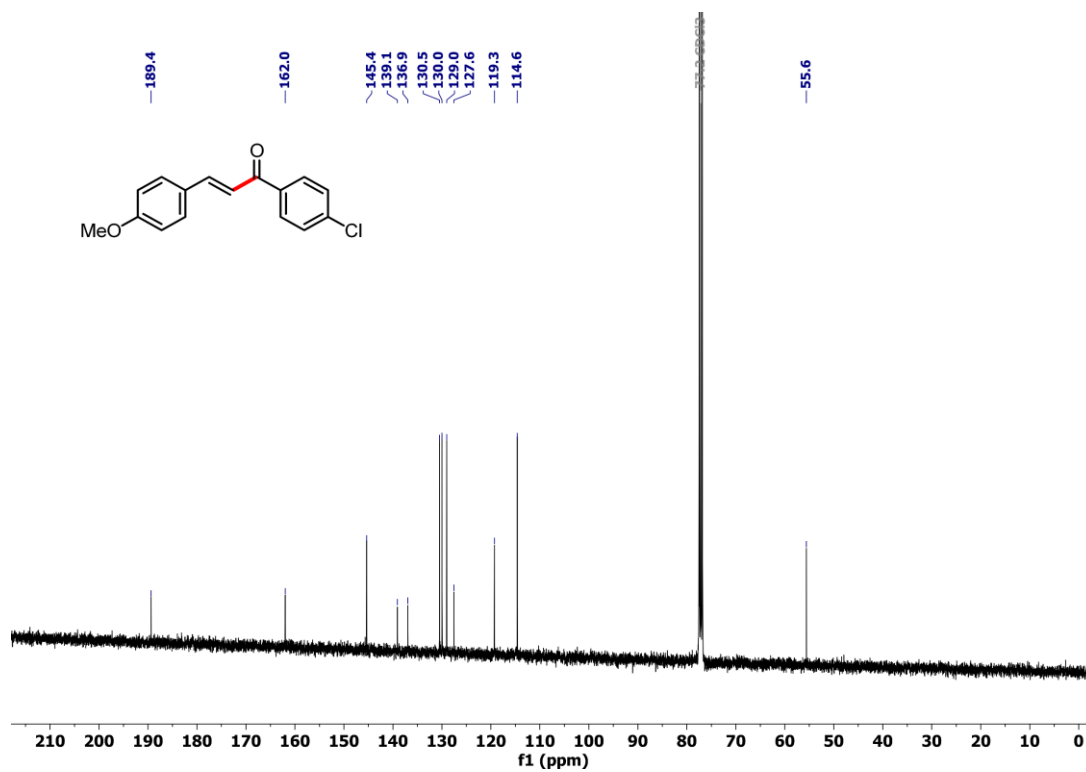
^{1}H NMR spectrum of 4ae
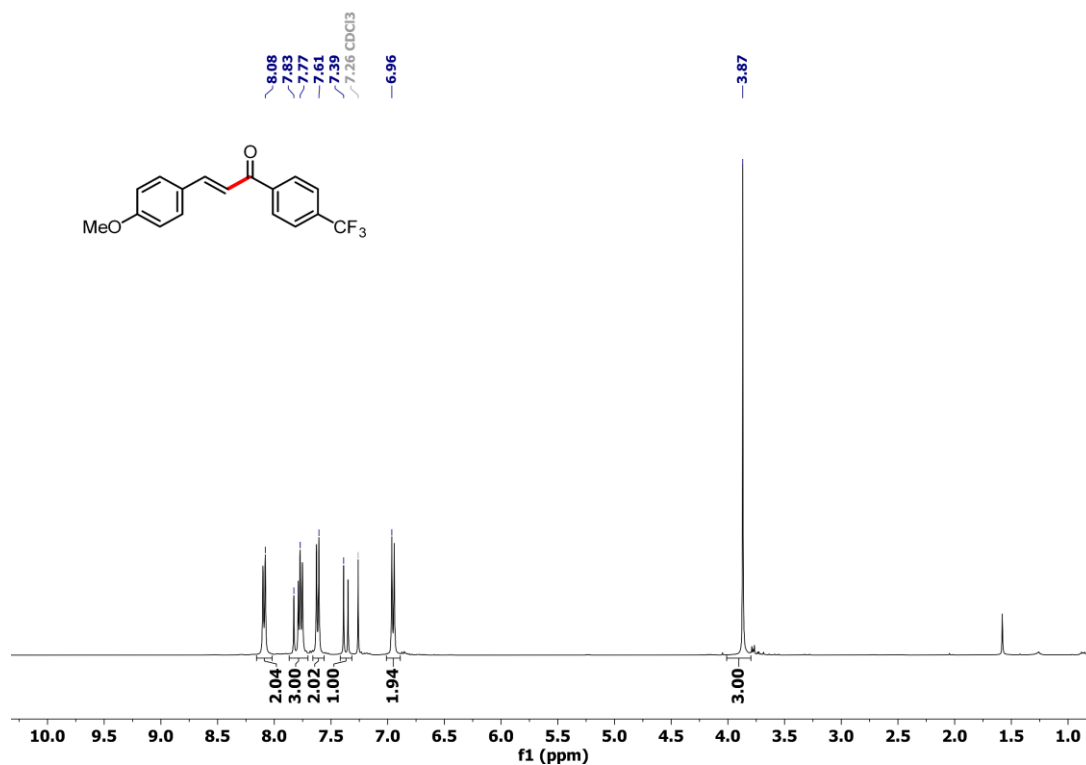
^{13}C NMR spectrum of 4ae

¹H NMR spectrum of 4ia